Skewed Highway Bridges

Final Report to

Michigan Department of Transportation

Gongkang Fu and Pang-jo Chun

Center for Advanced Bridge Engineering

Department of Civil and Environmental Engineering

Wayne State University, Detroit, Michigan 48202

August 2013

1. Report No. RC-1541	2. Government Accession No. N/A	3. MDOT Project Manager Peter Jansson
4. Title and Subtitle Skewed Highway Bridges		5. Report Date July 13, 2013
		6. Performing Organization Code N/A
7. Author(s) Gongkang Fu and Pang-jo Chun		8. Performing Org. Report No. N/A
9. Performing Organization Name and Address Center for Advanced Bridge Engineering Department of Civil and Environmental Engineering Wayne State University, Detroit, Michigan 48202		10. Work Unit No. (TRAIS) N/A
		11. Contract No. 2006-0413
		11(a). Authorization No. Z4
12. Sponsoring Agency Name and Address Michigan Department of Transportation Research Administration 8885 Ricks Rd. P.O. Box 30049 Lansing MI 48909		13. Type of Report & Period Covered Final Report 7/12/2007 – 9/30/2013
		14. Sponsoring Agency Code N/A
15. Supplementary Notes		

16. Abstract

Many highway bridges are skewed and their behavior and corresponding design analysis need to be furthered to fully accomplish design objectives. This project used physical-test and detailed finite element analysis to better understand the behavior of typical skewed highway bridges in Michigan and to thereby develop design guidelines and tools to better assist in routine design of these structures.

It is found herein that the AASHTO LRFD Bridge Design Specifications' distribution-factor analysis method is generally acceptable but overestimates the design moment for the typical Michigan skewed bridge spans analyzed herein and sometimes underestimates the design shear. Accordingly, a modification factor for possible shear underestimation based on detailed finite element analysis is recommended for routine design. Furthermore, the AASHTO specified temperature load effect is found to be relatively significant, compared with live load effect and should receive adequate attention in design. On the other hand the influence of warping and torsion effects in the analyzed typical Michigan skewed bridges is found to be small and negligible for the considered cases of span length, beam spacing, and skew angle. Based on these findings, the AASHTO distribution-factor analysis method is recommended to be used beyond the MDOT current policy of 30° skew angle limit for refined analysis, provided that the recommended modification factor C is applied and if the structure type, span length, beam spacing, and skew angle are within the ranges of the analyzed spans covered in this report.

An analytical solution for skewed thick plate modeling the concrete bridge deck is also developed in this research project, which can be furthered into an analytical solution for the bridge superstructure. When implemented in a software program, the analytical solution will serve routine design better than the distribution factor method and the finite element analysis method, without a constraint to the skew angle or a requirement for complex input such as

element type, shape, size, etc. required for finite element analysis.			
17. Key Words	**18. Distribution Statement** No restrictions. This document is available to the public through the Michigan Department of Transportation.		
19. Security Classification - report Unclassified	**20. Security Classification - page** Unclassified	**21. No. of Pages**	**22. Price** N/A

Acknowledgements

Abstract

Many highway bridges are skewed and their behavior and corresponding design analysis need to be furthered to fully accomplish design objectives. This project has used an approach of physical-test-aided and detailed finite element analysis to better understand the behavior of typical skewed highway bridges in Michigan and to thereby develop design guidelines and tools to better assist in routine design of these structures.

It has been found in this research effort that the AASHTO LRFD Bridge Design Specifications' distribution-factor analysis method is generally acceptable but overestimates the design moment for the typical Michigan skewed bridge spans analyzed herein and sometimes underestimates the design shear. Accordingly, a modification factor for possible shear underestimation based on detailed finite element analysis is recommended for routine design. Furthermore, the AASHTO specified temperature load effect is found to be relatively significant, compared with live load effect and should receive adequate attention in design. On the other hand the influence of warping and torsion effects in the analyzed typical Michigan skewed bridges is found to be small and negligible for the considered cases of span length, beam spacing, and skew angle. Based on these findings, the AASHTO distribution-factor analysis method is recommended to be used beyond the MDOT current policy of 30° skew angle limit for refined analysis, provided that the recommended modification factor C is applied and if the structure type, span length, beam spacing, and skew angle are within the ranges of the analyzed spans covered in this report.

An analytical solution for skewed thick plate modeling the concrete bridge deck is also developed in this research project, which can be furthered into an analytical solution for the

bridge superstructure. When implemented in a software program, the analytical solution will serve routine design better than the distribution factor method and the finite element analysis method, without a constraint to the skew angle or a requirement for complex input such as element type, shape, size, etc. required for finite element analysis.

Table of Contents

Chapter 1

Introduction

1.1 Background

Skewed bridges are commonly used to cross roadways, waterways, or railways that are not perpendicular to the bridge at the intersection. Skewed bridges are characterized by their skew angle, defined as the angle between a line normal to the centerline of the bridge and the centerline of the support (abutment or pier). According to the MDOT 2007 bridge inventory, about 33% of all bridges in Michigan are skewed with the angle ranging from 1º to 60º. The AASHTO Standard Specifications for Highway Bridges (2002) did not account for the effect of skew. Namely there are no calculation methods or guidelines given in the specifications to cover or estimate the effect of skew. So for decades, skewed bridges were analyzed and designed in the same way as straight ones regardless of the skew angle.

Nevertheless, research work has been published (*e.g.*, Menassa et al. 2007, Bishara et. al. 1993) indicating the mechanical behavior of skewed bridges being quite different from their straight counterparts. These efforts have shown that the AASHTO standard specifications did not adequately model and predict skewed bridge member behaviors including the midspan maximum bending moment and the obtuse corner maximum shear. Note also that these researchers have used numerical analyses such as finite element analysis (FEA).

Recently mandated AASHTO LRFD Bridge Design Specifications (2007) include provisions considering skew, but within certain ranges of the design parameters, such as the

skew angle, span length, etc. These ranges are often too narrow and thus frequently exceeded in routine design. When one of the design parameters exceeds its corresponding limit, refined analysis is required by the specifications, which mostly likely would be a numerical analysis such as FEA. Unfortunately many bridge design engineers are not familiar or adequately proficient with these analysis methods. In addition, the analysis equations in the AASHTO LRFD design specifications were developed using the regression of grillage analysis results based on a number of assumptions, which may not be realistic for some cases.

MDOT currently has a skew policy that requires spans with 30 to 45 degree skew to be designed using refined methods such as FEA methods, and those beyond 45 degrees to be approved by Bridge Design and also designed using refined methods.

This project was initiated to address these concerns by better understanding skew bridge behavior and developing design guidelines and tools to facilitate design practice in Michigan.

1.2 Research objectives

This research project had the following objectives.

1) To better understand the behavior of typical skew bridges in Michigan,

2) To accordingly develop design guidelines for bridge design engineers, and

3) To develop appropriate design tools that can help bridge design engineers in routine design for typical Michigan bridges.

1.3 Research approach

To accomplish the above objectives, the following tasks were planned carried out in this research project.

1. Literature review

This task was to understand and document state of the art and the practice on the behavior of skewed highway bridges. A literature search was performed using the Transportation Research Board's (TRB) database Transportation Research Information Services (TRIS) and its Research in Progress (RiP) component, the American Society of Civil Engineers' (ASCE) publication database, and the world wide web. The identified publications were then reviewed and the results are summarized below in Chapter 2.

2. Field testing

A full scale steel plate girder bridge S02 of 82191 was selected for physical testing under deck dead load and vehicular live load to provide measured behavior data. The bridge carries Woodruff Road over I-75 and M-85 in Monroe County, Michigan. The test was conducted in summer 2009. The field test had two main purposes. The first was to understand the strain load effect of a significantly skewed structure. The second purpose was to provide measurement data for validation and calibration of finite element modeling, so that the numerical analysis method could be reliably used to analyze and understand the behavior of typical skew bridges in Michigan.

3. Finite element analysis of Michigan typical bridge spans

Finite element models of skewed bridge spans typical in Michigan were developed using calibrated modeling based on the field measurement results from Task 2. Considering its higher cost, physical measurement can only be performed on a very limited number of structures and at a limited number of perceived critical locations, while the measured data are valuable and needed for calibrating numerical modeling. On the other hand, FEA can cost-effectively demonstrate the structure's behavior at arbitrary locations with high accuracy, if properly calibrated. This approach was taken here to analyze typical skew bridge spans with various skewed angles, beam spacings, and span lengths, to understand how these parameters affect their behavior, particularly for Michigan applications. The resulting analysis data were then used to develop guidelines for routine design practice.

4. Analytical solution method

FEA as a numerical solution method requires the end user to input information to control the analysis such as the element types and sizes, besides the general information on the structure including dimensions, material properties, etc. For routine design, this requirement can become challenging to meet when FEA is required. A possible alternative is analytical solution implemented in a computer program. The advantage of this approach is that data input for analytical solutions will be much simpler because only general information about the structure will be needed. In other words, special data such as element types, shapes, and sizes will not be needed. Namely analytical solution can be a powerful design tool for routine bridge design. This research project has also attempted this approach and the product is presented in Chapter 6.

5. Development of design guidelines

This task developed guidelines and distribution-factor modifiers for typical bridge types in Michigan, based on FEA results of selected bridge types, lengths, beam spacing, and skew angles. These products are intended for bridge design engineers to use in designing Michigan skewed highway bridges.

1.4 Report organization

This research report has seven more chapters. A literature review of state of the art and practice related to skewed bridges is presented in Chapter 2.

Chapter 3 focuses on the task of field measurement of a skewed steel bridge's behavior under loading. The information about the test bridge is provided in Section 3.1. Section 3.2 discusses the instrumentation details, and Section 3.3 presents the measurement results subjected to deck dead load and vehicular live load.

Chapter 4 presents the FEA calibration process and results using the measured response data from the physical test program presented in Chapter 3. Section 4.1 discusses the FEA models used herein. Section 4.2 presents the calibration and simulation results against the measurement data. Then, a summary is provided in Section 4.3 to conclude the chapter.

Chapter 5 focuses on the FEA for the selected typical bridge spans for Michigan. Eighteen cases of simple span highway bridges typical in Michigan were modeled using the calibrated FEA approach. They were analyzed using an FEA software program, GTSTRUDL. Section 5.1 provides the details of the analyzed typical bridge spans. The skew angle, beam spacing, and span length were chosen as the parameters of investigation for their effects on the

behavior. In addition to these parameters, the effect of the span support boundary condition is also discussed. Section 5.2 reports the analysis results, compared with the results using the AASHTO LRFD specifications provisions, and Section 5.3 extends the discussion to cover thermal load effects. A summary of the chapter is given in Section 5.4.

In Chapter 6, an analytical solution for skewed thick plates is developed. This kind of solution has not been reported in the literature. The chapter starts with an introduction of the subject in Section 6.1, also discussing the Kirchhoff theory and Reissner-Mindlin theory, which are suitable for thin plate and thick plate analysis, respectively. Next, the concept of an oblique coordinate system is introduced in Section 6.2, along with its relationship to the rectangular coordinate system and the corresponding governing differential equation of skewed thick plates based on the Reissner-Mindlin theory. Its solution is provided in Section 6.3 using a sum of polynomial and trigonometric functions. Section 6.4 discusses the technique for determining the parameters in the series solution based on boundary conditions and Section 6.5 demonstrates application example results, compared with those in the literature obtained using numerical methods. Finally, Section 6.6 summarizes this chapter.

Chapter 7 presents the recommended guidelines for bridge engineers to consider in designing skewed highway bridges in Michigan. A modification factor is included as part of the recommended guidelines to mitigate underestimation of design shear as a particular design tool.

Chapter 8 summarizes the findings and contributions of this research effort, and also gives recommendations for possible future research relevant to skewed bridges.

Chapter 2

Literature Review

This chapter presents the state of the art and practice related to skewed bridge behavior and design practice, based on a literature review conducted in the present research project. The publications reviewed below were identified using the TRB research database TRIS and its research in progress component RiP, the ASCE publication database, and the world wide web. It has been observed hereby that all research efforts identified and reviewed have employed numerical approaches assisted by limited physical testing in investigating skewed bridge behavior. Regression based on the data produced using the numerical and experimental approaches was also common to identify the trend of skew effect as a function of design parameters such as skew angle, beam spacing, span length, etc.

Menassa *et al.* (2007) presented the effect of skew angle, span length, and number of lanes on simple-span reinforced concrete slab bridges using FEA. Figure 2.1 shows a representative finite element model used in this research effort. The result was compared with relevant provisions in the AASHTO standard specifications (2002) and the AASHTO LRFD specifications (2004). Ninety six different cases were analyzed subjected to the AASHTO HS20 truck. It was found that the AASHTO standard specifications (2002) overestimated the maximum moment for beam design by 20%, 50%, and 100% for 30, 40, and 50 degrees of skew, respectively. Similar results of over-estimation were also observed for the LRFD specifications (2004) - up to 40% for less than 30 degree and 50% for 50 degree skew. The researchers

therefore recommended to conduct three dimensional FEA for design instead of using the AASHTO provisions for skew angles greater than 20 degrees.
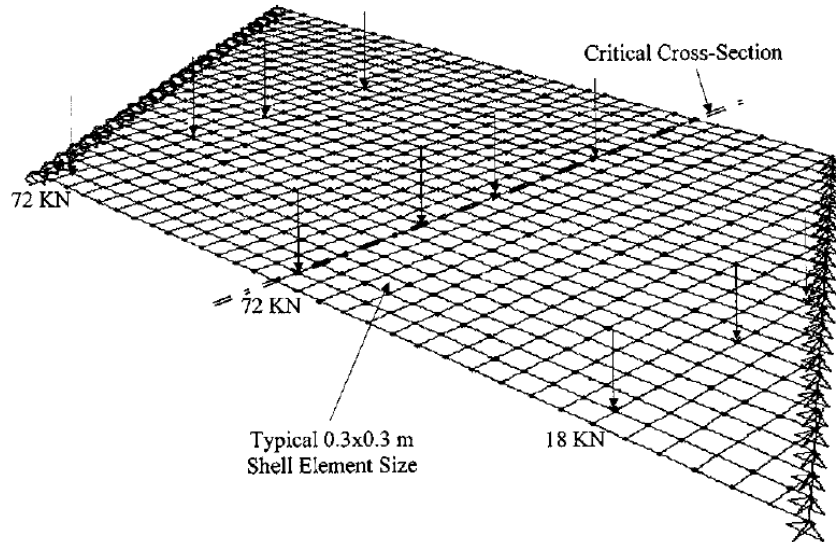

Figure 2.1 Finite element model for a 36-ft span two-lane bridge, with 30° skew

(taken from Menassa *et. al.* 2007)

Bishara *et al.* (1993) presented girder distribution factor expressions as functions of several design parameters (span length, span width, and skew angle) for wheel-loads distributed to the interior and exterior composite girders supporting a concrete deck for medium span length bridges. These expressions were determined using FEA results of 36 bridges with a 9-ft spacing of girders and different spans (75, 100, and 125 ft), widths (39, 57, and 66 ft), and skew angles (0º, 20º, 40º, and 60º). To validate this FEA model, a bridge of 137-ft length was tested in the field. From their analysis, it was concluded that a large skew angle reduces the distribution factor

for moment and the AASHTO standard specifications overestimated the maximum moment for design.

Ebeido and Kennedy (1996A, 1996B) conducted a sensitivity analysis using FEA, calibrated using physical testing of three simply supported bridge span models in the laboratory, one straight and the other two with a 45° skew. The bridge length was 12 to 14 ft, thickness of the deck was 2 in, width was 4 ft to 5 ft 8 in. After the FEA modeling calibration, more than 600 cases were analyzed using FEA to investigate the influence of parameters affecting the moment, shear, and reaction distribution factors. Empirical distribution factors were thereby developed and recommended. It was concluded that a large skew angle increases the distribution factor for shear at the obtuse corner and decreases the maximum bending moment. In addition, it was asserted that the more severely the bridge is skewed, the more the AASHTO standard specifications provisions overestimated the load effect of maximum design moment, shear, and reaction.

These efforts indicated that the AASHTO standard specifications failed to reliably model and predict skewed bridge member behaviors including maximum mid span moment and obtuse corner shear for design.

NCHRP Report 592 (BridgeTech 2007) was devoted to improving the AASHTO LRFD Bridge Design Specifications by providing simplified load distribution factors for the beam line analysis method. Skew effect was also covered. New distribution factor equations were produced using regression of numerical analysis results of a large number of bridge cases to cover wide ranges of the design parameters. However, the numerical models were relatively simple or simplistic to perhaps accommodate the large number of cases.

A typical such model using the grillage method used in that project is shown in Figure 2.2. Similar models were employed to analyze 1,560 bridge span cases with different skew angles, span lengths, beam spacings, number of lanes, truck locations, barriers, bridge types, intermediate diaphragms, and end diaphragms.

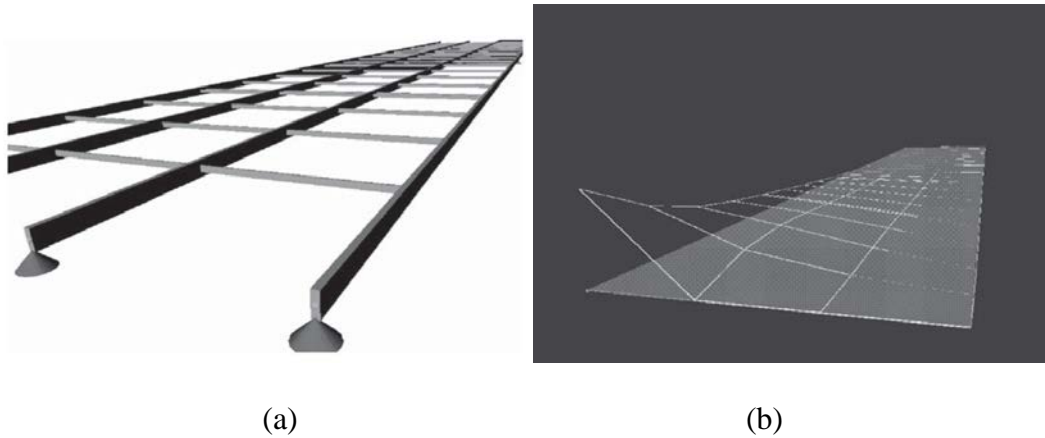(a)   (b)

Figure 2.2 A grillage bridge model taken from NCHRP Report 592

(a) non-deformed shape before truck load application

(b) deformed shape after truck load application

Nevertheless for skewed bridges, it is known that different grillage models can make the results different. For example, the two grillage models in Figure 2.3 for the same structure have been shown to produce much different results (Surana and Agrawal 1998). In Figure 2.3 (a), transverse grid lines are parallel with skew, whereas in Figure 2.3 (b) they are orthogonal to the beam lines. The model in Figure 2.3 (a) was reported to over-estimate the maximum deflection and moment, depending on the severity of skew. The model in Figure 2.3 (b) has reportedly produced more accurate results. The grillage model employed in NCHRP Report 592 as shown

in Figure 2.2 is similar to that in Figure 2.3 (a). In addition, the model is too simple to be able to cover the effect of bearings in resisting a combination of torsion, shear, moment, and axial force. Accordingly, more detailed models are recommended to be included in such refined analyses for more profound insight.
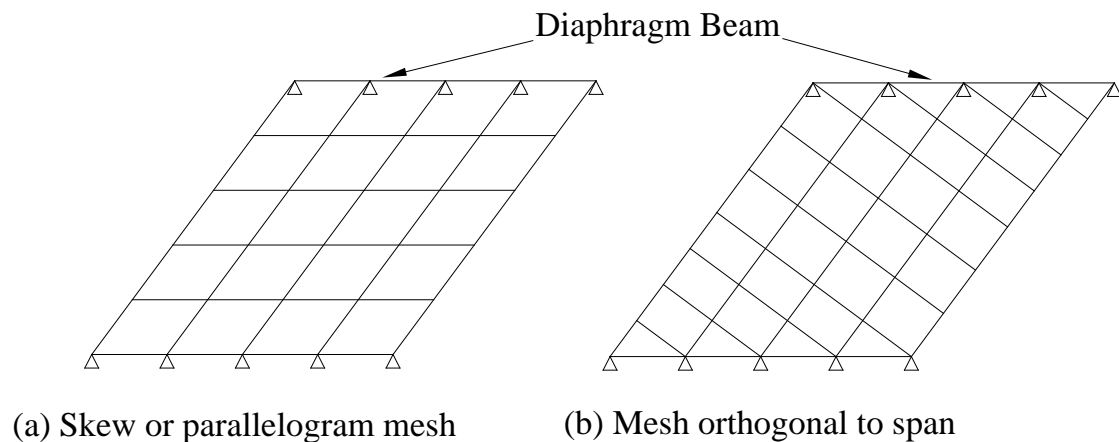

(a) Skew or parallelogram mesh   (b) Mesh orthogonal to span

Figure 2.3 Grillages for skew bridges (taken from Surana and Agrawal 1998)

(a) transverse grid lines parallel with skew

(b) transverse grid lines not parallel with skew

Helba and Kennedy (1995) conducted a parametric study of skewed bridges subject to concentric and eccentric loading using FEA. They also identified three groups of influencing parameters derived from an energy equilibrium condition: (1) the bridge geometry such as the skew angle, span length, aspect ratio, and continuity; (2) loading condition such as truck position and number of loaded lanes; and (3) the structural and material property such as those of the main girders or beams, transverse diaphragms, and the reinforced concrete deck slab and their connections.

Khaloo and Mizabozorg (2003) analyzed simply supported bridges consisting of five I-cross-section concrete girders using the commercial FEA program ANSYS. Beam elements and shell elements were used to model the girders and slab, respectively. A parametric study was conducted focusing on the following influencing factors: span length, girder spacing, and skew angle.

Huang *et al.* (2004) also developed an FEA model of a severely skewed (60°) composite bridge with steel plate girders supporting a concrete deck. The model was validated using field test. In the FEA model, the concrete slab and the longitudinal steel girders were respectively modeled using four-node shell elements and two-node beam elements with six degrees of freedom at each node, respectively.

The combination of beam and shell elements used in Khaloo and Mizabozorg (2003) and Huang *et al.* (2004) has the benefit of shorter computational time but cannot model certain details. For example, the vertical location of the diaphragms and supporting bearings cannot be included. To overcome this, in the present research project solid elements are used to model the skewed bridge spans at the expense of longer computational time.

Komatsu *et al.* (1971) attempted to analyze the behavior of skewed box girder bridges using the so called reduction method. The reduction method is a numerical analysis technique that divides the entire structure into multiple "bar elements" and then performs the required analyses. The computational cost of the reduction method can become lower than FEA methods. However, it is unable to model certain details of the structure. In Komatsu *et al.* (1971), this method was validated by testing a model skewed bridge subjected to eccentric load. The authors proposed four influencing factors to focus on in studying skew effect: the skew angle, aspect

ratio, ratio between the beams' bending stiffness and torsional stiffness, and loading condition. These factors were then investigated to understand their respective effects.

It is reasonable to conclude, based on these research efforts and results, that research on skewed bridges has overwhelmingly used numerical analysis (typically FEA) assisted by limited physical testing. On the other hand, it is also important to note that these numerical analyses have used simplified models that may miss many details that can be important in fully understanding the skew bridge behavior. Accordingly, more detailed modeling using 3D solid elements was performed in this research project to more reliably model the interested structures and their features. In addition an attempt was also made to approach to structural analysis using analytical solution in this project, to reduce the high specialty requirement for FEA, particularly for routine design.

Chapter 3

Field Test Program

As discussed in the previous chapters, there can be characteristic differences in the behavior of skewed bridges and their straight counterparts. In order to observe the behavior of skewed bridges under real truck load, field testing was conducted in this research project for physical measurement of interested responses, such as induced stresses due to accordingly changed moment and shear. The field test program had two main purposes: 1) to observe load effects of a significantly skewed bridge by measurement, and 2) to provide measurement data for the calibration of FEA modeling, so that the numerical analysis approach is reliable and its results can be used to develop design guidelines for design practice. The second purpose is more critical in the process of research reported herein, since it is to allow the numerical FEA to provide more data for the task of guideline development. Field instrumentation and testing of many bridges can be prohibitively expensive, and calibrated numerical modeling and analysis using FEA is the viable approach to understanding the behaviors of typical Michigan skewed bridges with different skew angles, span lengths, beam spacings, etc.

3.1 Test bridge

The test bridge S02 of 82191 in Monroe County, Michigan, carries Woodruff Road over I-75 and M-85, and it is hereafter referred to as the Woodruff Bridge in this report. Its superstructure includes a 9 in thick reinforced concrete deck and 6 parallel steel plate girders

spaced at 9 ft 9 in and continuous over 4 spans. The Woodruff Bridge has a skew angle of 32.5°

and it provides two lanes in each direction of east and west traffic. Figure 3.1 shows the design

drawing of the plan and elevation of the test bridge, and Figure 3.2 exhibits the instrumented and

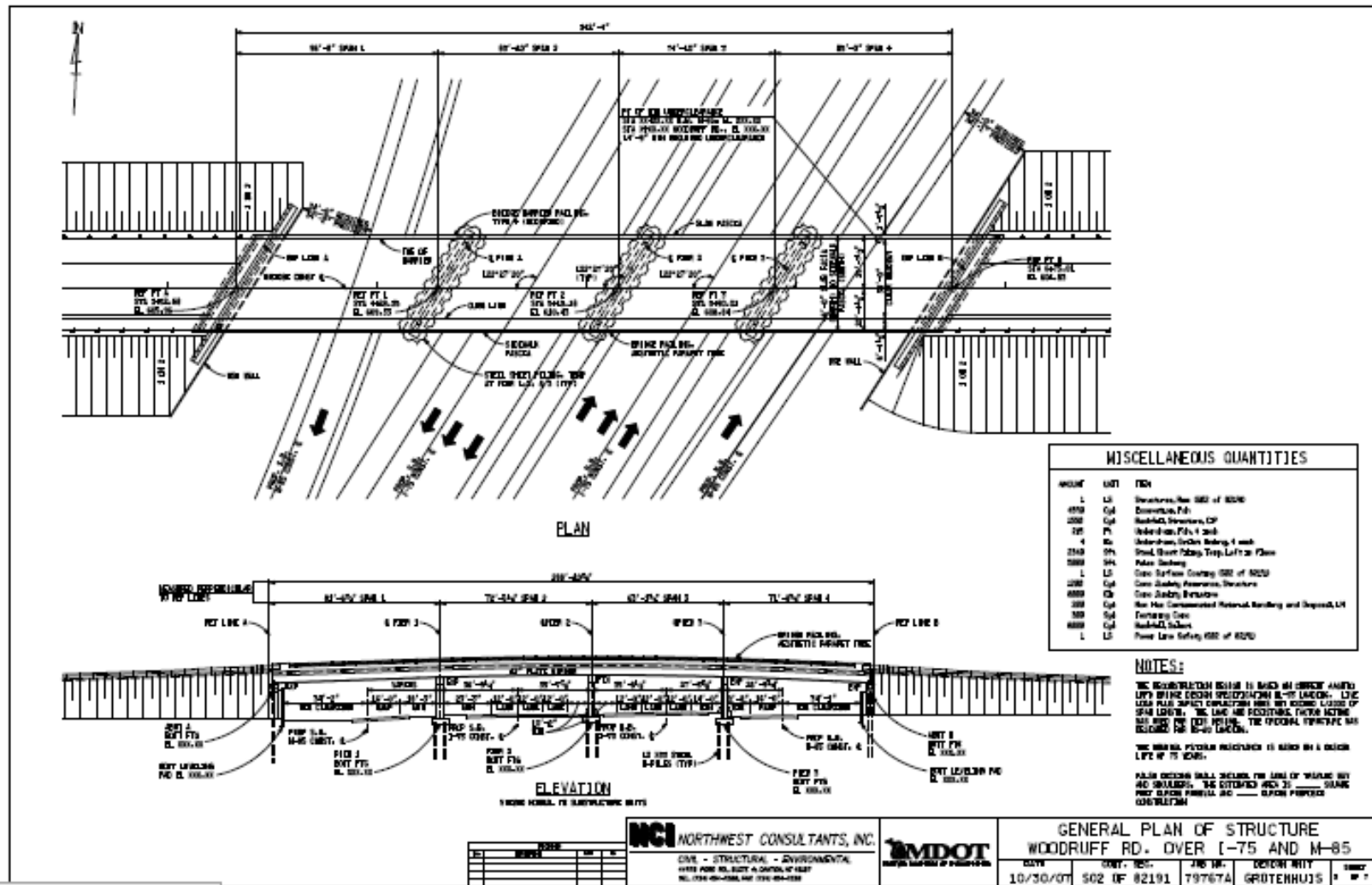tested span (Span1) on the west end before deck forming was completed during construction.

Figure 3.1   Plan and elevation of test bridge on Woodruff Road over I-75 and M-85

24

Figure 3.2 Tested span of test bridge on Woodruff Road over I-75 and M-85

Based on a preliminary FEA, an instrumentation plan was developed to use strain gages at several locations on some of the steel girders. As a result, two of the 6 girders were instrumented in one of the 4 spans (Span 1) at the west end. The tested span has a span length of 99 ft 2 in. Figure 3.3 shows the plan view of the test span along with the strain gage locations S1, S2, and S3. The six girder center lines are indicated using letters A through F. More details of instrumentation are given in the next section.
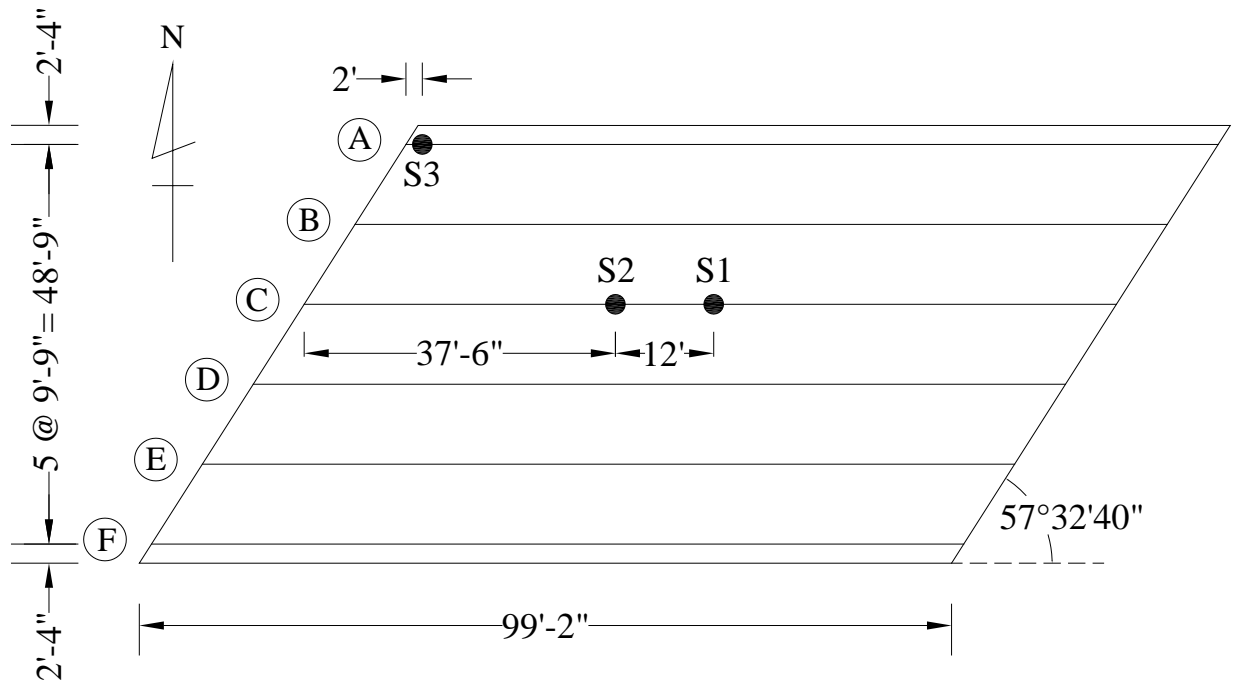
Figure 3.3 Deck and girders of the Woodruff bridge (S02 of 82191) span 1 and instrumentation

3.2 Instrumentation

Strain was measured in this bridge test program, using uni-directional strain transducers. A typical strain transducer is shown in Figure 3.4. Mounting a transducer to a structural component required surface preparation to glue two supporting stems also shown in Figure 3.4. Therefore, these strain transducers have an advantage of less field installation effort compared with foil strain gages. Load response strains were recorded using an Invocon wireless data acquisition system, as displayed in Figure 3.5. This radio wave based system offers a capability of high resolution in acquired strain data.
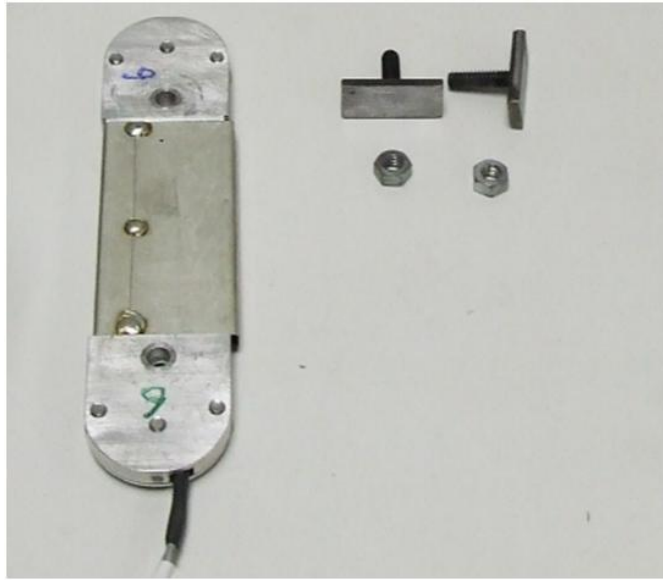
Figure 3.4 A typical strain transducer used in Woodruff Bridge test

Figure 3.5 Radio-based Invocon strain data acquisition system

The Woodruff Bridge was instrumented with 2 separate and parallel strain transducers on the bottom flange at each of the locations identified as S1 and S2 in Figure 3.3. The locations

were selected to capture maximum bending and warping strain responses based on the preliminary FEA. Figures 3.6 to 3.7 exhibit more detailed information including the locations and arrangements as well as the strain transducer identifications to be referred to later in this report when the measurement results are presented. Figure 3.8 shows a photograph of the strain transducers installed on a flange's bottom surface.
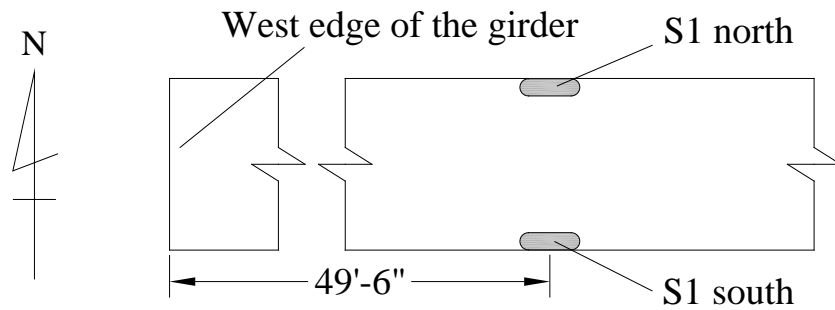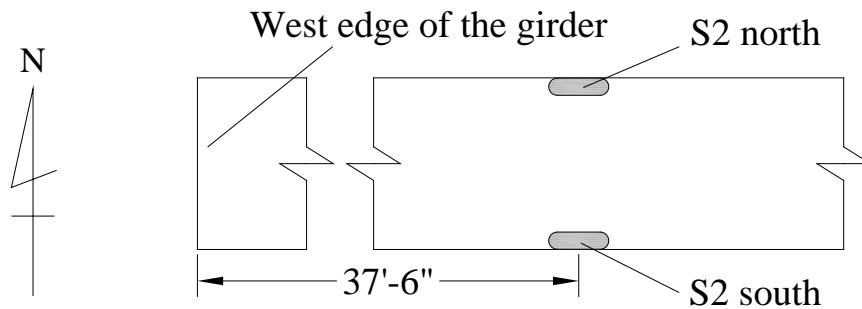

Figure 3.6 Strain transducer arrangement at location S1 on the bottom flange

Figure 3.7 Strain transducers arrangement at location S2 on the bottom flange

Figure 3.8 Strain transducer arrangement on bottom flange at Locations S1 and S2

At locations S2 and S3 indicated in Figure 3.3, shear strains were of interest. Figures 3.9 and 3.10 show the specific locations and arrangements of the strain transducers on the web of the steel beams.   At each location, three uni-directional train transducers were used to capture maximum shear responses.   Figure 3.11 exhibits the accordingly installed transducers. Along with strain measurement using these strain transducers, air temperature under the bridge was also measured. The results are to be discussed later in this report.

S2 web diagonal

S2 web vertical

S2 web transverse

CL

3'-6"

37'-6"

1'-9"
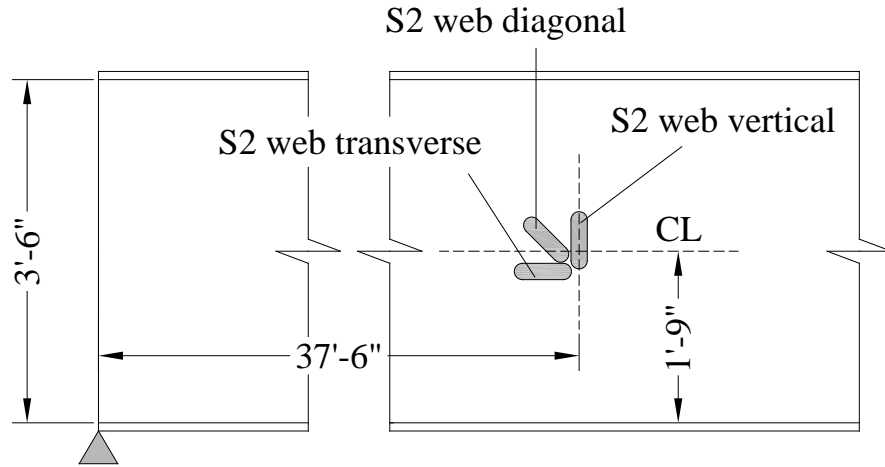
Figure 3.9 Strain transducer arrangement at location S2 on web

S3 web diagonal
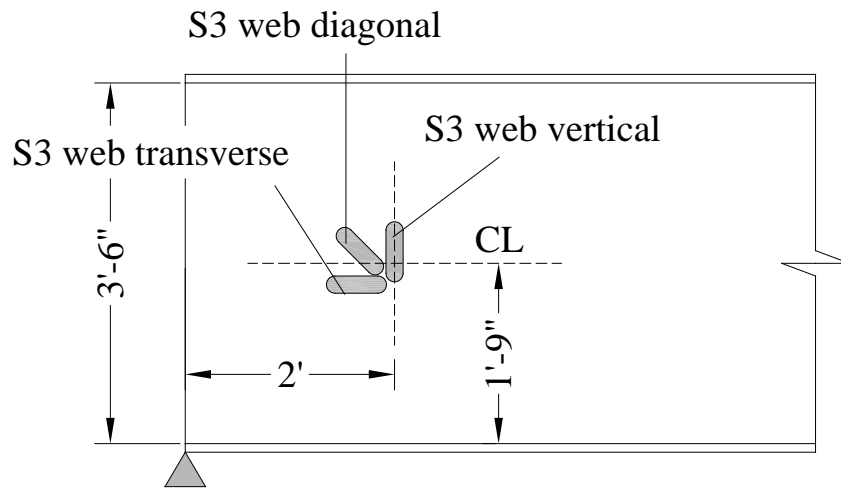
S3 web vertical

S3 web transverse

CL

3'-6"

2'

1'-9"

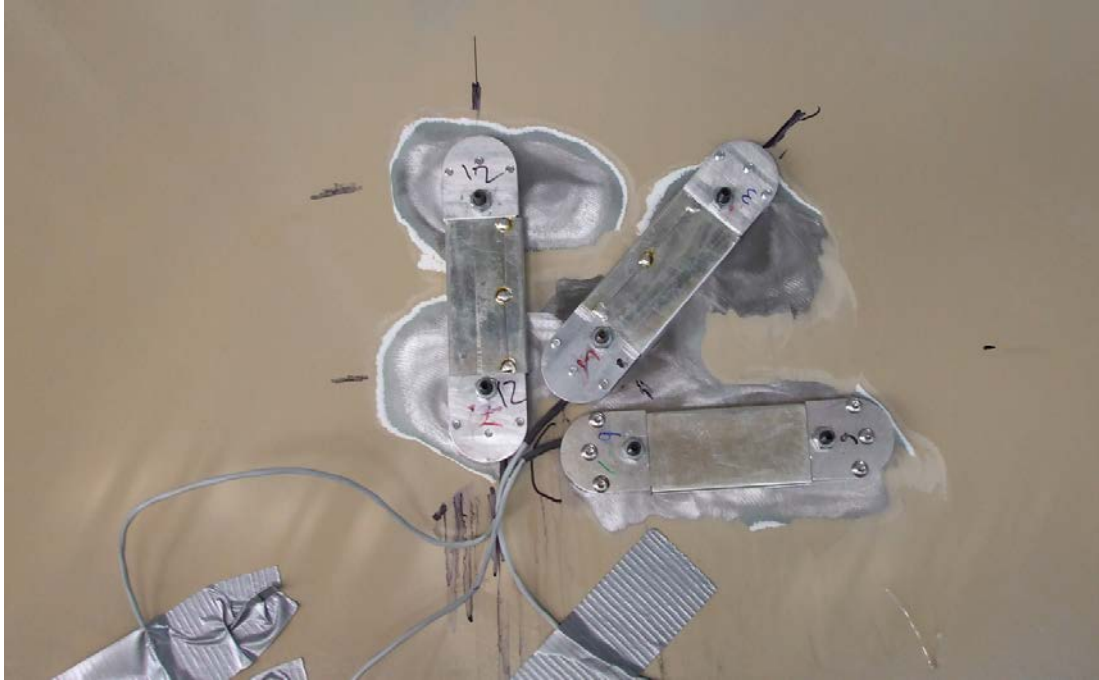Figure 3.10 Strain transducer arrangement at location S3 on web

Figure 3.11 Strain transducers arrangement on the web

3.3 Measurement results

3.3.1 Dead load effect

To understand the effect of the deck dead load, strain reading was collected during the first part of concrete placement of Span 1's deck. Figures 3.12 to 3.19 display the strain reading results for different strain transducers. Note that positive strains here are tensile strains, and negative compressive strains. Figure 3.20 shows air temperature reading results. These figures have time in minute on the horizontal axis, and microstrain (Figures 3.12 to 3.19) or temperature in degree Fahrenheit (Figure 3.20) on the vertical axis. For the time in Figures 3.12, 3.14, 3.16, and 3.18, 0 min indicates when concrete placement started, and the strain reading is accordingly

set to 0. Strain data collected before concrete placement are shown in the figures corresponding

to negative time. Note also that the strain transducer identification for each of these figures is
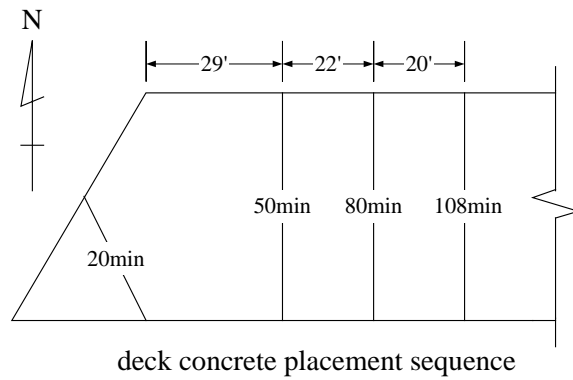
given in Figures 3.6, 3.7, 3.9, or 3.10.
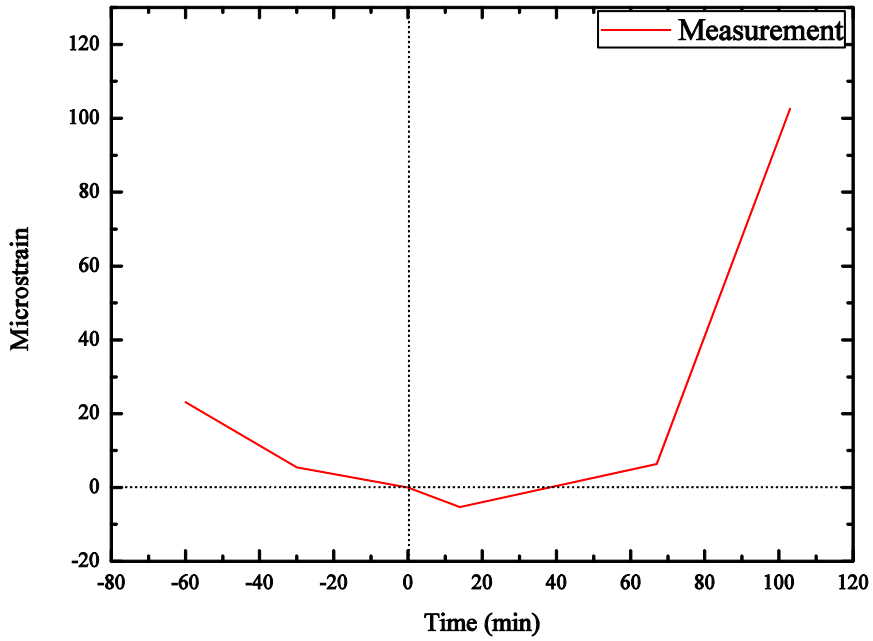

deck concrete placement sequence

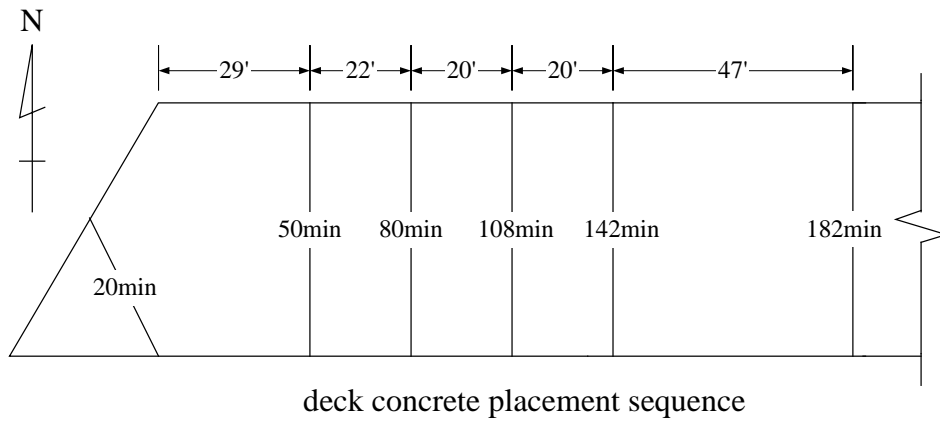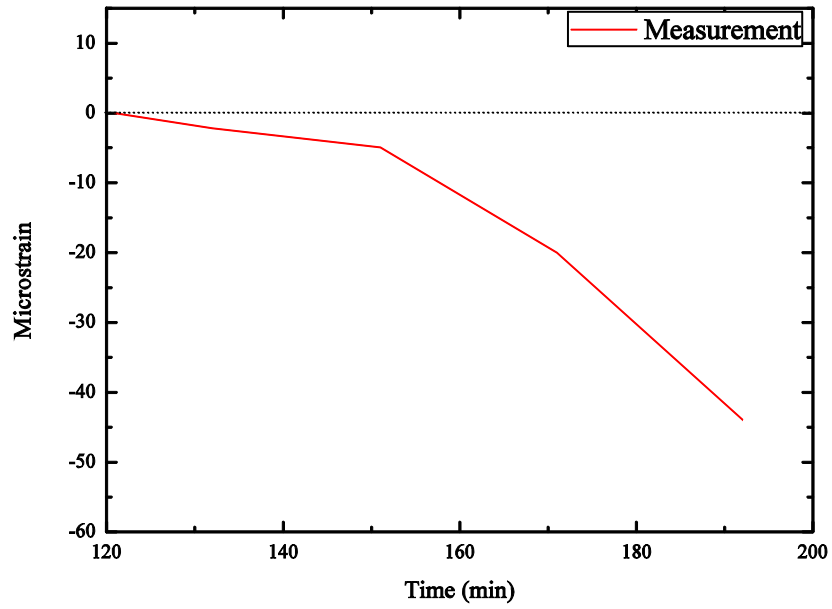Figure 3.12 Strain at "S1 south" due to concrete deck placement (up to 105 minutes)

Figure 3.13 Strain at "S1 south" due to concrete deck placement (starting from 120 minutes)
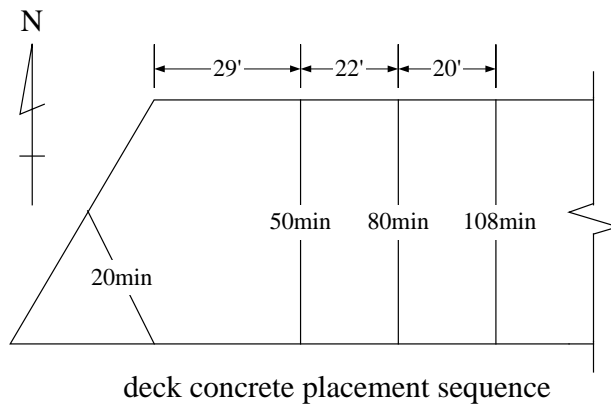
deck concrete placement sequence

Figure 3.14 Strains at "S2 south" due to concrete deck placement (up to 105 minutes)

deck concrete placement sequence

Figure 3.15 Strains at "S2 south" due to concrete deck placement (starting from 120 minutes)
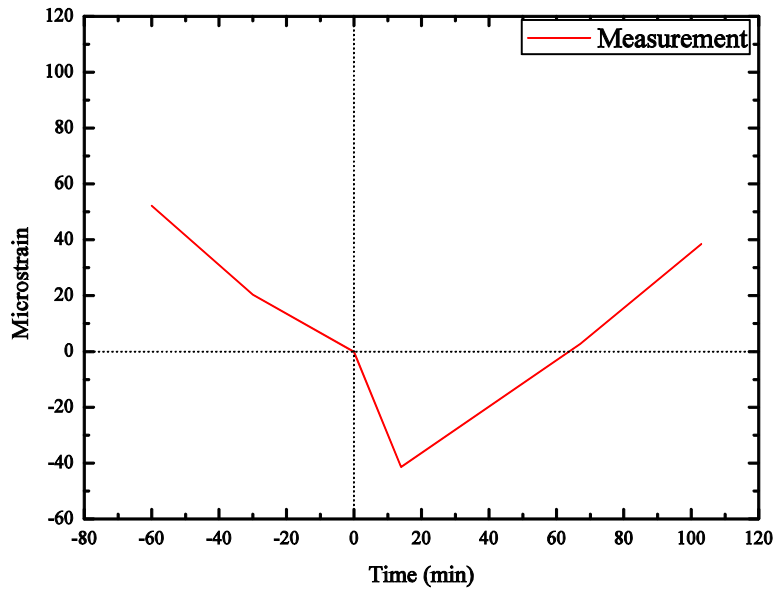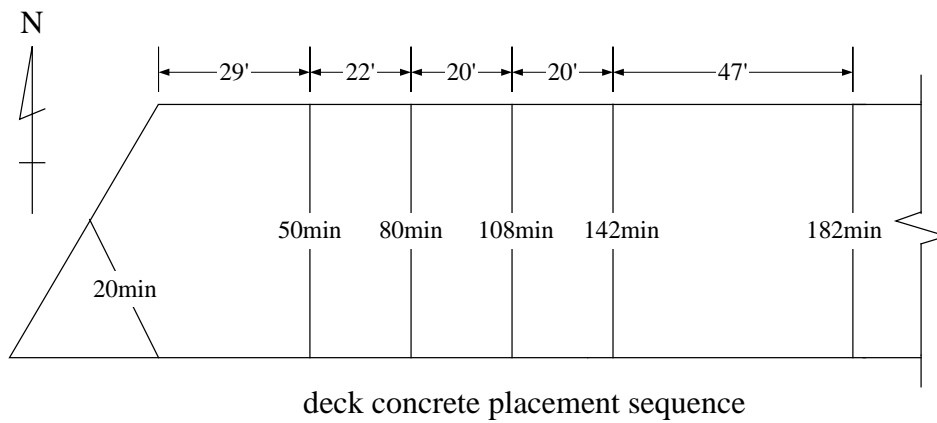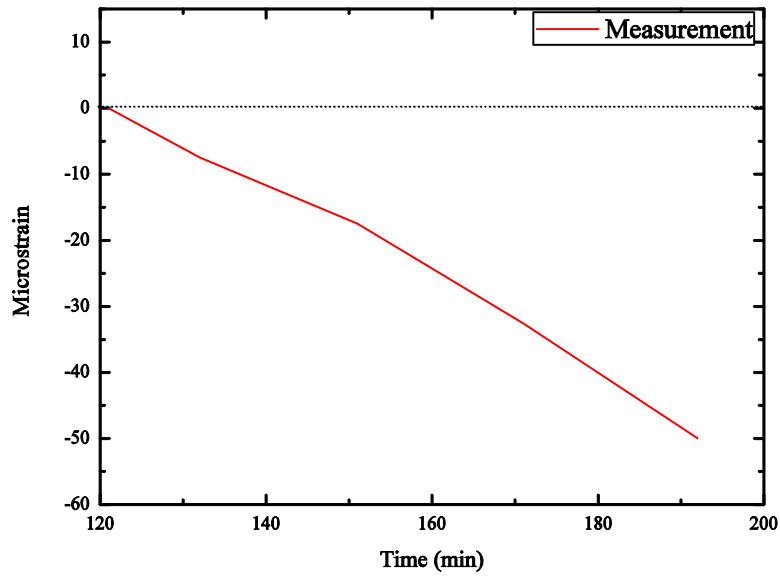
deck concrete placement sequence

Figure 3.16 Strain at "S2 web diagonal" due to concrete deck placement (up to 105 minutes)

Figure 3.17 Strain at "S2 web diagonal" due to concrete deck placement
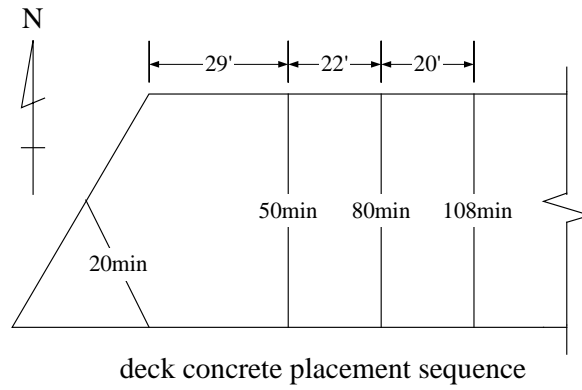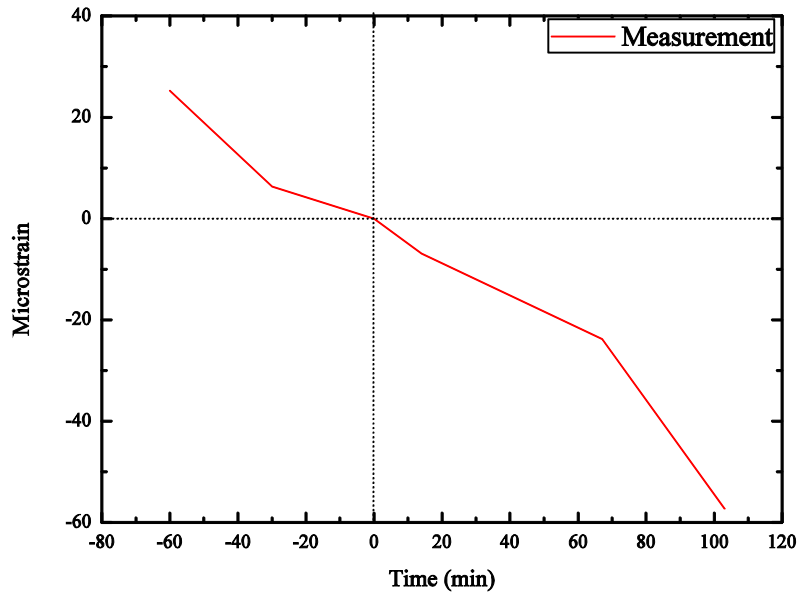
(starting from 120 minutes)

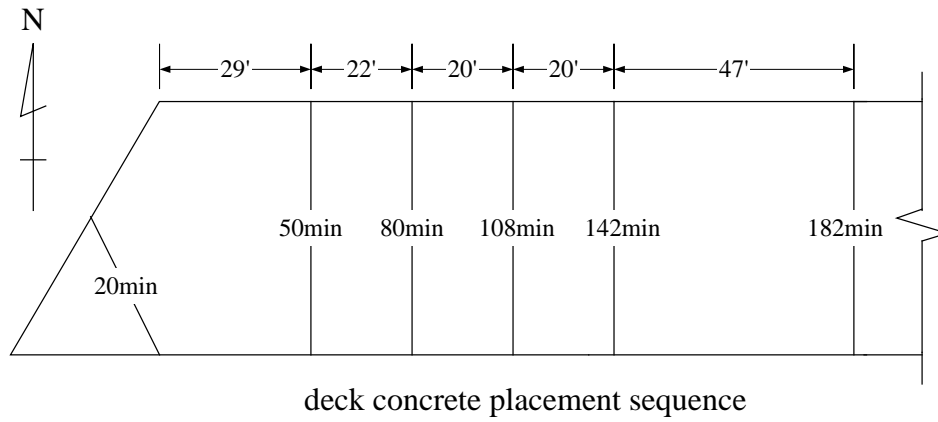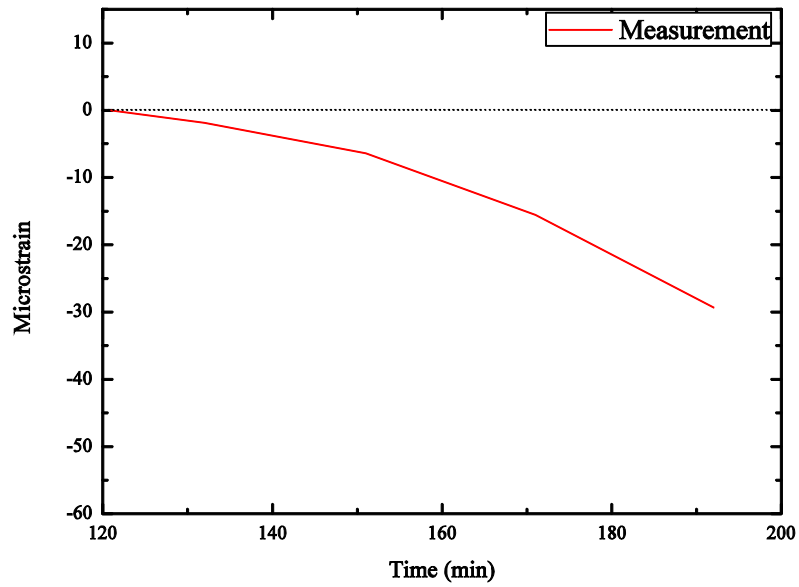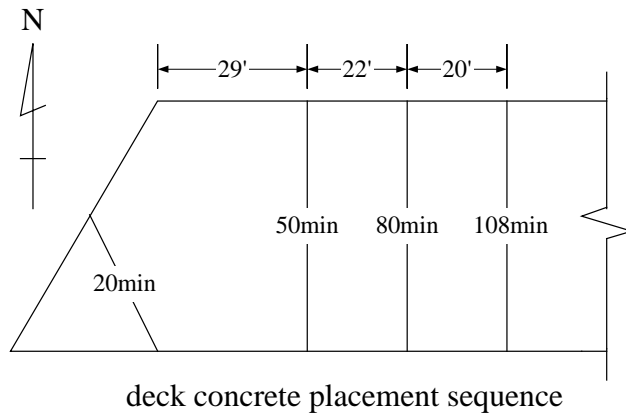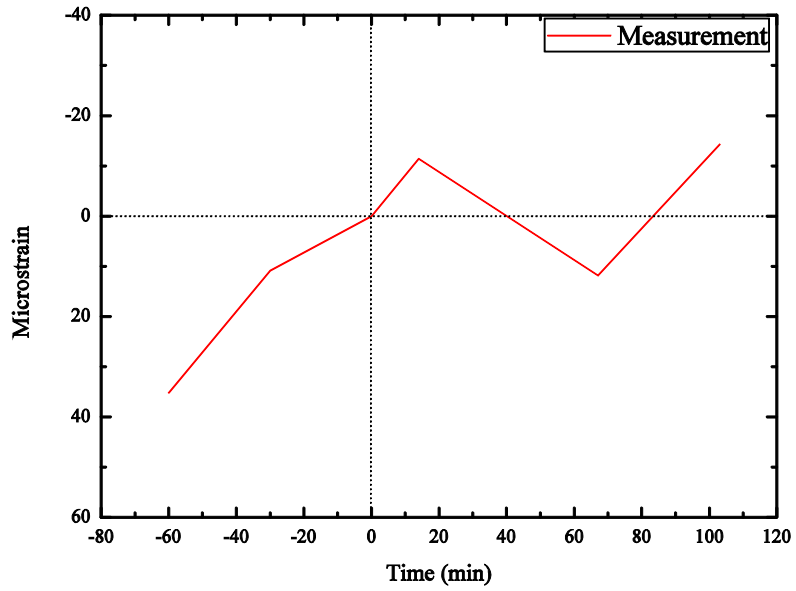Figure 3.18 Strain at "S3 web diagonal" due to concrete deck placement (up to 100 minutes)

deck concrete placement sequence
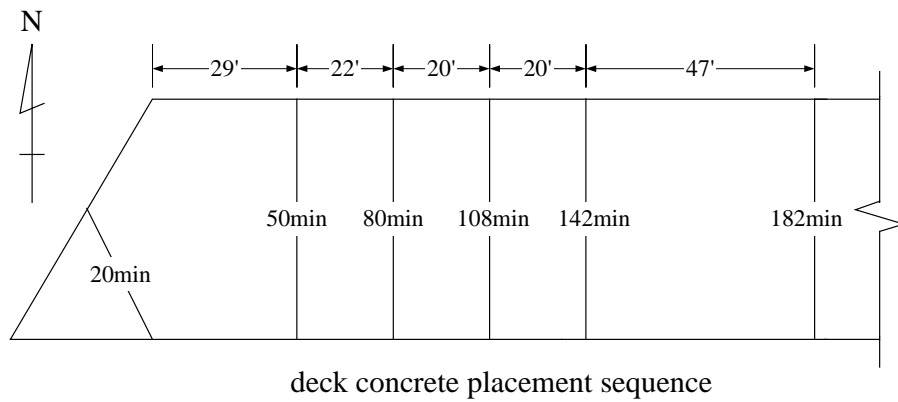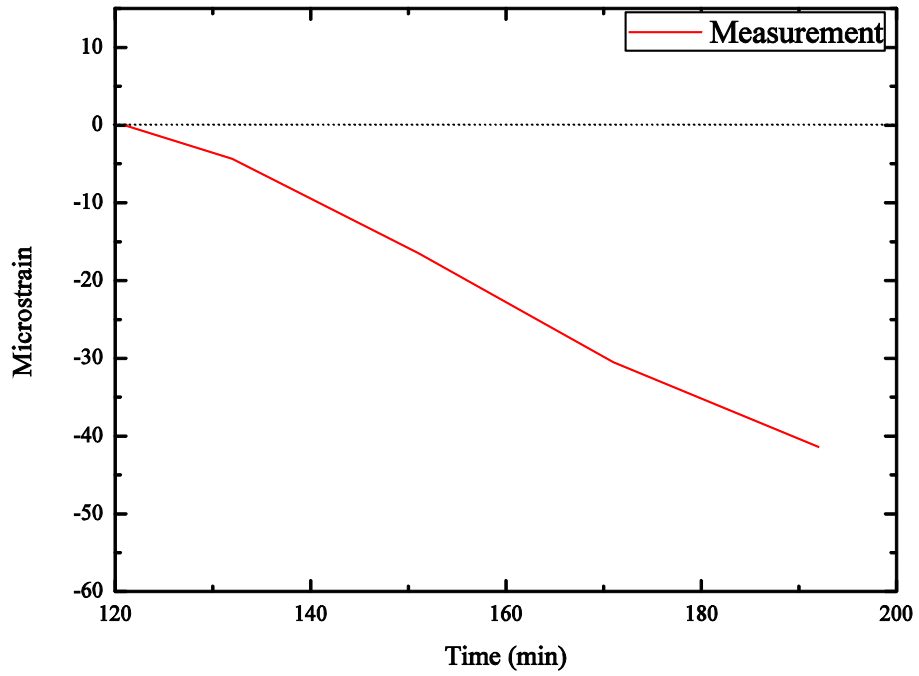
Figure 3.19 Strain at "S3 web diagonal" due to concrete deck placement

(starting from 120 minutes)
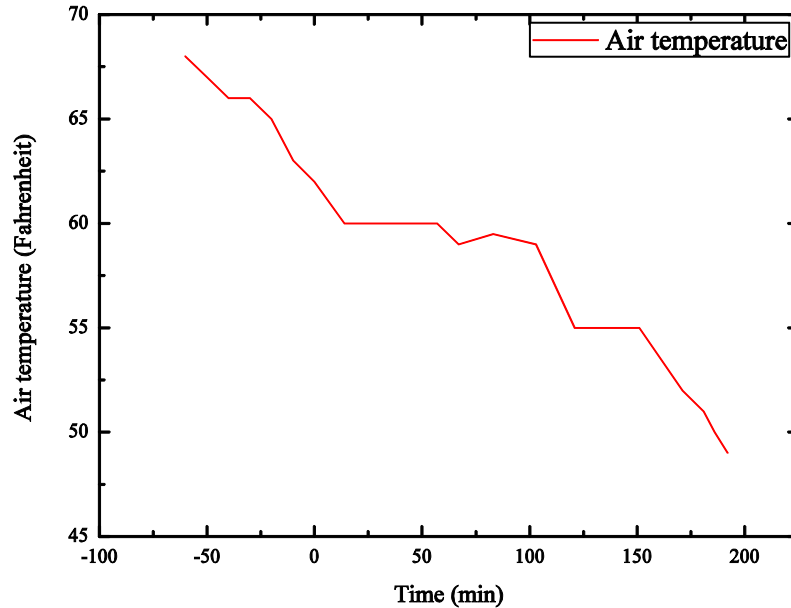
Figure 3.20 Ambient air temperature record

As seen above, two figures for each uni-directional strain transducer are shown (*e.g.*, Figures 3.12 and 3.13 for S1 south, and Figures 3.14 and 3.15 for S2 south, etc). One of them is for the time period from -60 minutes to 105 minutes, and the other from 120 minutes on. This is because data collection was interrupted at 105 minutes, and then was resumed at 120 minutes. Since electrical strain gage reading is relative to the zero set at the commencement, the resumed strain reading lost the original zero setting and had to start from another zero set then. Therefore the second figure starts at 120 minutes with a strain of new zero.

These results show that compressive strain was experienced at the bottom flange locations S1 and S2 before concrete was placed. It is believed that this compressive strain was

due to temperature dropping shown in Figure 3.20. It is seen that this temperature effect is not negligible. For example, Figure 3.14 indicates about 50 microstrains of compressive strain due to a temperature decrease of less than 10° F over about an hour of time. For comparison, the maximum tensile strain was about 80 microstrains due to two legal truck loads to be discussed later.

Furthermore, to understand the temperature effect, the temperature readings in Figure 3.20 should be used as a reference. Rapid temperature decrease was observed before concrete was started to be placed on this span and it corresponds to the observed compressive strain. Nevertheless, it should be noted that the temperature on the girder may be different from the ambient air temperature recorded because heat had to take some time to dissipate from the steel girder heated during the day and thus the girder may be hotter than the ambient temperature during these early evening hours before concrete placement. Accordingly, it is challenging or difficult to find the temperature effect precisely by analysis based on the measured air temperature alone. This subject will be discussed further in Chapter 4 for FEA modeling calibration.

3.3.2 Live load effect

In addition to measuring the dead load effect due to the concrete deck, truck load was also applied to measure the girders' strain response. Strain reading was taken with truck load driven on and off the test span to obtain truck load response at the strain-gaged locations. For each test, one or two trucks were driven through the span or to the predetermined locations on

the span.   The loading paths were designed to maximize the strain due to bending, warping torsion, and shear in the instrumented girders.

Figure 3.21 shows the two trucks with 3-axles used to load the Woodruff Bridge for strain reading purpose. The left and behind truck is referred to as the "white truck" and the right and ahead truck as the "red truck" hereafter in this report. Before loading the bridge, the axle weights and spacings were measured and recorded to be used in the FEA. This information is documented in Figure 3.22.

Figure 3.21 3-axle trucks used to load Woodruff Bridge
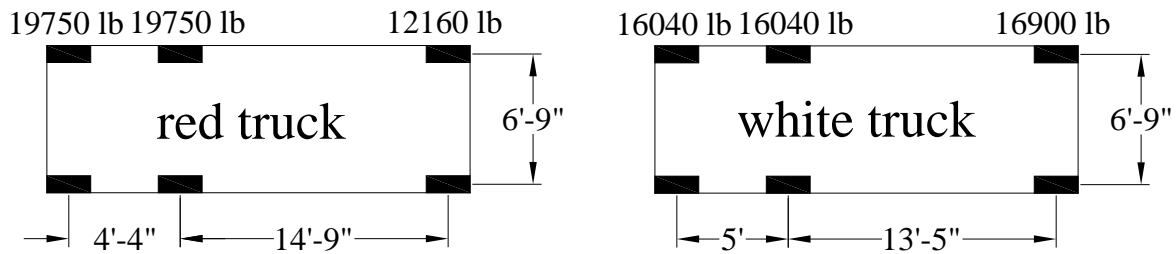
Figure 3.22 Details of 3-axle loading trucks in Figure 3.21

In this live load test program, a total of five loading paths or locations were used to respectively induce maximum strains at the different instrumented locations on the girders. They are referred to as 5 different tests and are presented next with details.

Test 1

In this test, the red truck was driven through Span 1 from the west end of the bridge towards east. Figure 3.23 shows the truck movement direction and path along the instrumented Girder C. This test was selected to maximize the moment effect of the girder at "S1 south" and "S1 north" on the two sides of the flange of Girder C at location S1 (Figure 3.8). This test was repeated four times to generate adequate replicates for verifying consistency. The strain records are shown in Figures 3.24 and 3.25 respectively for the two strain transducers "S1 south" and "S1 north". Note again that the strain transducer identifications and locations on the girder have been given in Figure 3.6.
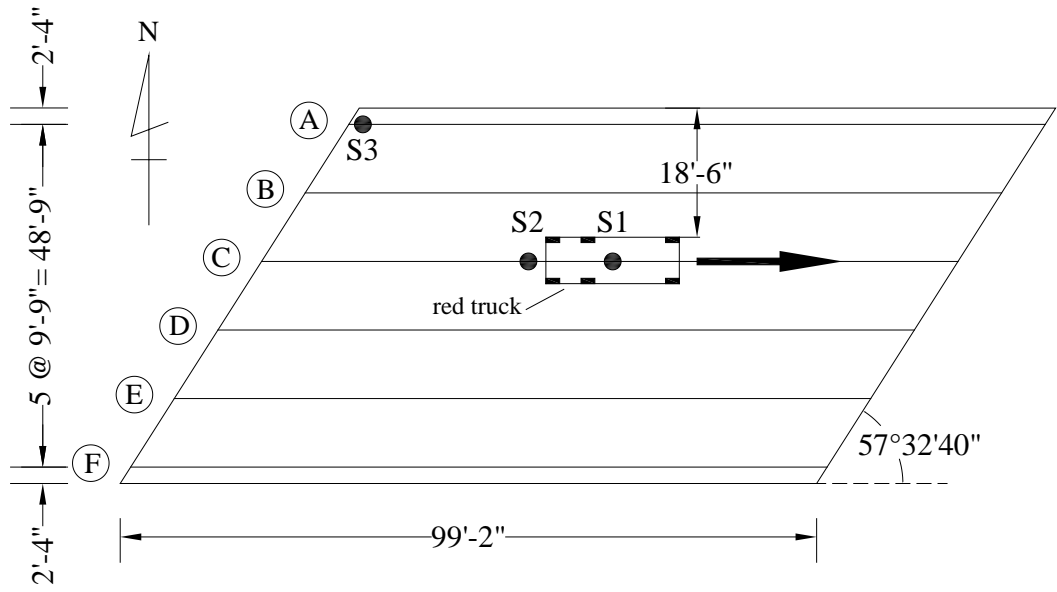
Figure 3.23 Loading path of Test 1
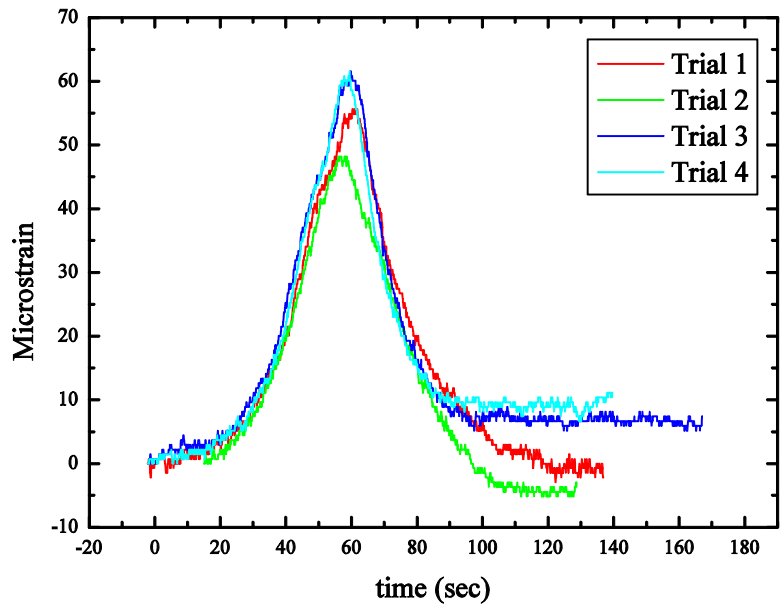
Figure 3.24 Strain at "S1 south" due to Test 1 load in Figure 3.23
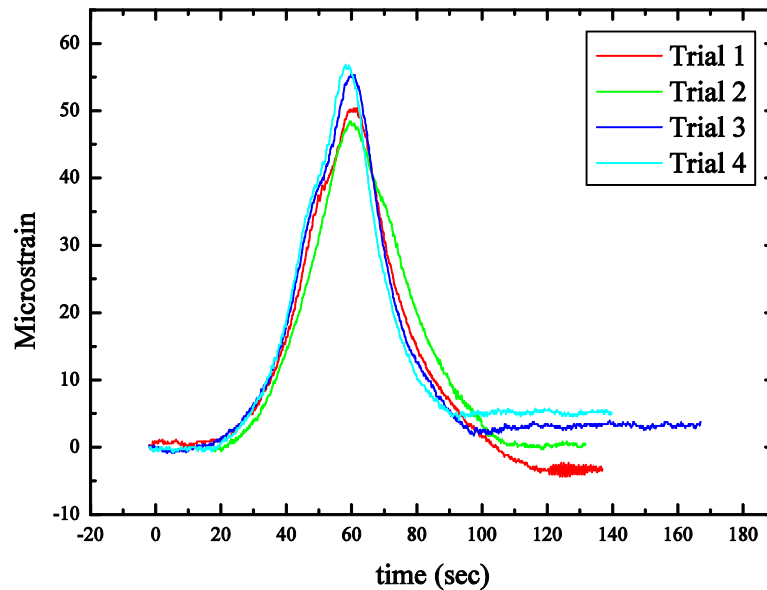
Figure 3.25 Strain at "S1 north" due to Test 1 load in Figure 3.23

These strain records show that strain reading was largely consistent, though small differences are observed. These differences might have been caused by the differences in the truck driven along different paths on the deck. Though the truck driver was instructed to follow the same marked path, it was impossible to exactly realize the same path and the deviation could be 1 ft or so in the transverse (north-south) direction.

Test 2

In this test, both loading trucks were used to load Span 1. After starting from the west end, the trucks were stopped at 60 ft from the west end without going through the entire span, as shown in Figure 3.26. This was to create a side-by-side loading considered to be critical for moment design and to generate a maximum bending strain at location S1. Accordingly, the

45

white truck was driven first to the predetermined location and was parked there, and then the red truck was driven on the span and stopped at its own target location indicated in Figure 3.26. This test was repeated three times and the results are shown in Figures 3.27 and 3.28.
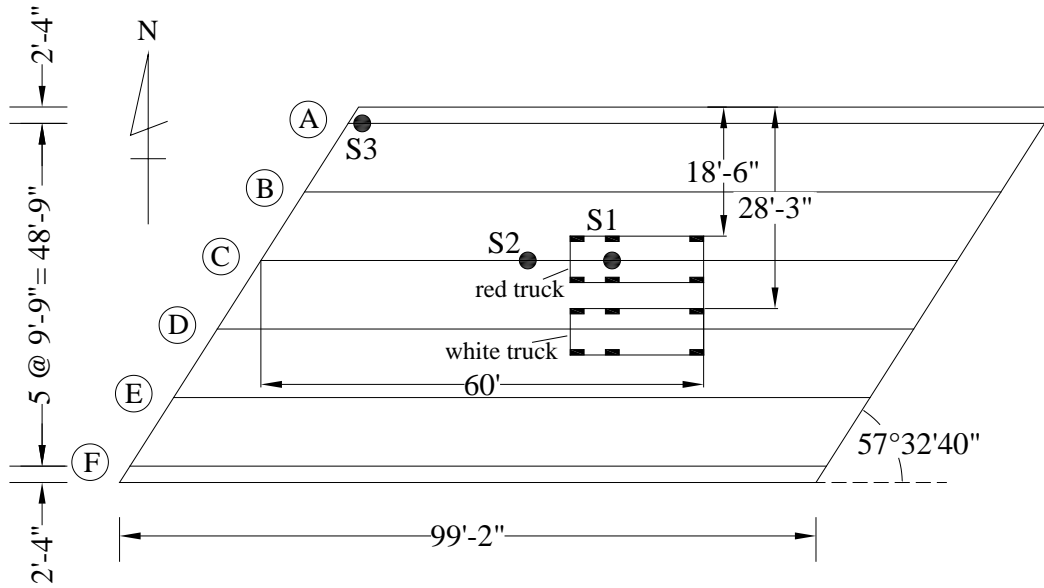

Figure 3.26 Truck load configuration and location of Test 2
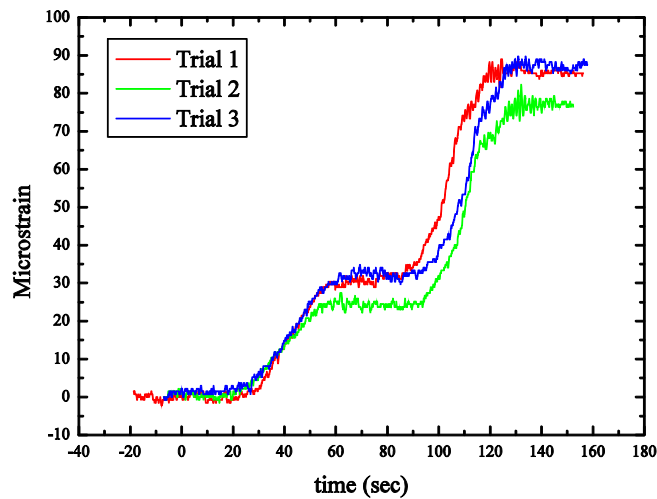
Figure 3.27 Strain at "S1 south" due to Test 2 truck load in Figure 3.26

46
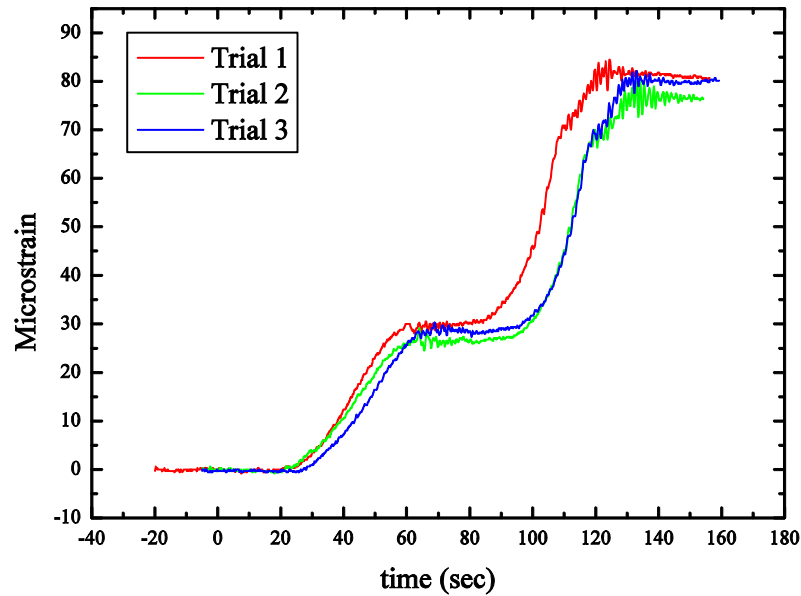
Figure 3.28 Strain at "S1 north" due to Test 2 truck load in Figure 3.26

The two flat parts in the strain records in Figures 3.27 and 3.28 correspond to the white and red truck respectively driven to the target locations and parked there. The oscillatory responses at these two parts were due to the truck taking the breaks to stop and the vibration induced thereby. It is observed that the red truck contributed more strain than the white one, apparently because it was closer to the instrumented Girder C. On the other hand, the contribution of the white truck is certainly not insignificant and in the same order of magnitude since the red truck directly loading Girder C. This situation is different from the shear and torsional effect tests to de presented below.

47

Test 3

This test used one truck (the red truck) to load through Span 1 from the west end to the east. Figure 3.29 shows the transverse location of the loading path. This test was designed to observe the maximum torsional effect in Girder C and thus the strain at "S2 web diagonal". This test was repeated four times and the strain records are shown in Figure 3.30. Quite consistent recording is seen there, as well as high resolution of data acquisition mainly due to the radio-wave based system.
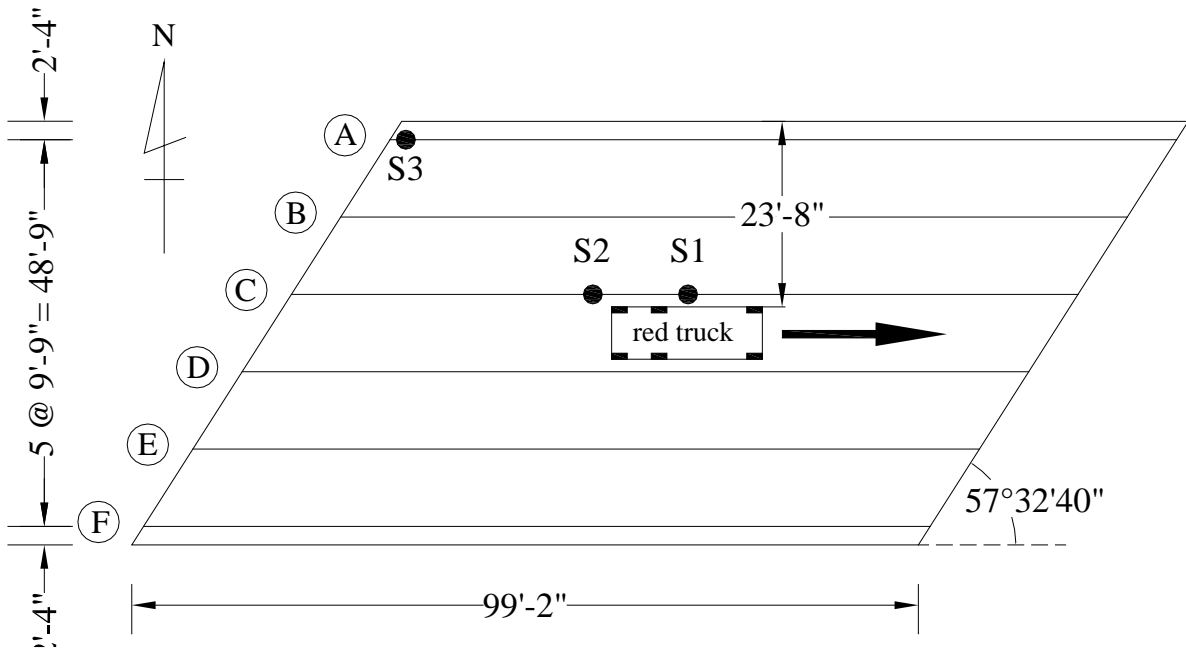
Figure 3.29 Loading path of Test 3
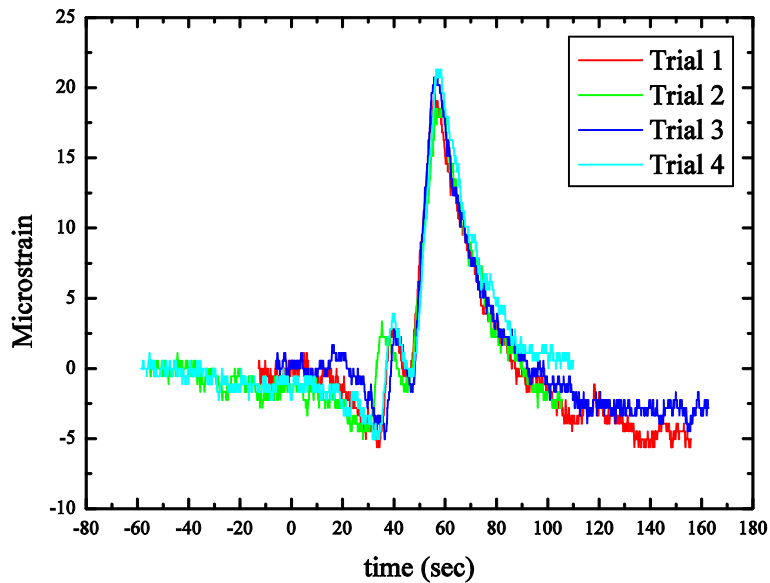
Figure 3.30 Strains at "S2 web diagonal" due to Test 3 truck load in Figure 3.29

Test 4

This test consisted of both trucks loading to the same location as Test 2 but transversely off by a half of a lane. Accordingly, the white truck was first driven to the target location and parked there, and then the red truck was driven to its target location as indicated in Figure 3.31. This test configuration and location was also determined to maximize the torsional effect in Girder C and thus the strain at "S2 web diagonal". This test was repeated three times for replicates and the strain records are plotted in Figure 3.32.

49

Figure 3.31 Truck load configuration and location of Test 4
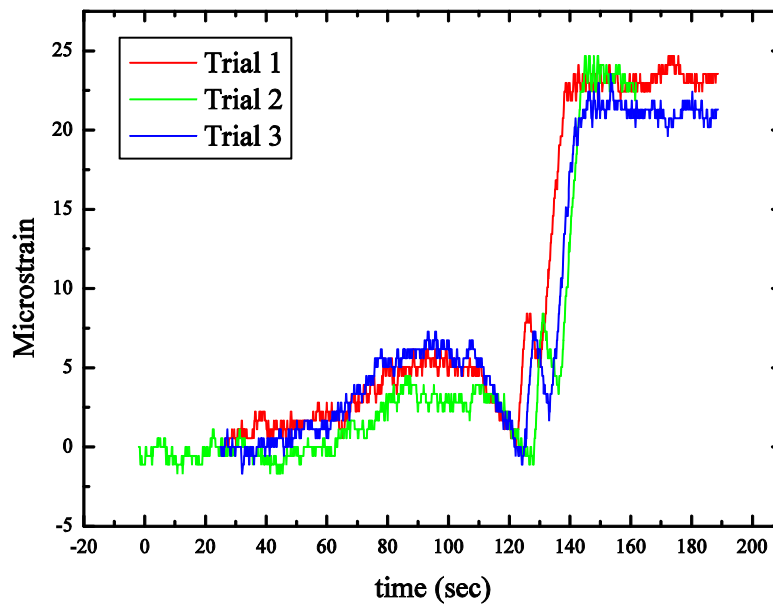
Figure 3.32 Strain at "S2 web diagonal" due to Test 4 truck load in Figure 3.31

Figure 3.32 shows that the white truck driven first to the target location contributed approximately 5 microstrains and stopped at around 100 seconds. The white truck apparently contributed much less significantly because it was further away from Girder C where the strain was read. Then, the red truck was driven on to the target location, superimposing more significantly about 20 more microstrains. Comparing Test 4 with Test 3 (Figure 3.32 with Figure 3.30) it is seen that the additional white truck's contribution is very limited, apparently due to a significant load sharing by Girder D.

Test 5

Test 5 also used both trucks for maximizing shear at the obtuse corner of the bridge. The red truck was driven first to the target location marked in Figure 3.33 and parked there, and then the white truck followed to its own target location also marked in Figure 3.33. This test was also intended to induce a maximum shear strain at "S3 web diagonal". Three strain reading replicates were acquired for this teat and they are exhibited in Figure 3.34.

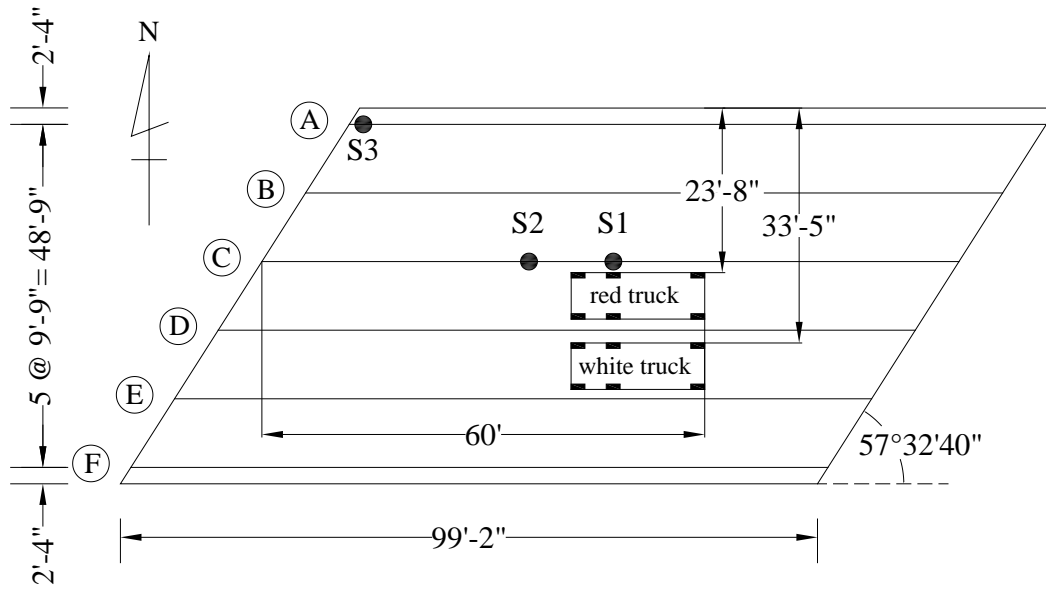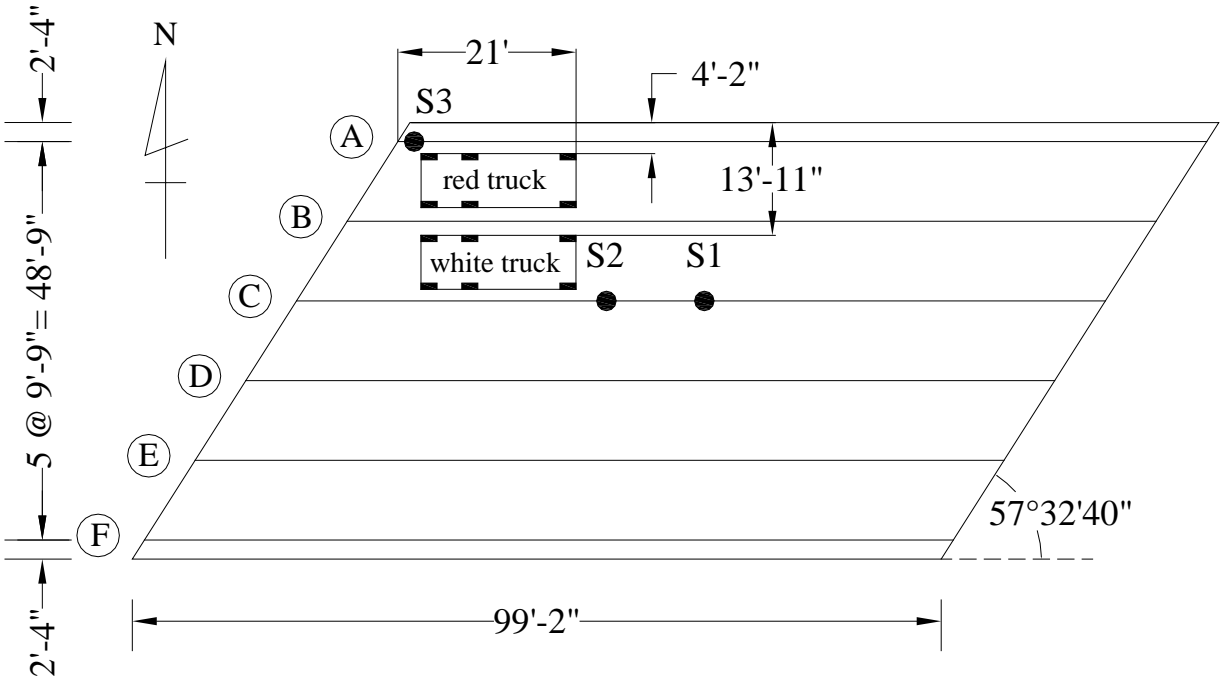Figure 3.33 Truck load configuration and location of Test 5
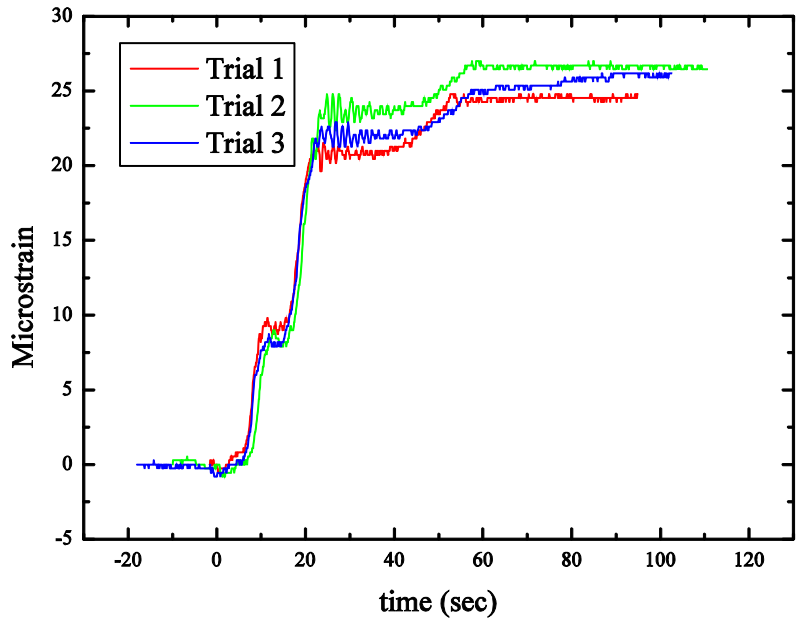
Figure 3.34 Strain at "S3 web diagonal" due to Test 5 truck load in Figure 3.33

Three obvious steps of strain increase are seen in Figure 3.34, between about 0 to 10 microstrains, 10 to 22 microstrains, and 22 to 26 microstrains. These three steps corresponded to the front axle of the red truck, the rear tandem axle of the red truck, and the entire white truck in the adjacent lane, respectively. The red truck which was driven right next to the fascia beam contributed significantly more as seen. Compared with Test 4, both tests involved a second truck in an adjacent lane that actually superimposed a very limited amount of additional strain.

3.4 Summary

This chapter has presented the process and results of the field test program to provide measurements of strain effect resulting from the concrete deck placement as dead load and truck load as live load. The strain readings also provide some insight to the behavior of skewed bridges.

In the dead load test, temperature strain effect is seen to be not negligible compared to the observed dead load effect and live load effect.

In the live load test, five loading tests were performed to induce possibly maximum strains in different strain reading locations. All tests were repeated three or four times, and consistent measurement results were obtained. The second truck in an adjacent lane contributes more additional response for bending strain than for shear and torsional strains.

Besides the light shed on the behavior of skewed bridges, these test data are to be used next to calibrate and validate FEA modeling used in Chapter 5.

Chapter 4

Finite Element Analysis Modeling and Calibration

Physical measurement can only be performed on a limited number of structures and at a limited number of perceived critical locations. However, these measurements are important and can be used to calibrate numerical modeling of the measured structures to provide validation. FEA is considered the most generally applicable and powerful tool for such modeling and analysis. This chapter first presents the developed finite element model for the test bridge and then the process and the results of validation and calibration using the measured data from the Woodruff Bridge.

4.1 FEA modeling

GTSTRUDL, a 3-D FEA software program, was used in this study to perform the required analysis. This section presents the process of modeling along with model details and next section will discuss the process of validation using the measured data presented earlier in Chapter 3.

4.1.1 Selection of modeling elements

In the analysis covering dead load effect of the concrete deck and live load effect of truck load, the 3-D linear solid element IPLS of the GTSTRUDL program was used to model the concrete deck, steel girder, bearing, intermediate diaphragm, and end diaphragm. The reason for

this selection was to be able to model certain details that other simpler elements cannot model as commented on in Chapter 2. For example, when the beams are modeled using beam elements as done in some previous research efforts reported in the literature, it will be difficult or too much time consuming to place the intermediate diaphragms at the right locations other than the neutral axis of the beam. IPLS in GTSTRUDL is an 8-nodes iso-parametric solid brick element as shown in Figure 4.1. It is based on linear interpolation and Gauss integration. The basic variables on a node are the translations u_x, u_y, and u_z in the three orthogonal directions.
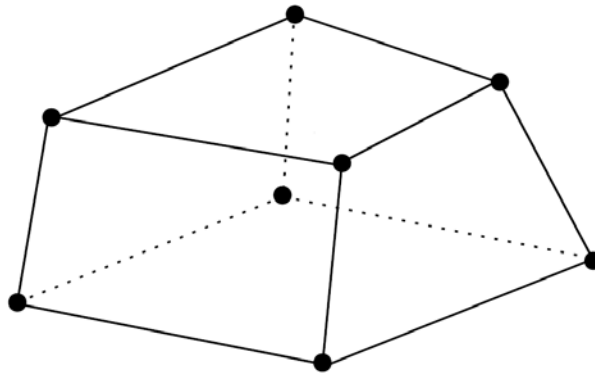
Figure 4.1 GTSTRUDL 3-D solid element IPLS

4.1.2 Material properties

The FEA model of the Woodruff Bridge is divided into 5 structural parts, the deck, girders, bearings, intermediate diaphragms, and end diaphragms. The deck and end diaphragms are made of reinforced concrete, the girders and intermediate diaphragms are made of steel, and the bearings are made of synthetic rubber or elastomer with steel reinforcing plates. Detailed information for each material is shown in Table 4.1.

Note that the Young's modulus of concrete E_c in Table 4.1 is derived from the following equation (AASHTO).

$$E_c \text{ (psi)} = 57000\sqrt{f'_c \text{ (psi)}}$$

where f'_c is the compressive strength of the concrete and 4,344 psi was used in this modeling effort, obtained from compression tests of cylinders taken from the concrete batches placed in the deck of the test bridge.

Table 4.1 Material properties used in FEA modeling

	Young's modulus (ksi)	Poisson's ratio
Concrete	3757	0.2
Steel	29000	0.3
Synthetic rubber	11	0.4

4.1.3 FEA modeling of the Woodruff Bridge

Figure 4.2 below shows the finite element model of the Woodruff bridge (isometric view) using 70,969 elements and 44,331 nodes. Figure 4.3 displays the top view of Span 1 that was tested. It is seen in Figure 4.2 that the element mesh of Span 1 is finer than Spans 2 and 3 to allow a higher resolution of analysis. Span 4 of the structure was not included in the model to reduce computational cost since Span 4's effect to Span 1 to be focused on was considered negligible.
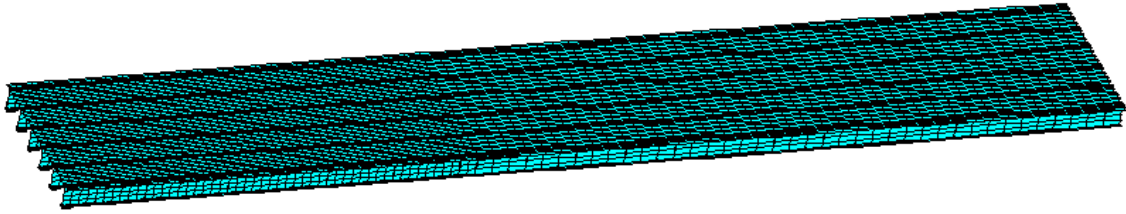
Figure 4.2 Isometric view of FEA model of Woodruff Bridge
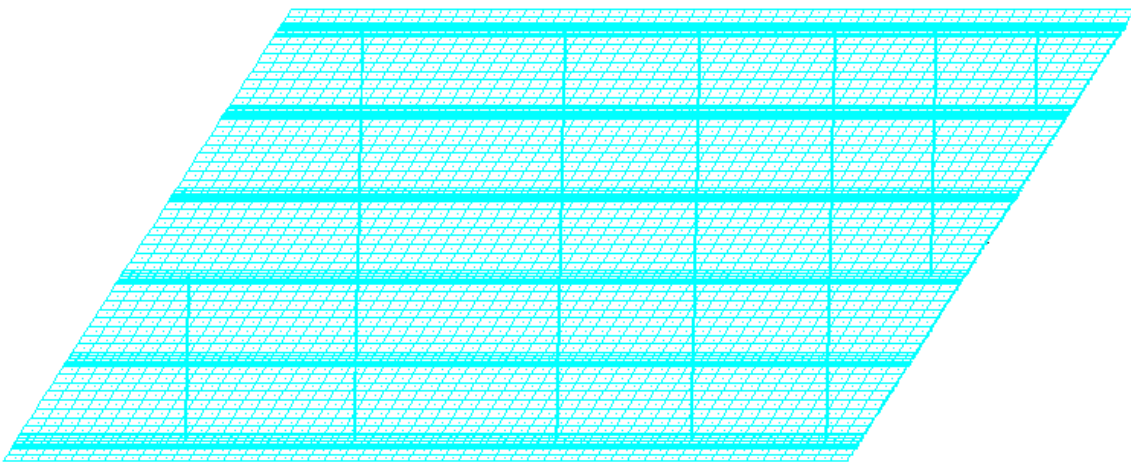
Figure 4.3 Top view of Span 1 FEA model of Woodruff Bridge

For illustration, typical examples of strain contour plots are shown in Figures 4.4 to 4.6. Figure 4.4 shows the top view of Span 1, Figure 4.5 highlights the bottom flange at the midspan where the maximum strain is experienced, and Figure 4.6 shows the lateral view at the obtuse corner. Load specific analysis results are to be discussed below.
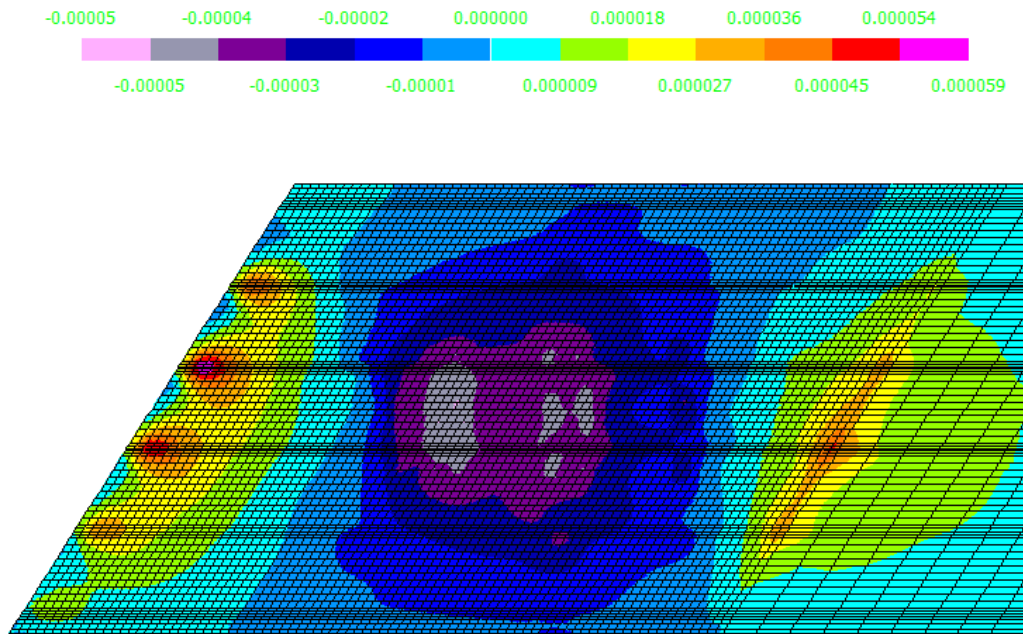
Figure 4.4 Typical strain contour plot of Span 1
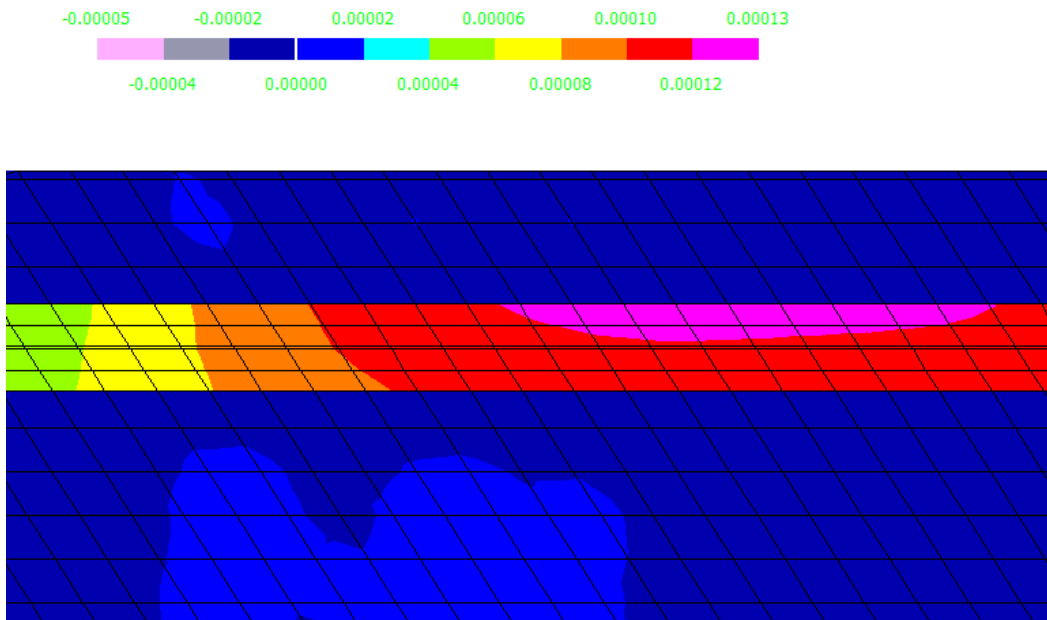
Figure 4.5 Typical strain contour plot of a beam's bottom flange at midspan
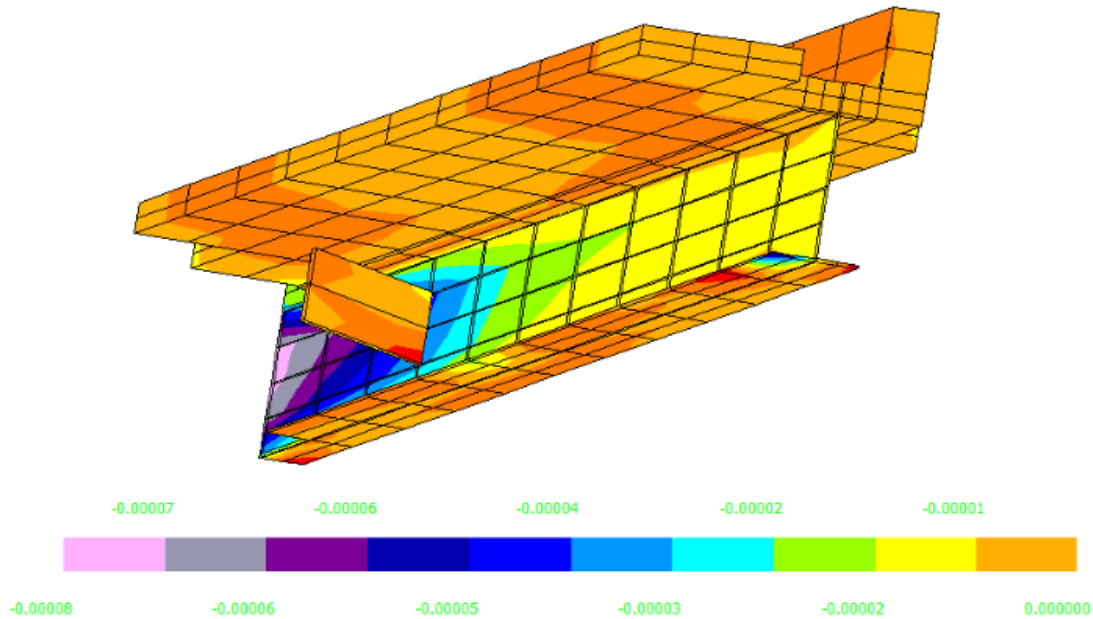
Figure 4.6 Typical strain contour plot for the obtuse (left bottom) corner

4.2 Validation and calibration of FEA model using measured responses

4.2.1 Validation and calibration

The validation of FEA modeling started from checking mesh convergence in this project. Several different meshes were used to finalize to the one presented above upon confirmation of convergence.

The calibration of FEA modeling used the measured deck dead load and truck live load effects as the reference for confirmation decision making, which have been presented in Chapter 3 and acquired by measurement from the Woodruff Bridge field tests. In this process, it was found how to model the intermediate and end diaphragms may affect the computed strain

responses to a great extent. Nevertheless several publications in the literature have asserted that the effect of these diaphragms are limited (*e.g.,* BridgeTech 2007). The reason for this discrepancy is perhaps that the diaphragms in the Woodruff bridge are large and thus significantly more stiff than those used in many other highway bridges.

Several intermediate diaphragms of the Woodruff Bridge are photographed in Figure 4.7. The depth of the intermediate diaphragms is approximately 3/4 of the steel girder web depth. As a result the diaphragms possess a high stiffness compare with traditional cross frames. Their influence is particularly noticeable in analyzing the concrete deck dead load before the deck hardens and then participates in load distribution for live load.

Figure 4.8 shows a photograph of the west end diaphragm of the test bridge in Monroe Count, Michigan. This end diaphragm is made of reinforced concrete and as thick (in the traffic direction) as the back wall of the abutment that the bearings and in turn the girders site on. It is seen to have the ends of the steel girders embedded in it including even the elastomeric bearings. As a result, the end diaphragm practically provides a very rigid support for the steel plate girders, although the design assumption for this end is simple support. The discrepancy between the design assumption and the field condition has lead to significant differences in computed and measured strains. Accordingly, two different support conditions were used in FEA to investigate further. More details on this subject are presented in the following sections depending on which strain response is focused on. One assumption is simple support condition and thus consistent with the design assumption. The other one is fixed end condition according to the field observation. Of course neither of them is the real support condition, while the field condition is much closer to the fixed end one for the service load, which was the applied test load whose responses are used here as the reference for calibration.

Figure 4.7 Intermediate diaphragms of Woodruff bridge

Figure 4.8 The reinforced concrete end diaphragm / back wall of the Woodruff Bridge

4.2.2 Dead load effect

Figures 4.9 to 4.16 show comparison of the deck dead load effect results by FEA using GTSTRUDL and measurement using the instrumentation presented in Chapter 3 for the test bridge. In the analysis, temperature effect was not included because we did not have the girder temperature and the air temperature alone was considered inadequate for strain analysis. As presented in Chapter 3, each strain location has two figures, one for the time period from 60 minutes before to 105 minutes after the concrete placement starting, and the other from 120 minutes after the concrete placement starting. Note again that the time at concrete placement starting is set at 0 and thus negative time is used for before and positive time for after that starting time.
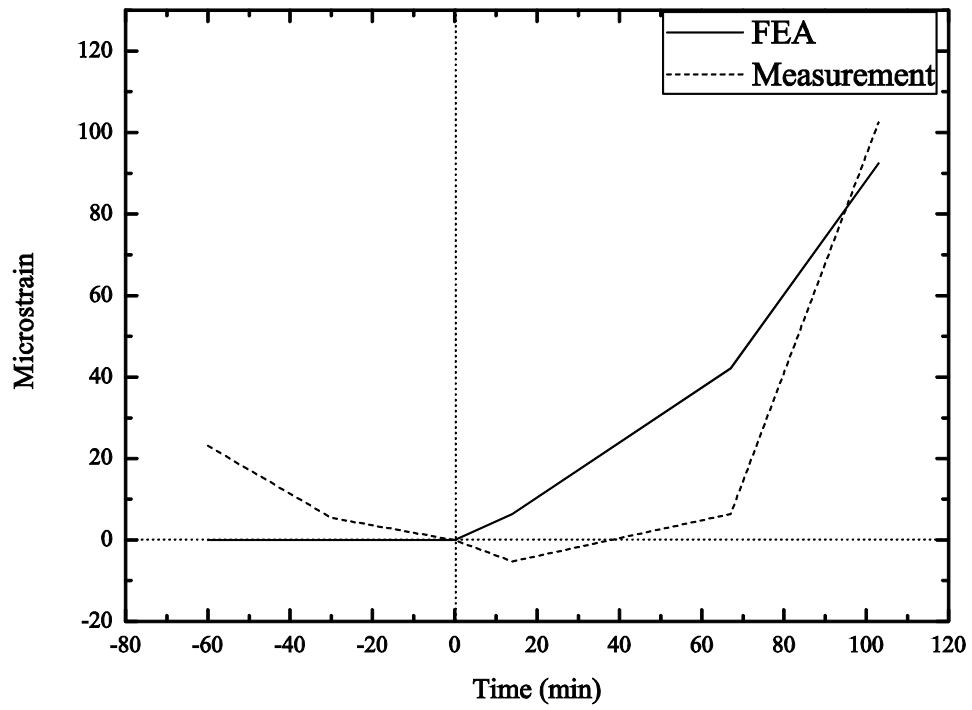
Figure 4.9 Comparison of dead load strains at S1 south (up to 105 minutes)
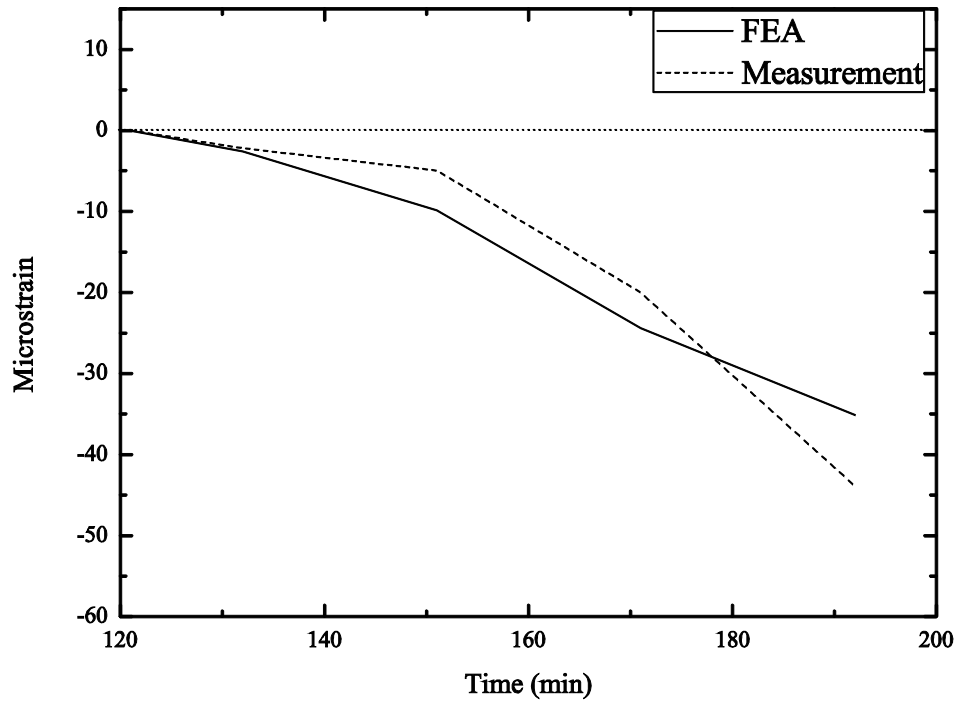
Figure 4.10 Comparison of dead load strains at S1 south (starting from120 minutes)
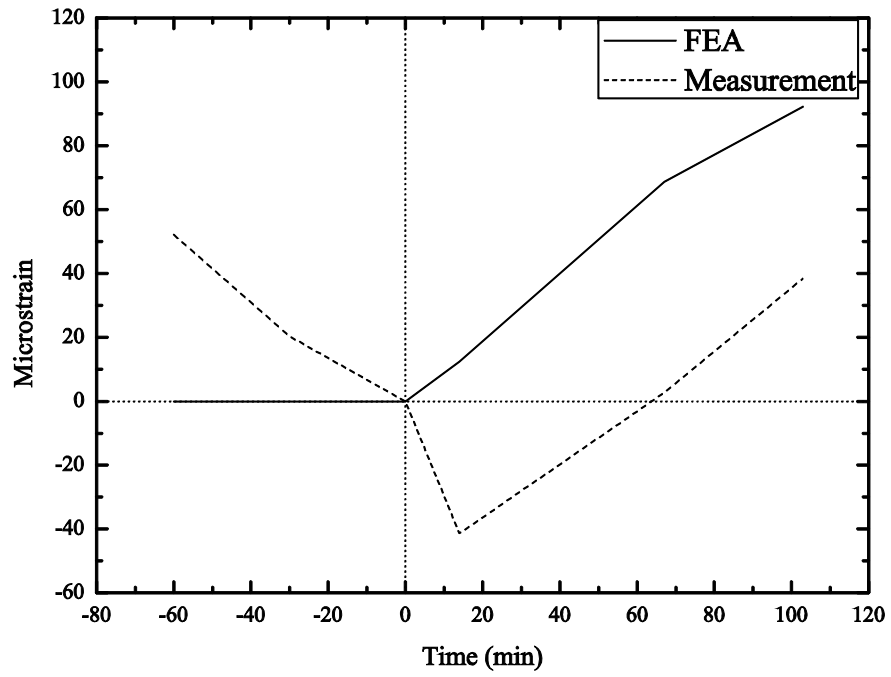
Figure 4.11 Comparison of dead load strains at S2 south (up to100 minutes)
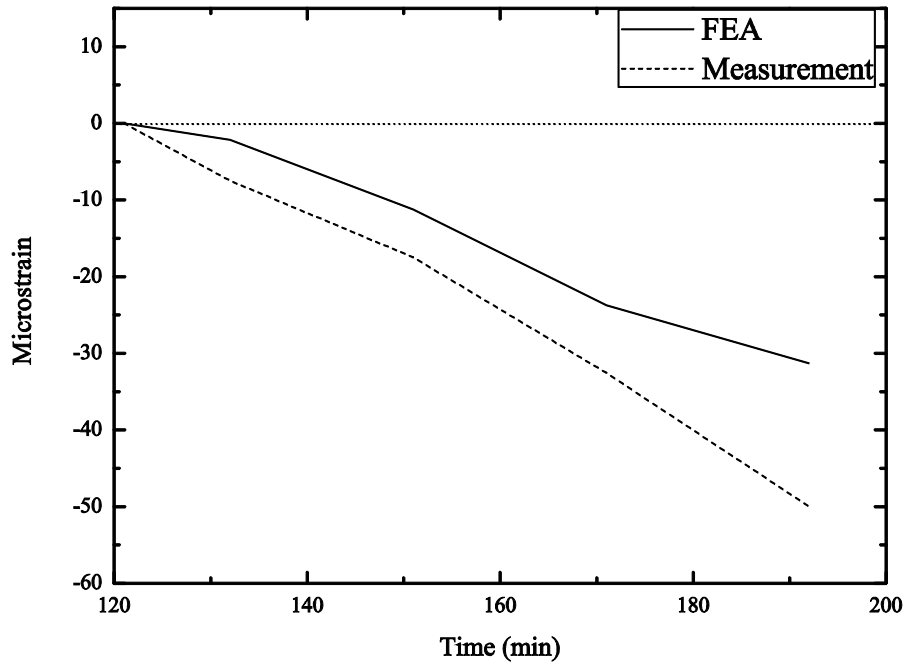
Figure 4.12 Comparison of dead load strains at S2 south (starting from120 minutes)
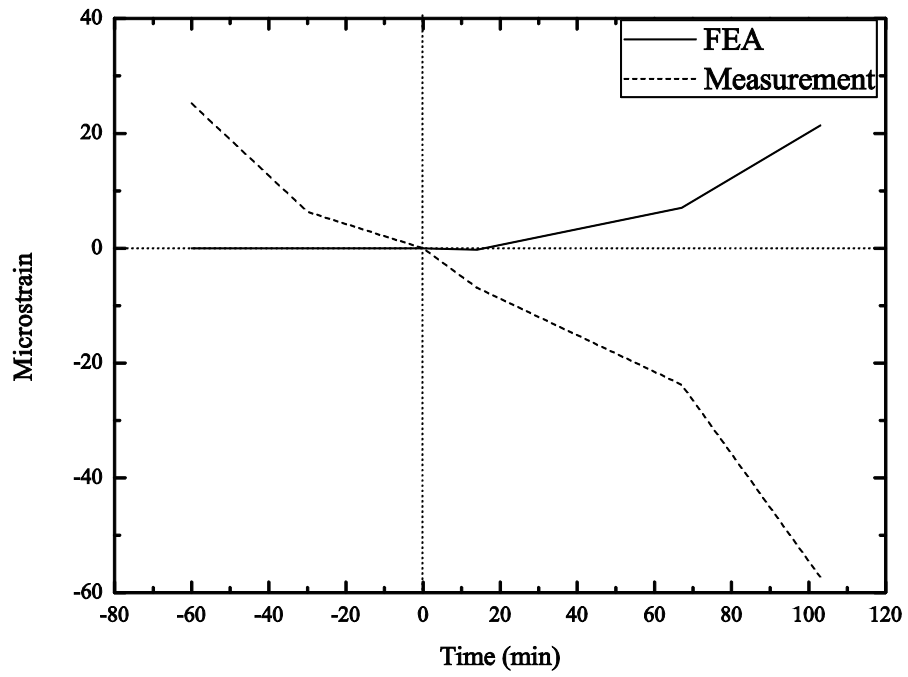
Figure 4.13 Comparison of dead load strains at S2 web diagonal (up to 105 minutes)
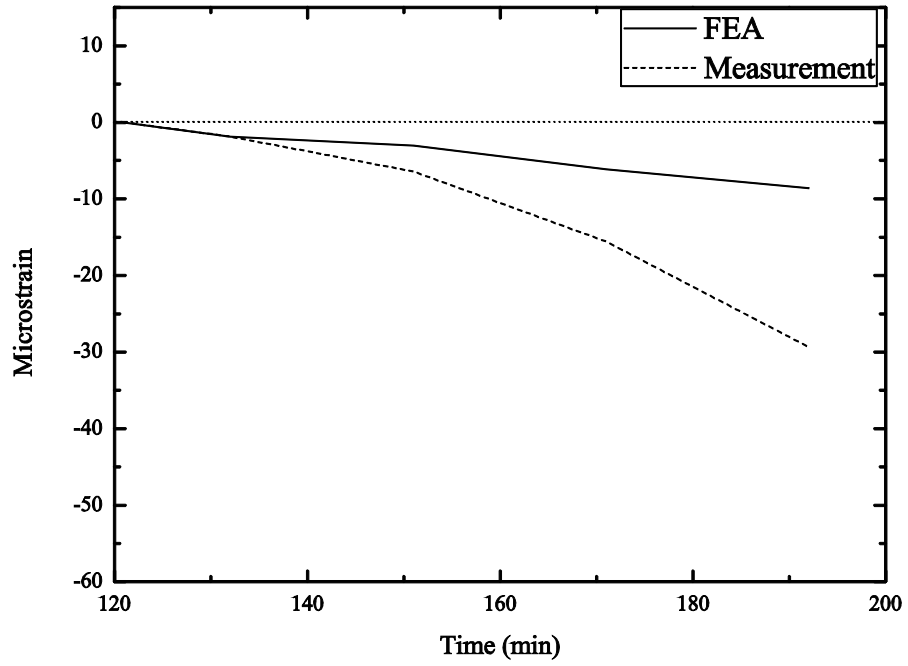
Figure 4.14 Comparison of dead load strains at S2 web diagonal (starting from 120 minutes)
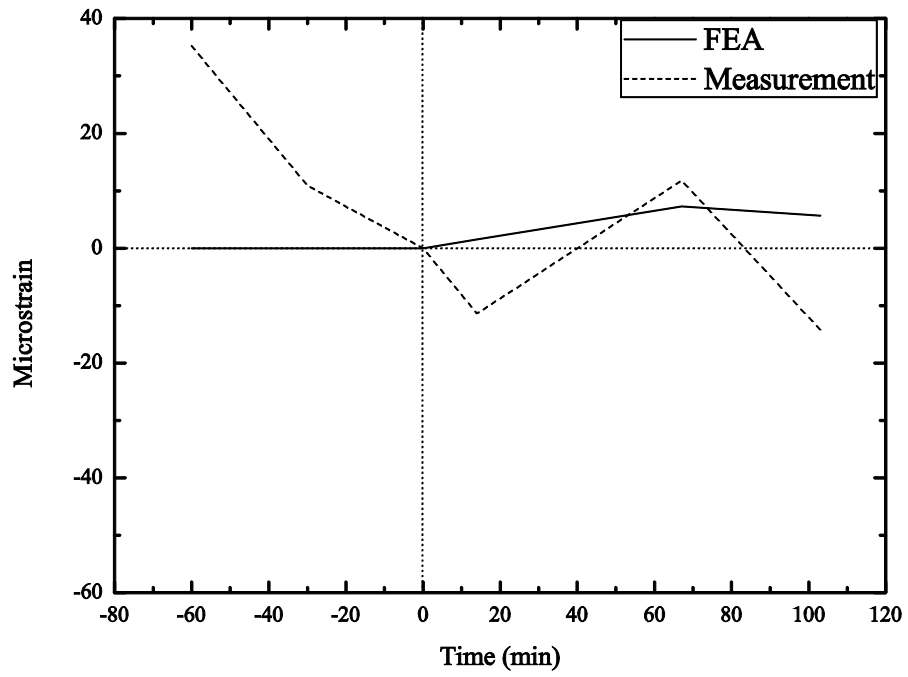
Figure 4.15 Comparison of dead load strains at S3 web diagonal (up to 105 minutes)
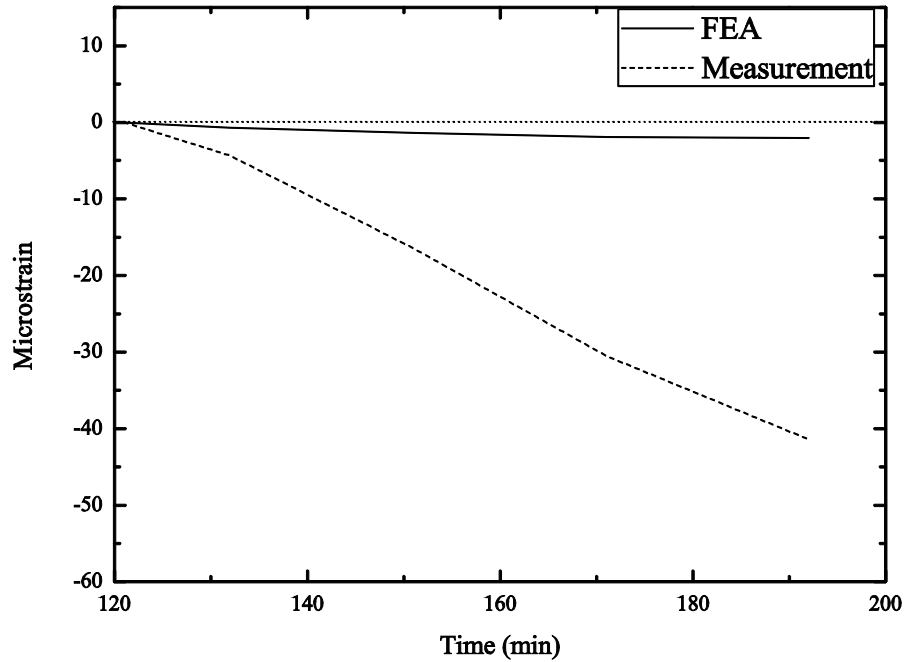
Figure 4.16 Comparison of dead load strains at S3 web diagonal (starting from 120 minutes)

In these figures, the difference between the FEA and measurement results is observed. The reason for the difference is considered to be due to not including the temperature effect in the FEA results. This is consistent with the fact that the measurement results showed generally more compressive strains than FEA owing to monotonic decrease in air temperature in this night concrete pour, conducted according to the Michigan Department of Transportation (MDOT) Standard Specifications for Construction. With this understanding, the calibration of FEA modeling for deck dead load effect concluded here.

4.2.3 Live load effect

As discussed in Chapter 3, five different load tests using different truck load configurations and locations were performed in the field. Accordingly, this FEA modeling calibration was conducted using the field measurement of all of these tests. To reiterate, Tests 1 and 2 had a focus on moment/warping strains, Tests 3 and 4 on torsional strains, and Test 5 on shear strains.

Figures 4.17 to 4.23 demonstrate comparison of the live load strain results by FEA computation and field measurement. It is seen that the FEA results agree very well with the measurement results for these 5 tests, each having 3 or 4 replicates. This has provided evidence for the effectiveness of the FEA modeling effort and approach for the interested load effects moment, warping moment, torsion, and shear. This modeling approach was then extended to a sample of typical new bridge spans in Michigan to observe effect trends of the design factors on skew bridge behaviors and responses.
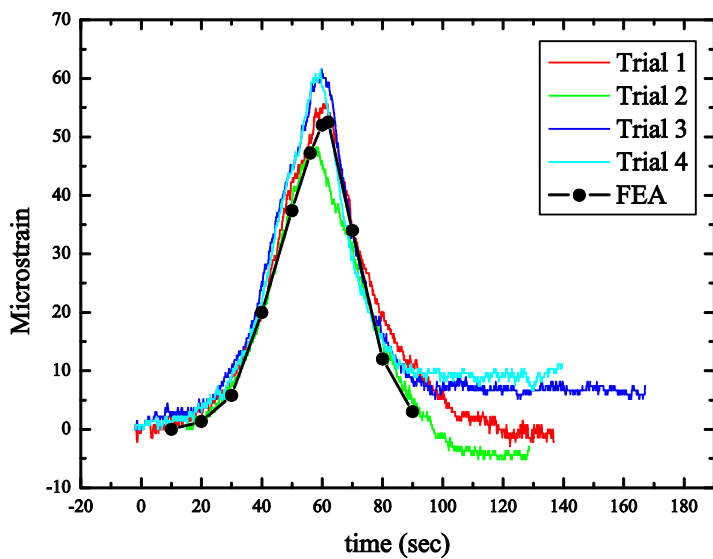
Figure 4.17 Comparison of measured and FEA computed live load strains at S1 south

for Test 1 in Figure 3.23
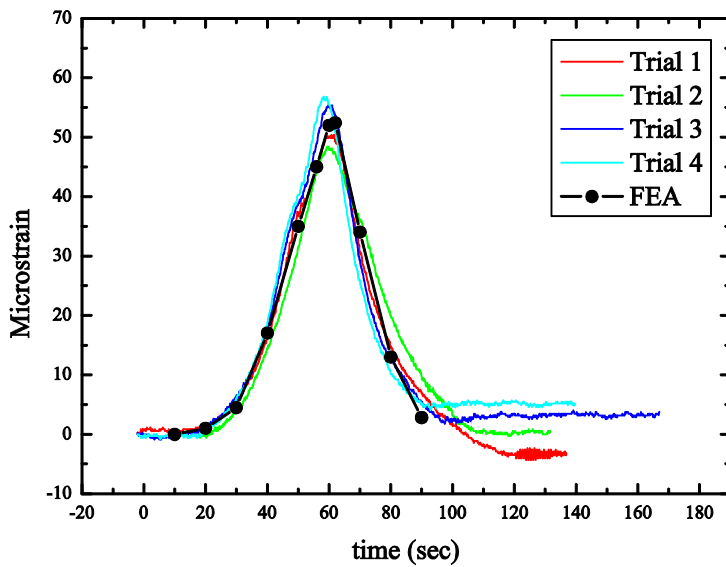
Figure 4.18 Comparison of measured and FEA computed live load strains at S1 north

for Test 1in Figure 3.23

72
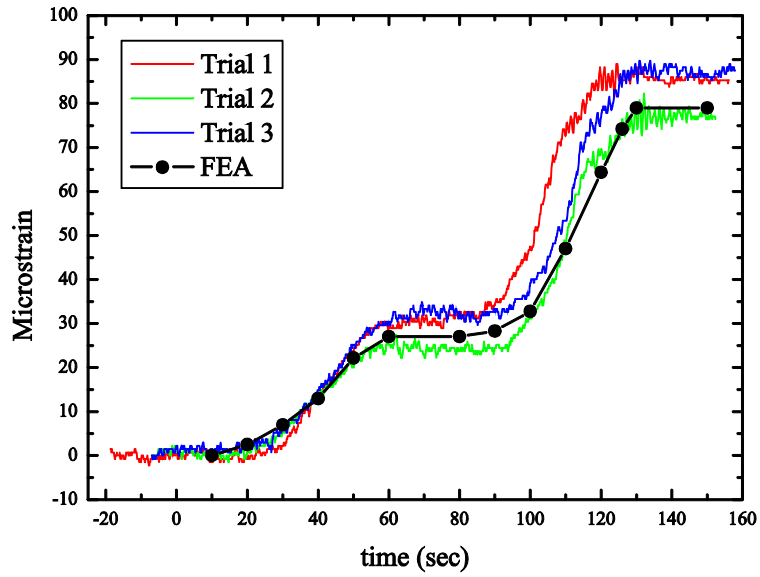
Figure 4.19 Comparison of measured and FEA computed live load strains at S1 south

for Test 2 in Figure 3.26
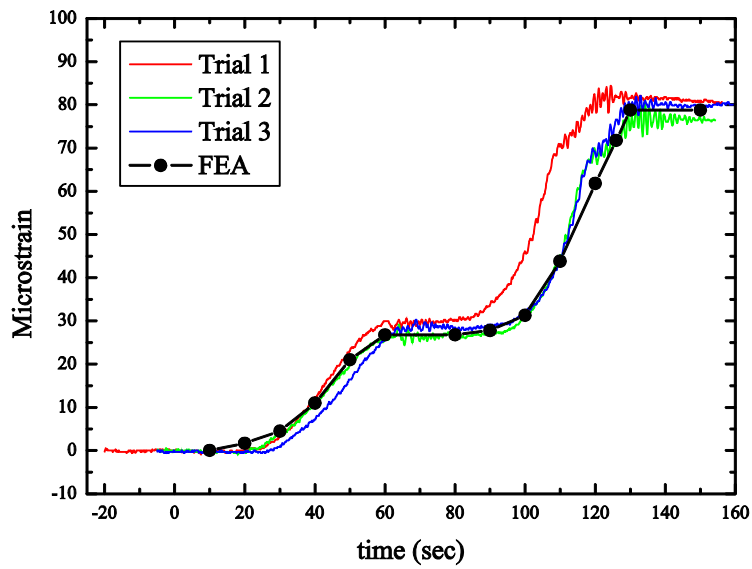
Figure 4.20 Comparison of measured and FEA computed live load strains at S1 north

for Test 2 in Figure 3.26
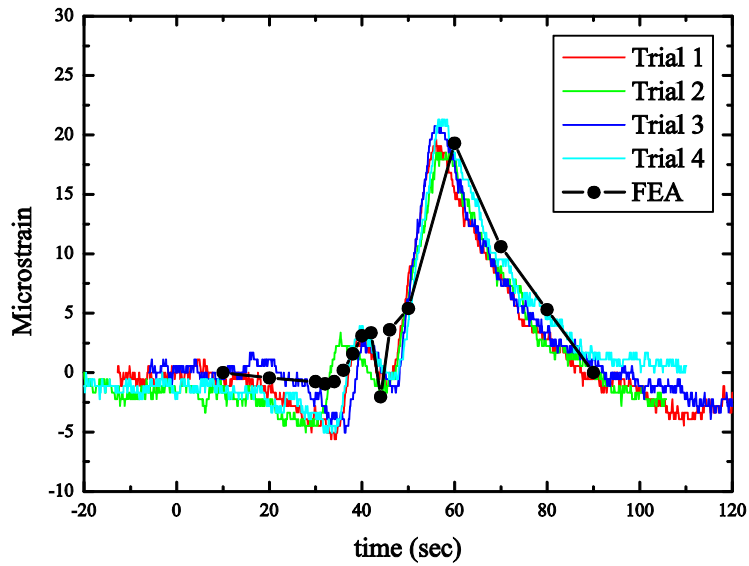
Figure 4.21 Comparison of measured and FEA computed live load strains at S2 web diagonal

for Test 3 in Figure 3.29
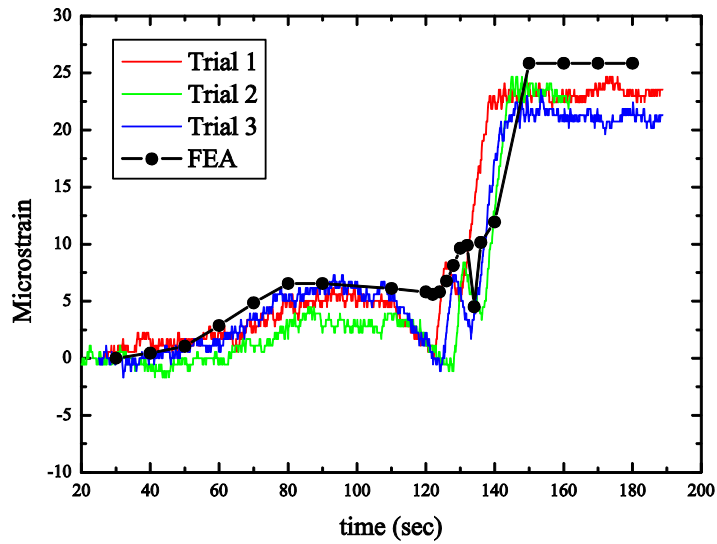
Figure 4.22 Comparison of measured and FEA computed live load strains at S2 web diagonal

for Test 4 in Figure 3.31

74
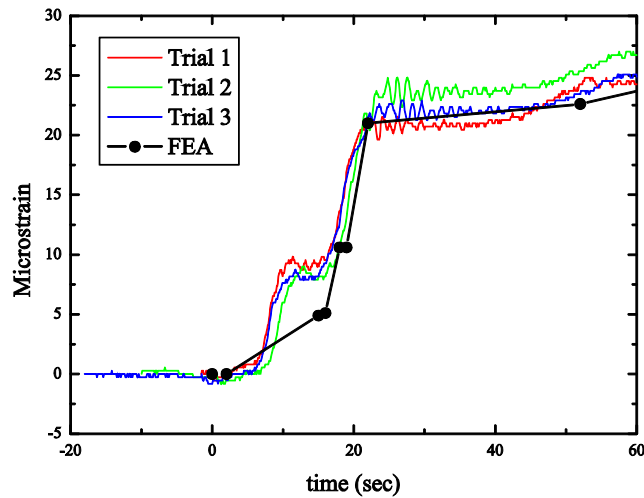
Figure 4.23 Comparison of measured and FEA computed live load strains at S3 web diagonal

for Test 5 in Figure 3.33

4.3 Summary

In this chapter, details of developed finite element model using GTSTRUDL are described first. Element material properties were determined from testing data and mesh size is selected by checking convergence. For all 5 structural components (deck, beams, intermediate diaphragms, end diaphragms / back walls, and bearings), 3-D solid element IPLS is employed to model the Woodruff Bridge in detail. From the calibration process, it is found that the existence of intermediate and end diaphragms / backwalls affect the strain measurement response to a great extent because those of the Woodruff Bridge appear to be larger and stiffer than many other bridges.

The FEA results are compared to measurement results of the deck dead load test and truck live load test. For the dead load test, differences are observed between the FEA and

75

measurement results because the measurement results include not only the dead load effect but also the temperature load effect, although the general trends look consistent between the two sets of strain results.   For the truck live load test, the FEA results agree very well with the measurement results for all five tests and numerous replicates of measurement reading. It is thus concluded that our FEA modeling is reliable and can capture the critical responses of moment, warping moment, torsion, and shear.

Chapter 5

Numerical Analysis Program Using FEA

In Chapter 4, our FEA modeling was validated and calibrated using measurement results of deck dead load and truck live load strains. In this chapter, 18 cases of typical simple span bridges in Michigan are selected, modeled, and analyzed using the validated FEA modeling approach. Moment and shear distribution factors are derived for these bridge spans and are compared to those according to the AASHTO LRFD Bridge Design Specifications. The effect of diaphragms and boundary conditions on the load distribution factors is also investigated. In Section 5.1, parameters and dimensions of the analyzed bridges are provided. Sections 5.2 and 5.3 present the analysis results and discussions of the effect of truck load and thermal load on the behavior of skewed bridges, respectively. A summary is provided in Section 5.4 to conclude the chapter.

5.1 Modeling typical new Michigan bridges

Based on the calibration of FEA modeling discussed in Chapter 4, FEA using GTSTRUDL is performed to 18 cases of simple span composite bridges with six beams. The selected design parameters are exhibited in Table 5.1. Two superstructure types are considered here: steel I and prestressed concrete I beams supporting a composite reinforced concrete deck. These bridge types were selected based on an MDOT bridge inventory search showing them to be the top two types of new bridges constructed in Michigan in the recent 10 years. About 80%

or more new bridge in these years belong to these two groups. The span length and skew angle ranges were also selected based on bridge inventory data statistics and consultation with members of the MDOT research advisory panel (RAP) for this project. The beam spacing range is rather more certain and was determined according to experience of the research team and the MDOT RAP members for this project. Table 5.2 lists the material properties of the steel and concrete materials used in the analysis.

Table 5.1 Analyzed bridge types and design parameters using FEA

	Steel I-beam	*Prestressed I-beam*
Skew angle	0°, 30°, 50°	0°, 30°, 50°
Beam spacing	6', 10'	6'
Span length	120', 180'	60', 120'

Table 5.2 Material properties of steel and concrete for analyzed bridge sample

	Young's modulus (ksi)	*Poisson's ratio*
Steel	29000	0.3
Concrete	3600	0.2

Using the selected design parameters, a total of 18 spans were designed according to the AASHTO LRFD Bridge Design Specifications (2007) as currently practiced in Michigan. The

resulting cross sectional details of these spans are tabulated in Tables 5.3 and 5.4. For each and every case here, the reinforced concrete deck's thickness is 9 in to be consistent with MDOT practice.

Table 5.3 Cross sections of analyzed steel bridge spans

Span-spacing-skew	top flange width	top flange thickness	web depth	web thickness	bottom flange width	bottom flange thickness
120'-6'-0°	17"	0.875"	60"	0.5625"	20"	0.875"
120'-6'-30°	17"	0.875"	60"	0.5625"	20"	0.875"
120'-6'-50°	17"	0.875"	56"	0.5625"	20"	0.875"
180'-6'-0°	17"	0.875"	84"	0.5625"	24"	1.25"
180'-6'-30°	17"	0.875"	84"	0.5625"	24"	1.25"
180'-6'-50°	17"	0.875"	81"	0.5625"	24"	1.25"
120'-10'-0°	17"	0.875"	72"	0.5625"	20"	0.875"
120'-10'-30°	17"	0.875"	72"	0.5625"	20"	0.875"
120'-10'-50°	17"	0.875"	69"	0.5625"	20"	0.875"
180'-10'-0°	17"	0.875"	84"	0.5625"	30"	1.25"
180'-10'-30°	17"	0.875"	84"	0.5625"	30"	1.25"
180'-10'-50°	17"	0.875"	80"	0.5625"	30"	1.25"

Table 5.4 Cross sections of analyzed prestressed I-beam bridge spans

Span-spacing-skew	Girder type
60'-6'-0°	AASHTO Type III girders
60'-6'-30°	
60'-6'-50°	
120'-6'-0°	AASHTO Type V girders
120'-6'-30°	
120'-6'-50°	

In order to investigate the effect of intermediate diaphragms on the behavior of the bridges, these structures with and without intermediate diaphragms were analyzed and are compared below. Figures 5.1 to 5.18 display the arrangement of the intermediate diaphragms in the analyzed bridges with different design parameters listed in Table 5.1.

Figure 5.1 Intermediate diaphragm arrangement of steel bridge:

span length = 120 ft, beam spacing = 6 ft, skew angle = 0°
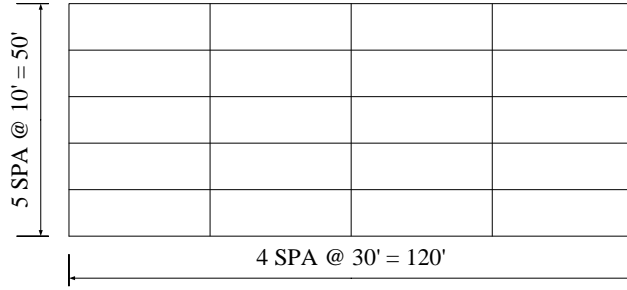
Figure 5.2 Intermediate diaphragm arrangement of steel bridge:

span length = 120 ft, beam spacing = 10 ft, skew angle = 0°
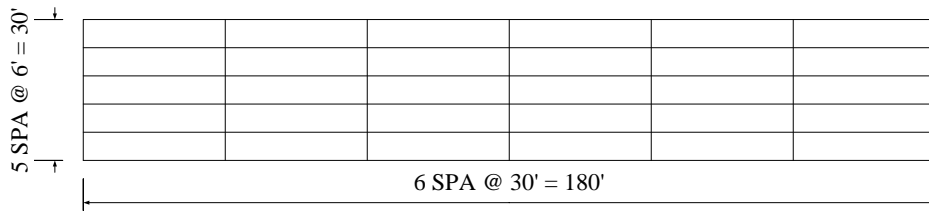
Figure 5.3 Intermediate diaphragm arrangement of steel bridge:

span length = 180', beam spacing = 6', skew angle = 0°
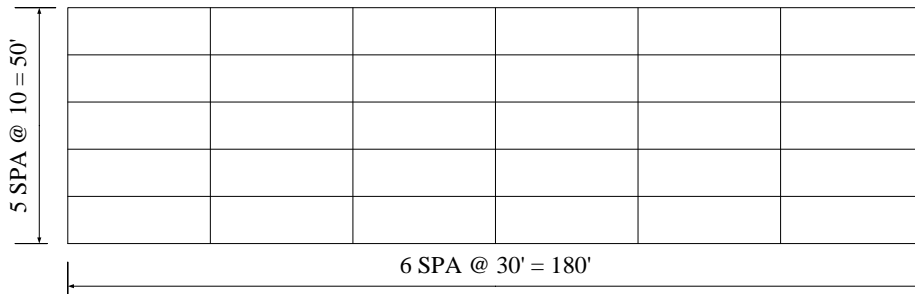
Figure 5.4 Intermediate diaphragm arrangement of steel bridge:

span length = 180', beam spacing = 10', skew angle = 0°
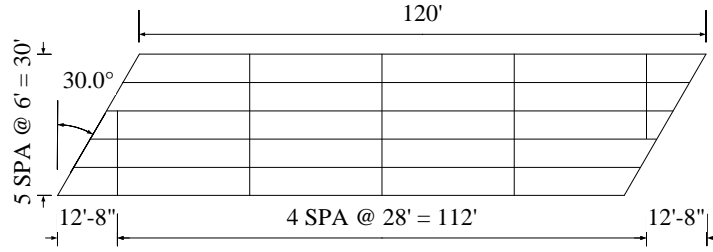
Figure 5.5 Intermediate diaphragm arrangement of steel bridge:

span length = 120 ft, beam spacing = 6 ft, skew angle = 30°
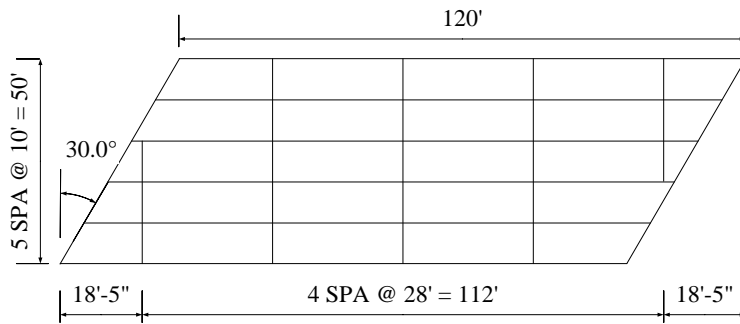
Figure 5.6 Intermediate diaphragm arrangement of steel bridge:

span length = 120 ft, beam spacing = 10 ft, skew angle = 30°
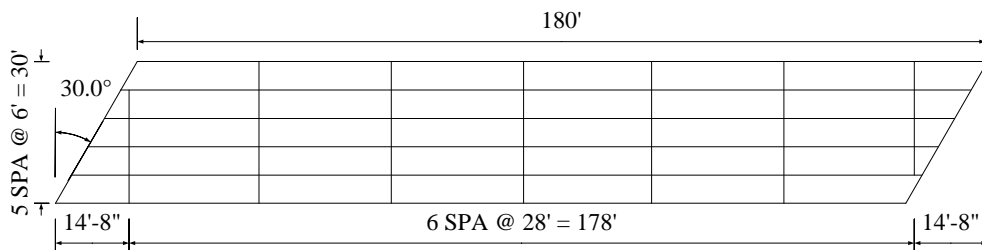
Figure 5.7 Intermediate diaphragm arrangement of steel bridge:

span length = 180 ft, beam spacing = 6 ft, skew angle = 30°
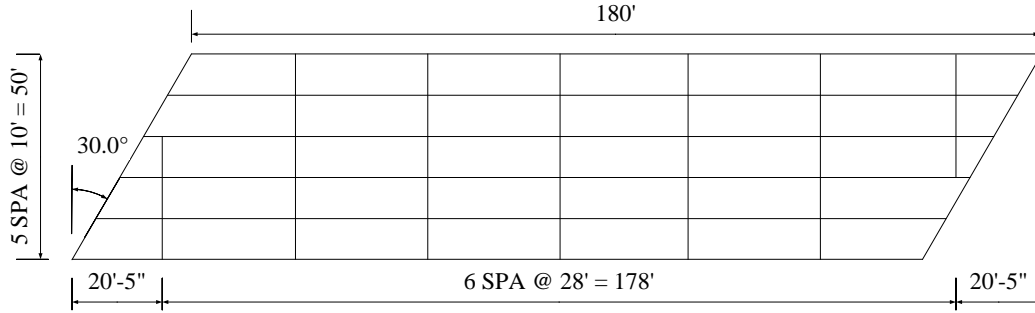
Figure 5.8 Intermediate diaphragm arrangement of steel bridge:

span length = 180 ft, beam spacing = 10 ft, skew angle = 30°
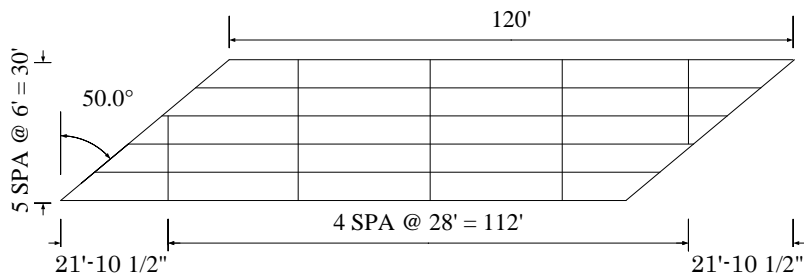
Figure 5.9 Intermediate diaphragm arrangement of steel bridge:

span length = 120 ft, beam spacing = 6 ft, skew angle = 50°
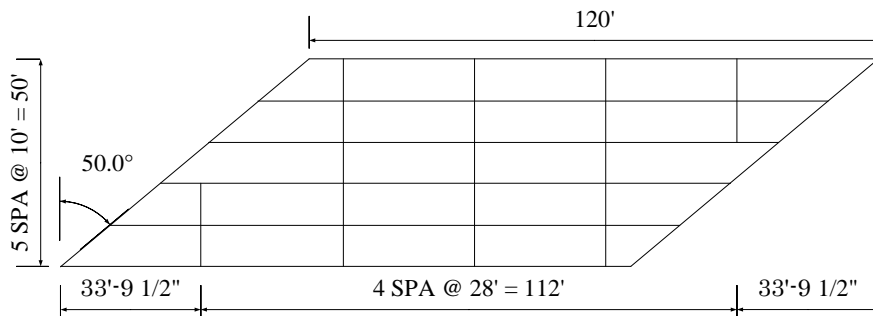
Figure 5.10 Intermediate diaphragm arrangement of steel bridge:

span length = 120 ft, beam spacing = 10 ft, skew angle = 50°

83
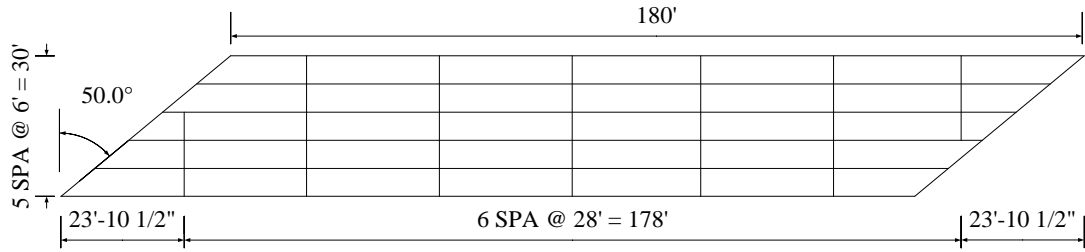
Figure 5.11 Intermediate diaphragm arrangement of steel bridge:

span length = 180 ft, beam spacing = 6 ft, skew angle = 50°
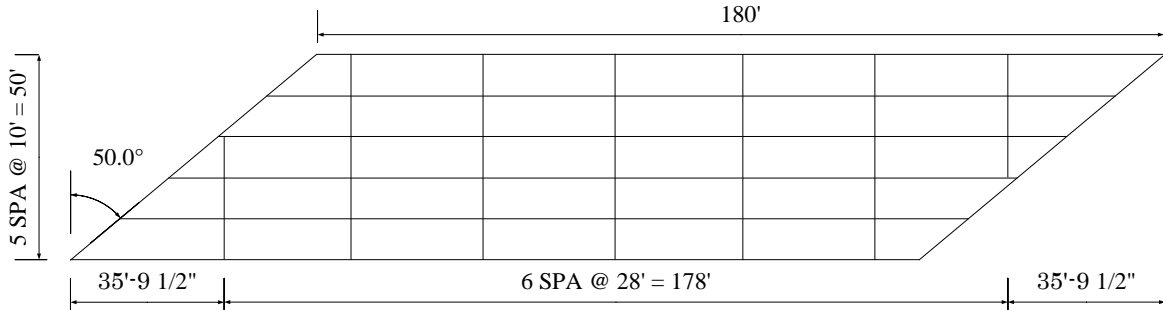
Figure 5.12 Intermediate diaphragm arrangement of steel bridge:

span length = 180 ft, beam spacing = 10 ft, skew angle = 50°
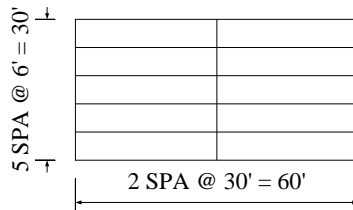
Figure 5.13 Intermediate diaphragm arrangement of prestressed concrete bridge:

span length = 60 ft, beam spacing = 6 ft, skew angle = 0°
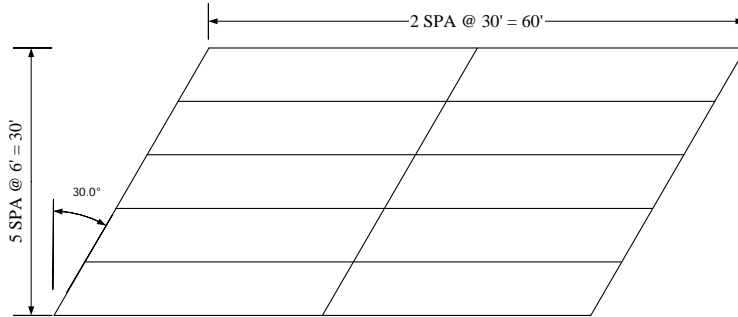
Figure 5.14 Intermediate diaphragm arrangement of prestressed concrete bridge:

span length = 60 ft, beam spacing = 6 ft, skew angle = 30°
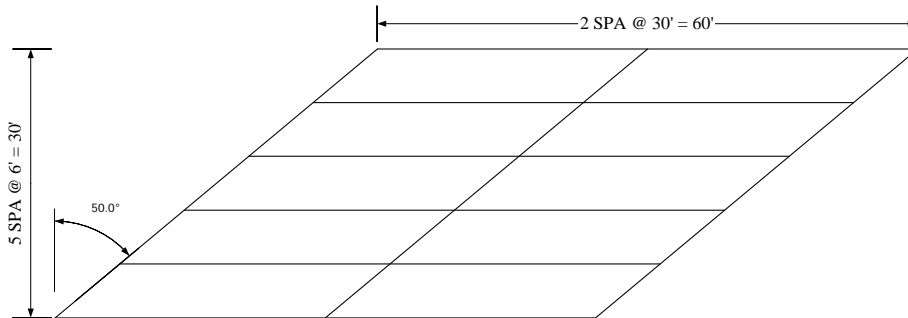
Figure 5.15 Intermediate diaphragm arrangement of prestressed concrete bridge:

span length = 60 ft, beam spacing = 6 ft, skew angle = 50°
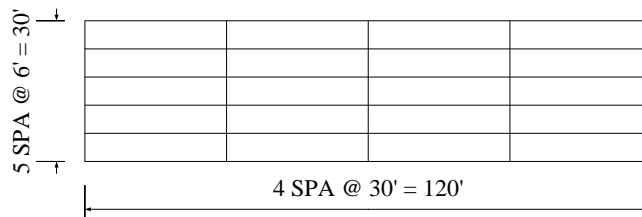
Figure 5.16 Intermediate diaphragm arrangement of prestressed concrete bridge:

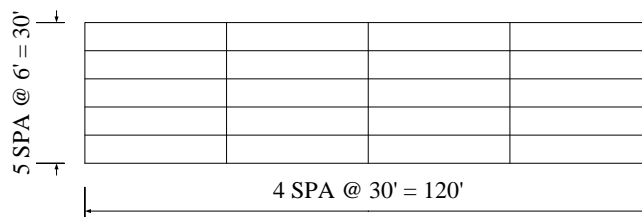span length = 120 ft, beam spacing = 6 ft, skew angle = 0°
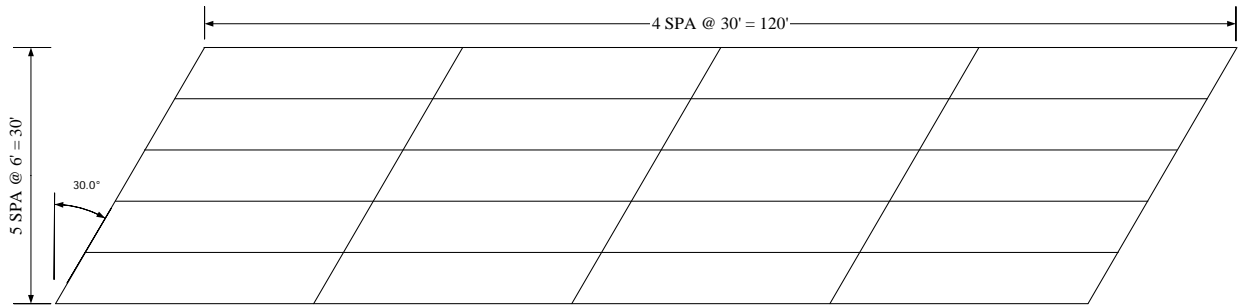
Figure 5.17 Intermediate diaphragm arrangement of prestressed concrete bridge:

span length = 120 ft, beam spacing = 6 ft, skew angle = 30°
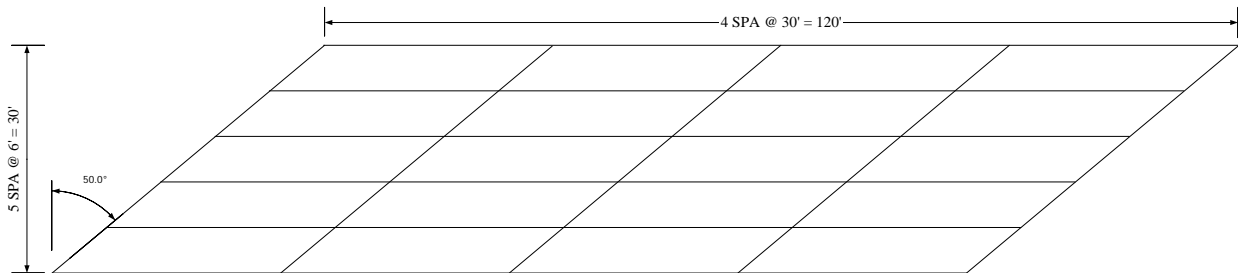
Figure 5.18 Intermediate diaphragm arrangement of prestressed concrete bridge:

span length = 120 ft, beam spacing = 6 ft, skew angle = 50°

In addition to the intermediate diaphragm, the effect of end diaphragm and bearings on the behavior of the skewed bridges were also studied. For this purpose, the following three models were analyzed.

1. The girders and deck are assumed to have a fixed support boundary condition by concrete end diaphragms at both ends of the span, like the case of Woodruff Bridge. At the bottom of the end diaphragms, translations and rotations are constrained. This condition is referred to as "Fixed" end condition hereafter.

2. The girders are assumed to be braced using typical steel cross frames. At the bottom of the girders, a simply supported condition was modeled using no constraint to horizontal translations at one end of the span and a hinge at the other end that constrains translations. This condition is referred to as "SS" end in this report.

3. The girders are assumed to be braced with typical steel cross frames. At the bottom of the girders, elastomeric bearings are provided. The bearings are modeled using solid elements and as fixed to the abutment at the bottom surface. The elastomeric bearings are modeled as a linearly elastic material with Young's modulus = 11 ksi and Poisson's Ratio = 0.4. This support condition is referred to as "bearing" end hereafter.

To focus on the parameters described above, the barriers, guard rails, or sidewalks were ignored in the FEA models.

5.2 Live load effect

In this section, a study is conducted focusing on the load distribution factors for moment and shear for the analyzed bridge spans typical in Michigan. These distribution factors are compared with those according to the AASHTO LRFD Bridge Design Specifications (2007).

5.2.1 Live load distribution factor for moment

In the AASHTO LRFD Bridge Design Specifications (2007), the load distribution factor for moment for interior beams is given in Article 4.6.2.2, as copied here in Equation 5.1. For the bridges analyzed here, it is employed to be compared with FEA results.

$$DF_m = 0.075 + \left(\frac{S}{9.5}\right)^{0.6} \left(\frac{S}{L}\right)^{0.2} \left(\frac{K_g}{12.0\,L\,t_s{}^3}\right)^{0.1} \quad ....(5.1)$$

where DF_m stands for load distribution factor for moment, S is the beam spacing (ft), L is the span length (ft), t_s is concrete slab thickness (in), K_g is the longitudinal stiffness parameter (in^4). The applicable ranges of Equation 5.1 are $3.5 \leq S \leq 16.0$, $4.5 \leq t_s \leq 12.0$, $20 \leq L \leq 240$, $4 \leq N_b$, and $10{,}000 \leq K_g \leq 7{,}000{,}000$. The analyzed bridge spans in this research project fall in these ranges.
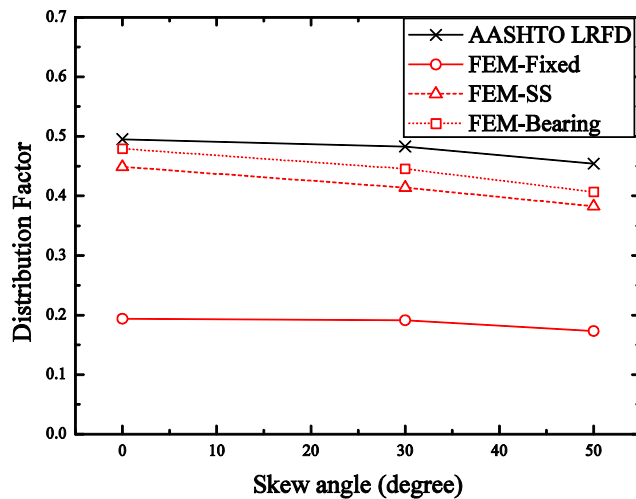
Figure 5.19 Load distribution factor for moment in interior beams of steel bridge:

span length = 120 ft, beam spacing = 6 ft.

For skewed bridges, the following correction factor is also required in the AASHTO specifications to be multiplied to the load distribution factor in Equation 5.1 to account for skew and effectively reduce the design bending moment.

$$1 - 0.25 \left(\frac{K_g}{12.0 \, L \, t_s^3} \right)^{0.25} \left(\frac{S}{L} \right)^{0.5} (\tan \theta)^{1.5} \quad \ldots\ldots\ldots\ldots\ldots\ldots\ldots\ldots\ldots(5.2)$$

where θ is the skew angle in degree. The applicable range of above equation is $30° \le \theta \le 60°$, $3.5 \le S \le 16.0$, $20 \le L \le 240$, and $4 \le N_b$. The analyzed bridges have skew angles within the given applicability range. Results calculated using these specified equations are to be compared with the FEA results.
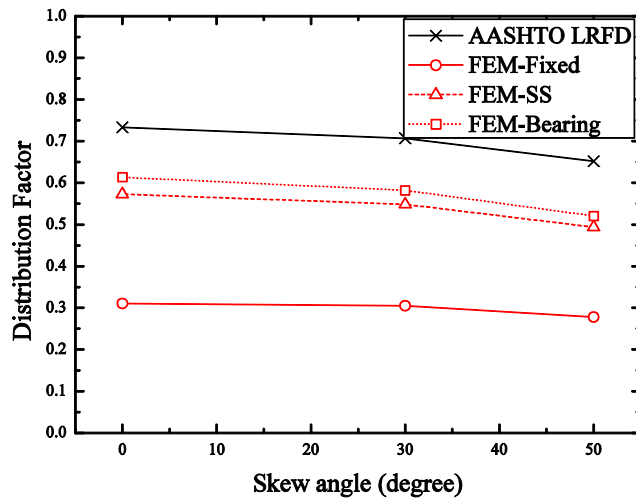
Figure 5.20 Load distribution factor for moment in interior beams of steel bridge: span length = 120 ft, beam spacing = 10 ft.

Figures 5.19 to 5.24 for respective design parameter combinations display the FEA results of moment distribution factors of the analyzed bridge spans, compared with the AASHTO distribution factors also plotted. It is seen that the "Fixed" end model significantly deviates from the other models and the AASHTO approach. Otherwise, the other two models ("SS" and "Bearing") are closer to the AASHTO approach. When the beam spacing is smaller (6 ft), the AASHTO approach gives fairly similar results of moment distribution. While the AASHTO distribution factor is generally acceptable compared with the FEA results, it is also fair to point out that the former generally overestimates moment effect, with a maximum of about 25% overestimation.
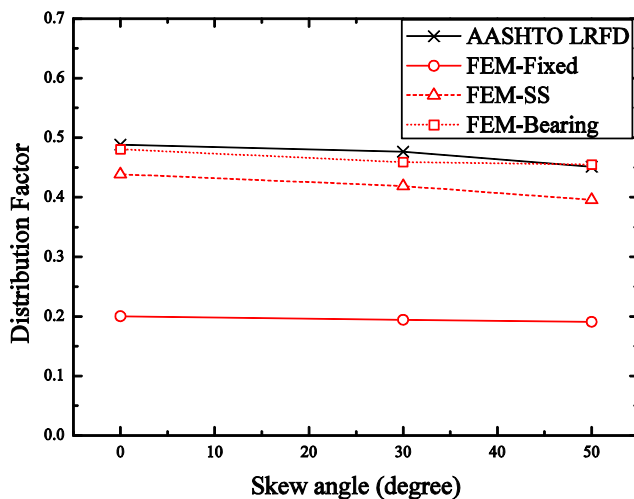
Figure 5.21 Load distribution factor for moment in interior beams of steel bridge:

span length = 180 ft, beam spacing = 6 ft.
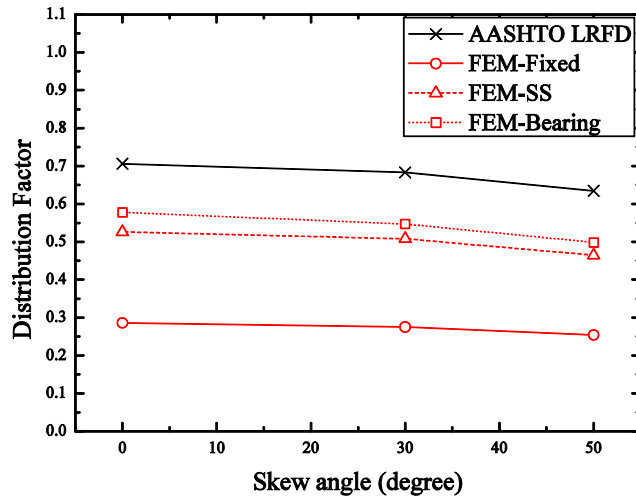
Figure 5.22 Load distribution factor for moment in interior beams of steel bridge:

span length = 180 ft, beam spacing = 10 ft.
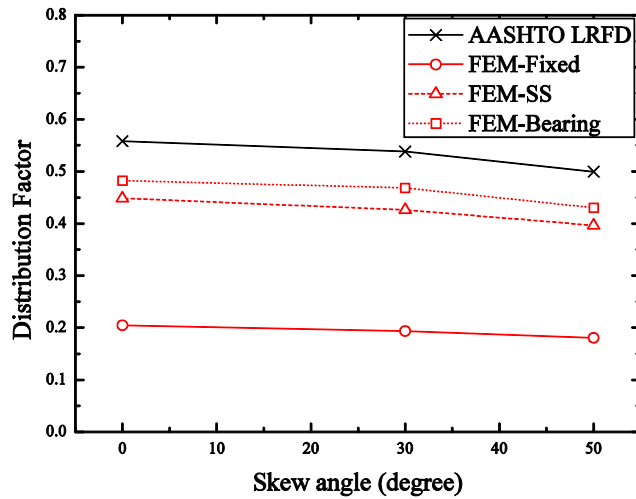
Figure 5.23 Load distribution factor for moment in interior beams of prestressed concrete bridge:

span length = 60 ft, beam spacing = 6 ft.
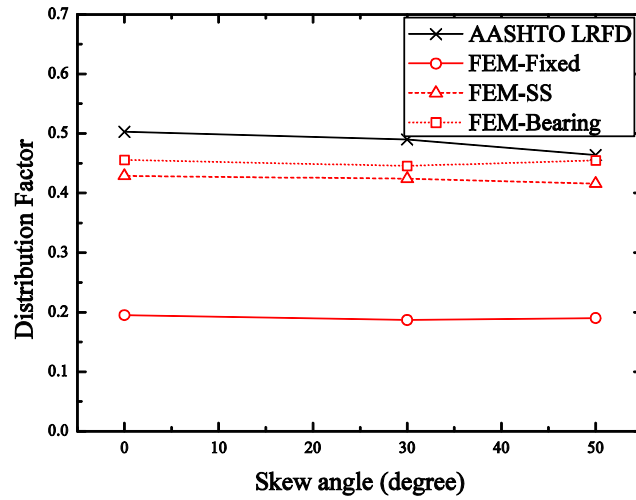
Figure 5.24 Load distribution factor for moment in interior beams of prestressed concrete bridge: span length = 120 ft, beam spacing = 6 ft.

Influence of intermediate diaphragms

To understand the effect of intermediate diaphragms considered to be a possible reason for the observed difference in the moment distribution factor, models with and without the intermediate diaphragms are used in FEA for comparison. The results are shown in Figures 5.25 to 5.30 according to the combination of design parameters, span type, span length, beam spacing, and skew angle.
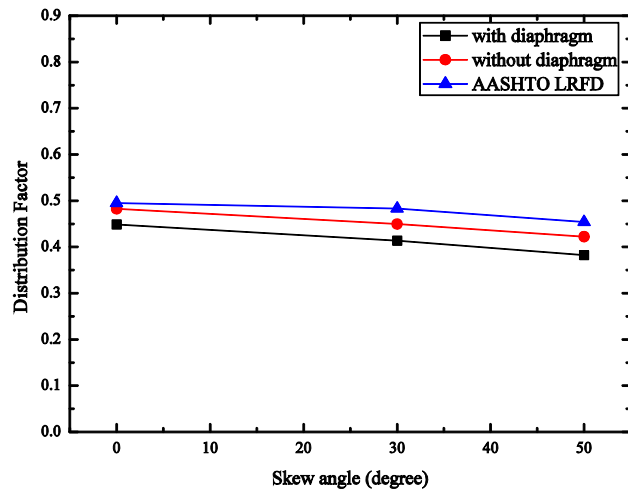
Figure 5.25 Effect of intermediate diaphragms on moment distribution factor in interior beams:

steel bridge, span length = 120 ft, beam spacing = 6 ft
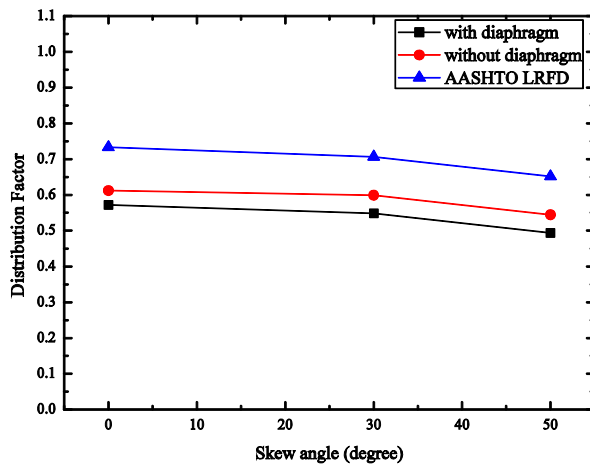
Figure 5.26 Effect of intermediate diaphragms on moment distribution factor in interior beams:

steel bridge, span length = 120 ft, beam spacing = 10 ft
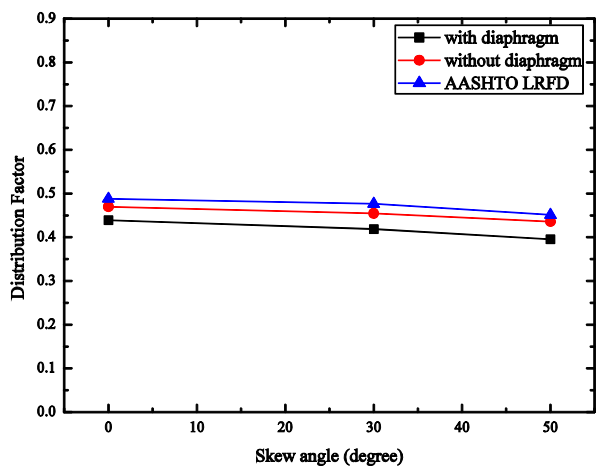
Figure 5.27 Effect of intermediate diaphragms on moment distribution factor in interior beams:

steel bridge, span length = 180 ft, beam spacing = 6 ft
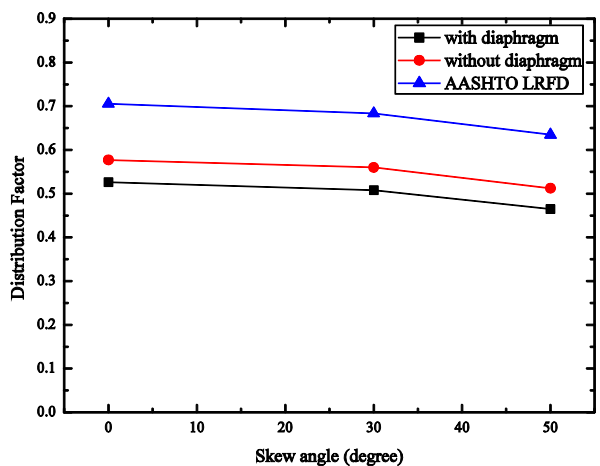
Figure 5.28 Effect of intermediate diaphragms on moment distribution factor in interior beams:

steel bridge, span length = 180 ft, beam spacing = 10 ft
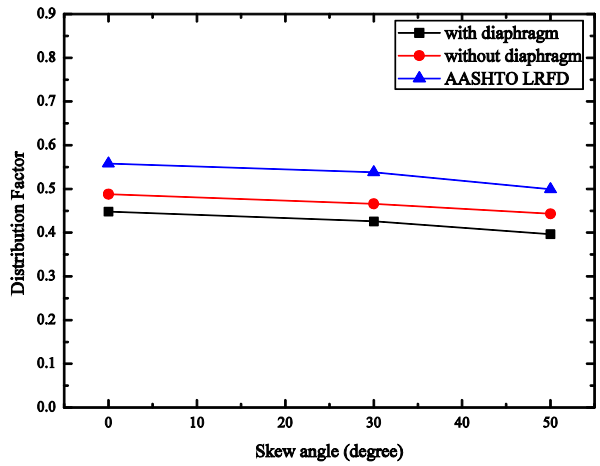
Figure 5.29 Effect of intermediate diaphragms on moment distribution factor in interior beams:

prestressed concrete bridge, span length = 60 ft, beam spacing = 6 ft
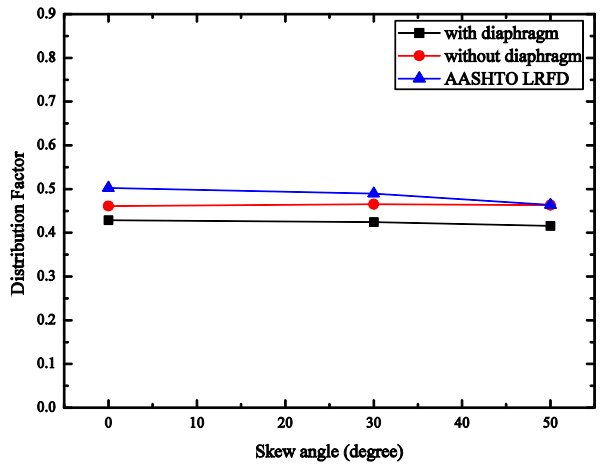
Figure 5.30 Effect of intermediate diaphragms on moment distribution factor in interior beams:

prestressed concrete bridge, span length = 120 ft, beam spacing = 6 ft

It is seen in these results that the intermediate diaphragms do reduce the moment

noticeably but at most about 10%. It is also of interest to mention that the AASHTO moment

distribution factor indeed overestimates the moment effect even further beyond the models with intermediate diaphragms. Again, the 10 ft beam spacing cases appear to show more noticeable differences than 6 ft. This perhaps is because of the relatively stiffer diaphragms used and the AASHTO distribution factors do not include diaphragm stiffness as an influencing factor.

Influence of warping

Warping effect may become significant in thin-walled open section beams subjected to twisting moment for skewed or horizontally curved cross sections. Beam bridges' cross sections may be viewed as an assembly of a number of π shaped thin walled open sections with a beam being a leg of the π shape cross section. This phenomenon causes additional longitudinal stresses in the bottom flange of the beams. In order to examine the effect of warping, the FEA results were examined at the quarter and mid span cross sections. The midspan section was expected to experience the maximum bending stress and the quarter span section the maximum warping stress. The warping stresses are compared with the bending stresses in Figures 5.31 and 5.32 as a ratio to help observe the warping effect for all 18 cases of design parameter combinations listed in Table 5.1.
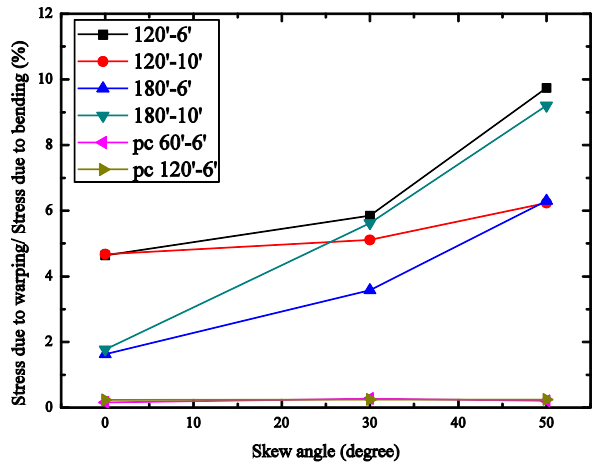
Figure 5.31 Effect of warping at quarter span section
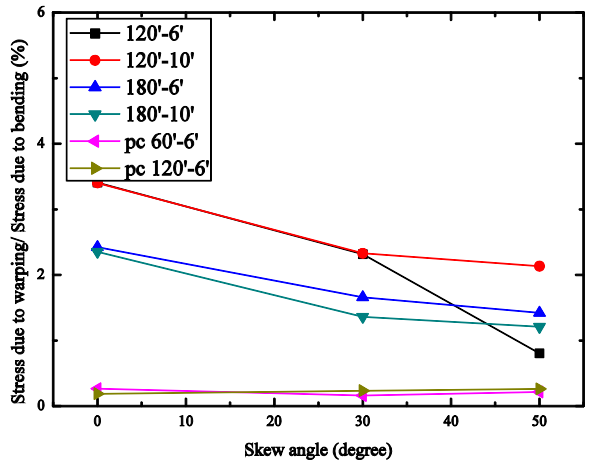
Figure 5.32 Effect of warping at mid span section

These curves show the ratio of the warping stress to bending stress as a function of skew angle for the range defined in Table 5.1. It is seen there that the warping effect is very small or negligible for the prestressed concrete bridges. This is because warping effect exists only in thin-walled open sections, and the prestressed I-beam sections are hardly considered to be of

thin-wall with also the deck included in the cross section. For steel bridges, warping effect is rather more visible but still too small to be worth attention in routine design such as those cases investigated herein.

The warping stress is observed at about 3% of the bending stress at the mid span section (Figure 3.32). In contrast at the quarter span where warping effect was expected to reach its maximum, the warping effect increases as the skew angle increases and the stress ratio can reach up to about 10% (Figure 3.31). Note also that at the quarter span location, the bending moment or stress is lower than that at the midspan section. Thus, the total longitudinal stress at the quarter span is expected to be still smaller than that at midspan. Nevertheless, if the beam is designed to change cross section (*e.g.,* for a plate girder), it is prudent and thus recommended to locate the cross section reduction beyond the point where warping effect may become significant, which is the quarter span point for these cases analyzed here.

5.2.2 Load distribution factor for shear

In the AASHTO LRFD Bridge design Specification (2007), the load distribution factor for shear is given in Article 4.6.2.2. In this section, the main focus is on the shear in the exterior beam, also referred to as the obtuse corner shear or reaction where a maximum is expected. For this case, the AASHTO shear distribution factor is copied here:

$$DF_s = \left(0.6 + \frac{d_g}{10}\right)\left(0.2 + \frac{S}{12} - \left(\frac{S}{35}\right)^2\right) \dots\dots\dots\dots\dots\dots\dots\dots(5.3)$$

where DF_s is the load distribution factor for shear, d_e is the distance from the exterior web of the exterior beam to the interior edge of curb or traffic barrier in feet. The applicable ranges of Equation 5.3 are $3.5 \le S \le 16.0$, $4.5 \le t_s \le 12.0$, $20 \le L \le 240$, $4 \le N_b$, $-1.0 \le d_e \le 6.6$. All the analyzed bridge spans in this report are within these ranges. To account for skew effect, the following correction factor is prescribed in the AASHTO specifications to be multiplied to the load distribution factor for support shear at the obtuse corner.

$$1 + 0.20 \left(\frac{12.0\,L\,t_s^{\,3}}{K_g} \right)^{0.3} \tan\theta \quad\text{...(5.4)}$$

The applicable ranges of Equation 5.4 are $0° \le \theta \le 60°$, $3.5 \le S \le 16.0$, $20 \le L \le 240$, and $4 \le N_b$. The considered cases in this report defined in Table 5.1 are all within these ranges. Their FEA results are exhibited in Figures 5.33 to 5.38 along with those using the AASHTO approach for comparison.
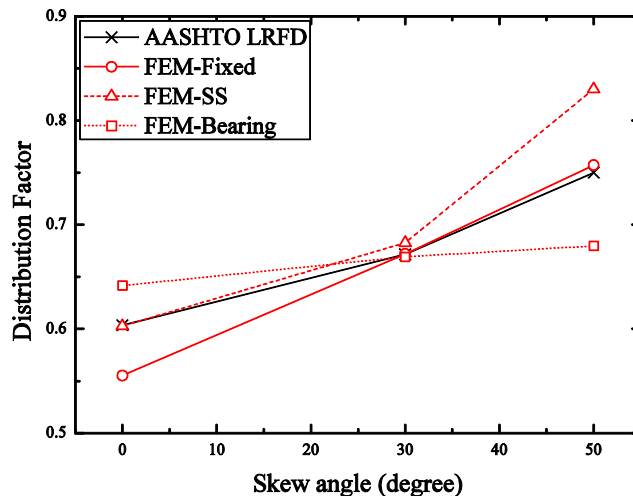
Figure 5.33 Load distribution factor for shear in exterior beams of steel bridge:

99

span length = 120 ft, beam spacing = 6 ft
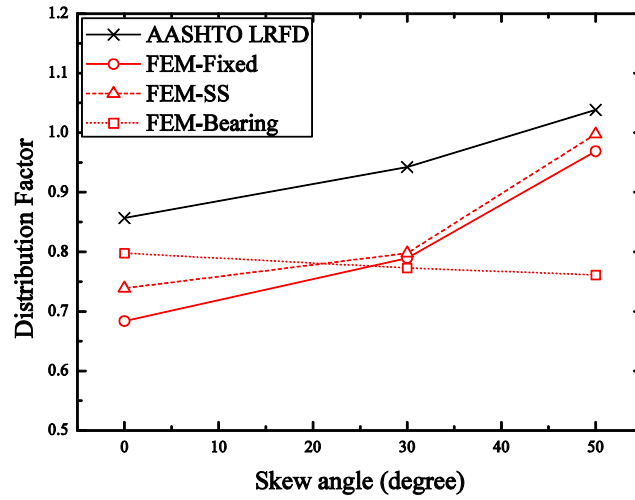
Figure 5.34 Load distribution factor for shear in exterior beams of steel bridge:

span length = 120 ft, beam spacing = 10 ft
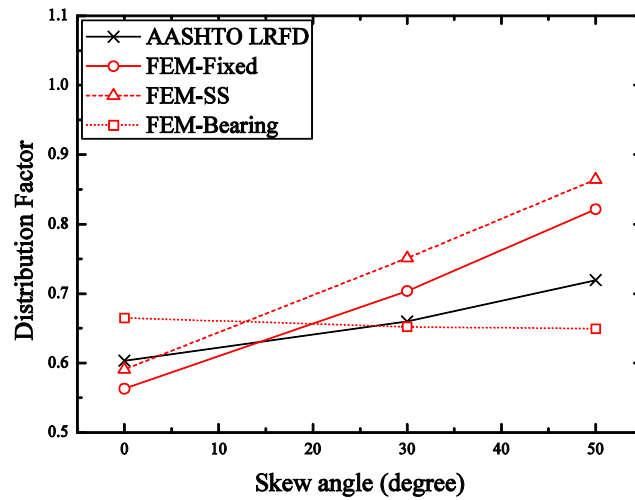
Figure 5.35 Load distribution factor for shear in exterior beams of steel bridge:

span length = 180 ft, beam spacing = 6 ft
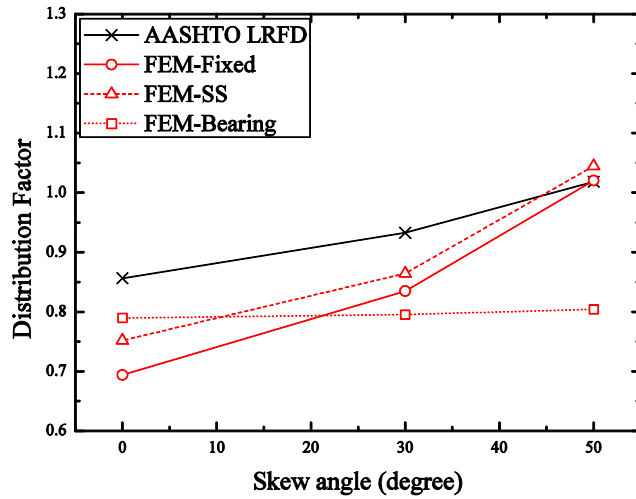
Figure 5.36 Load distribution factor for shear in exterior beams of steel bridge:

span length = 180 ft, beam spacing = 10 ft
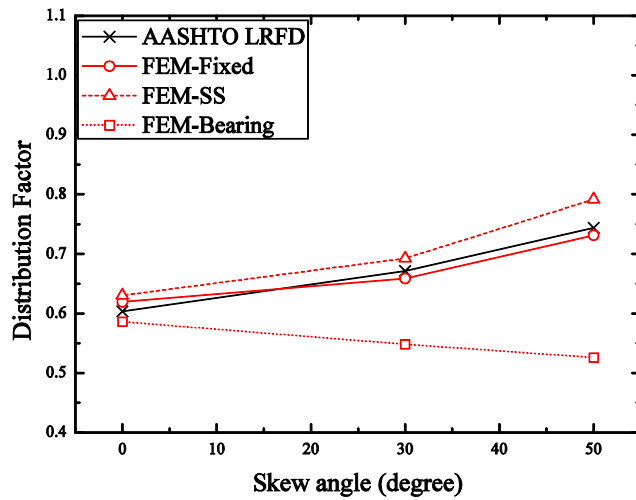
Figure 5.37 Load distribution factor for shear in exterior beams of prestressed concrete bridge:

span length = 60 ft, beam spacing = 6 ft
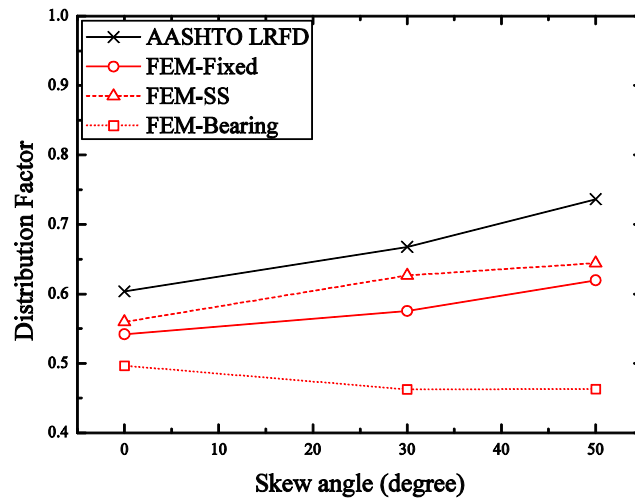
Figure 5.38 Load distribution factor for shear in exterior beams of prestressed concrete bridge:

span length = 120 ft, beam spacing = 6 ft

It is seen in these figures that the "Fixed" and "SS" end models have produced similar results as the AASHTO approach. In contrast, the "Bearing" end model's shear distribution factor is noticeably different. This model allows the supports (bearings) to deform and thus more evenly distribute the total load being transferred from the superstructure through the bearing to the substructure, while the other models and approach ("Fixed", "SS", and the AASHTO approach) do not. Figure 5.39 shows how the total load is distributed among all the beams and thus bearings as a typical case. It is seen that, compared with the SS end condition, the "bearing" end condition distributes the reactions forces more evenly. This more even distribution reduces the reaction on the bearing at the obtuse corner. In other words, the bearings next to the obtuse corner bearing share more loads than the "SS" end condition model.

While it may be too high of a requirement for design calculations to consider bearings' function of load distribution, the SS end condition that is commonly used in routine design is shown here to produce conservative predictions for design shear.
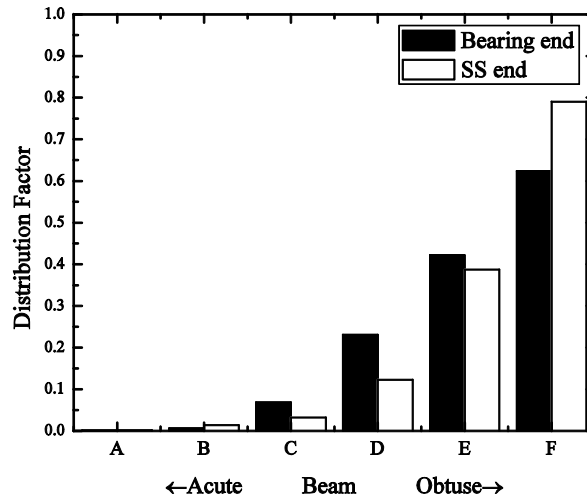
Figure 5.39 Reaction force distribution among beams

(steel bridge, span length = 120 ft, beam spacing = 10 ft, skew angle = 50°)

Influence of torsion

Skewed bridges are subjected to twisting moment due to differential deflections in the beams and different load paths from the loading location to the nearest support. This twisting adds shear stresses to the maximum shears in their straight counterpart. It is thus important to understand this effect and its magnitude for routine design. Figure 5.40 is designed to shed light on this effect. It displays the ratio of the shear stress on the fascia beam web due to torsion to that due to reaction shear as a function of the skew angle. It is seen that the torsional effect is

relatively small, especially for the steel superstructure, probably because it is less rigid than the prestressed concrete superstructure and its span is usually longer. For different locations other than the obtuse corner, more torsional effect has been observed, but the shear is much lower than that at the obtuse corner and therefore the total shear stress is lower. Thus, it is concluded that the effect of torsion causing additional shear stress is not at a significant level for skewed bridge design in Michigan to deserve special checking.
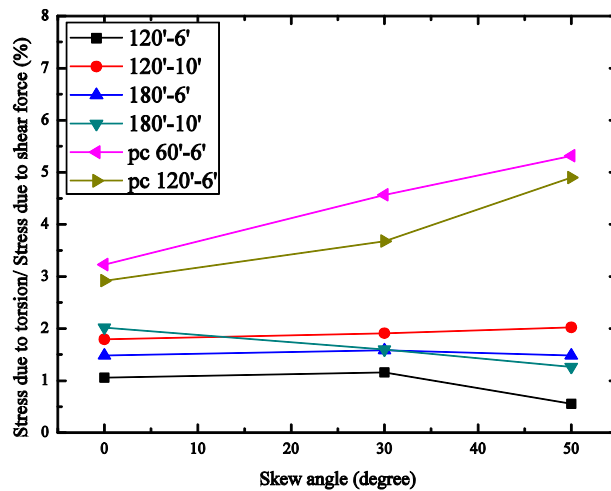
Figure 5.40 Effect of torsion on shear at obtuse corner

5.3 Thermal load effect

The effects of ambient thermal forces on bridge components can be significant and should not be underestimated or ignored in design. The thermal forces referred to here are caused by fluctuation in ambient temperature. In the AASHTO LRFD Bridge Design Specifications (2007), the prescribed change in temperature is a function of the bridge location as well as the

superstructure material. The specifications require consideration for two types of temperature change: uniform temperature change and gradient temperature change. In the following sections, both changes are discussed and addressed.

5.3.1 Uniform temperature load

The uniform temperature change refers to the condition where the entire bridge is at the same temperature without differential temperature differences in the same or different components and is then subjected to a constant temperature change. The temperature range is the difference between $T_{MaxDesign}$ and $T_{MinDesign}$, where $T_{MaxDesign}$ and $T_{MinDesign}$ are respectively the highest and lowest temperatures the bridge may experience. Figures 5.41 to 5.44 below show the highest and lowest temperatures given in the AASHTO LRFD code for steel and concrete girder bridges with a concrete deck of interest here. For Michigan, the highest and lowest temperatures are summarized in Table 5.5.
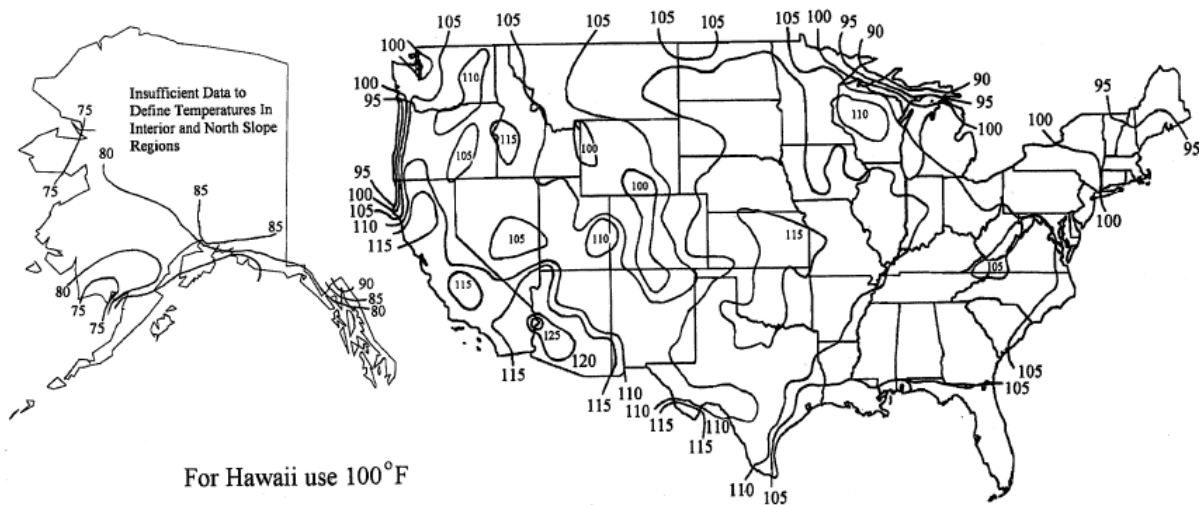
Figure 5.41 Contour map of $T_{MaxDesign}$ for concrete girder bridges with concrete deck

Note that the temperature difference focused here is understood as the cause of thermal load effects, such as thermal expansion or contraction for the entire superstructure.
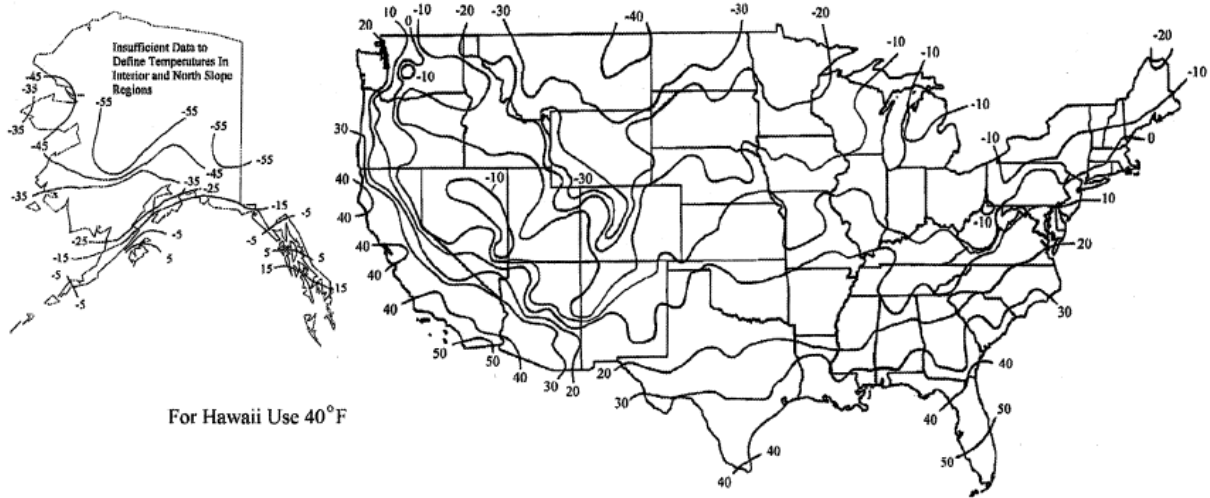
Figure 5.42 Contour map of $T_{MinDesign}$ for concrete girder bridges with concrete deck
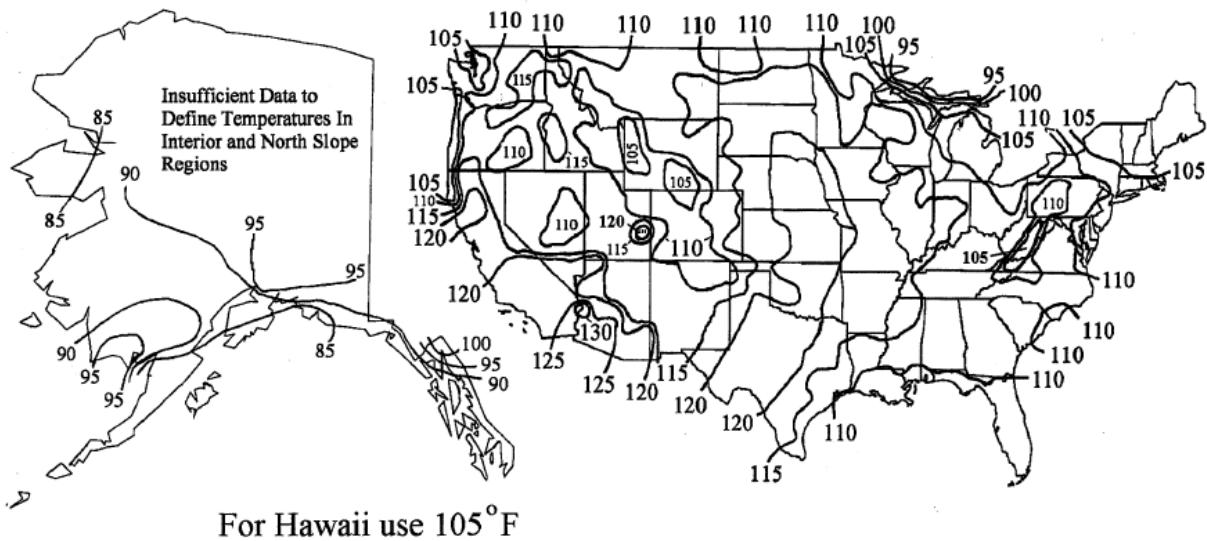
Figure 5.43 Contour map of $T_{MaxDesign}$ for steel girder bridges with concrete deck

For Hawaii use 30°F
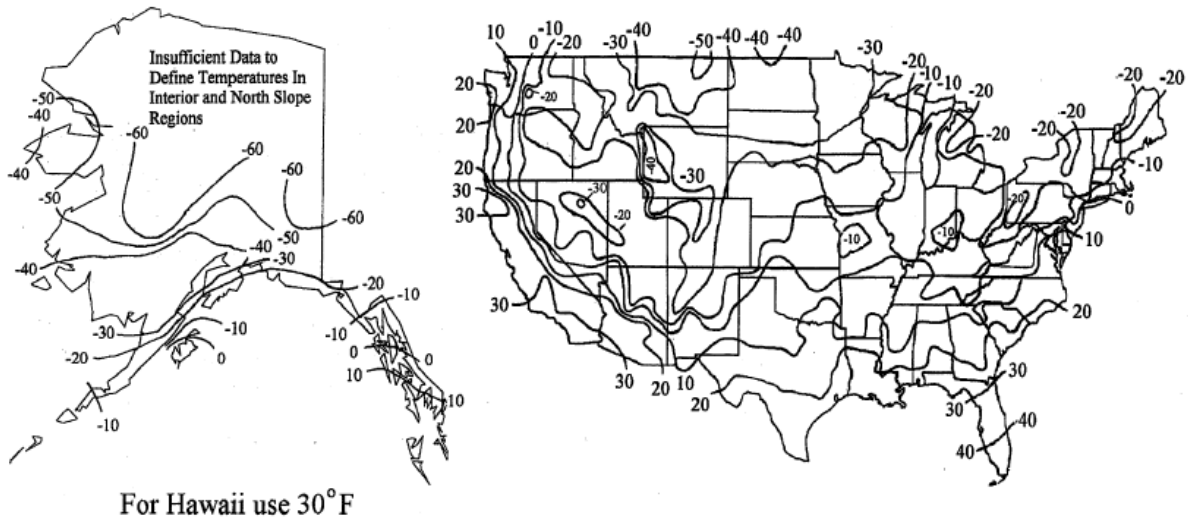
Figure 5.44 Contour map of $T_{MinDesign}$ for steel girder bridges with concrete decks

Table 5.5 $T_{MaxDesign}$ and $T_{MinDesign}$ for steel and concrete girder bridges in Michigan

	$T_{MaxDesign}$	$T_{MinDesign}$
Steel girder bridges with concrete decks	110°F	-20°F
Concrete girder bridges with concrete decks	105°F	-10°F

The design thermal movement is then computed here using the temperature range Δ_T given in the following equation and is applied to the sample of typical Michigan bridges analyzed here in.

$$\Delta_T = T_{MaxDesign} - T_{MinDesign}$$ ....(5.5)

107

5.3.2 Temperature gradient load

Contrary to uniform temperature change mainly due to seasonal change, bridge structures can also be exposed to temperature gradient over the depth of the superstructure mainly due to impedance of the structure to temperature change in a short period of time, such as in a day. For example, when the deck or top of the bridge is exposed to the sun while the bottom side is not, the differential in temperature through the depth of the superstructure can cause thermal forces. The AASHTO LRFD Bridge Design Specifications specify the vertical temperature gradient in concrete and steel superstructures with a concrete deck as shown in Figure 5.45. This model is used in analyzing the typical Michigan bridge spans here.
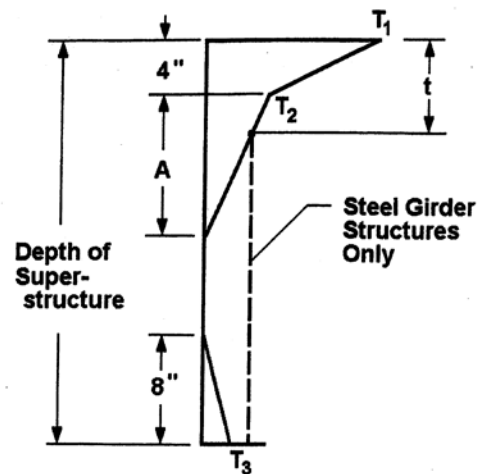
Figure 5.45 Positive vertical temperature gradient in concrete and steel superstructures

Dimension A in Figure 5.45 is taken as:

- 12.0 in., for concrete superstructures that are 16.0 in. or more in depth.

- 4.0 in. less than the actual depth, for concrete sections shallower than 16.0 in.

- 12.0 in. with distance t as the depth of the concrete deck, for steel superstructures.

Temperature T_1 and T_2 in Figure 5.45 are given in Figure 5.46 and Table 5.6 taken from the AASHTO LRFD specifications. For example, Michigan is categorized as Zone 3 in Figure 5.46, and therefore $T_1 = 41°F$ and $T_2 = 11°F$ according to Table 5.6. The specifications allow T_3 to be set at 0.0°F unless a site-specific study is made to determine a more appropriate value. In this report, $T_3 = 0.0°F$ is accordingly used.
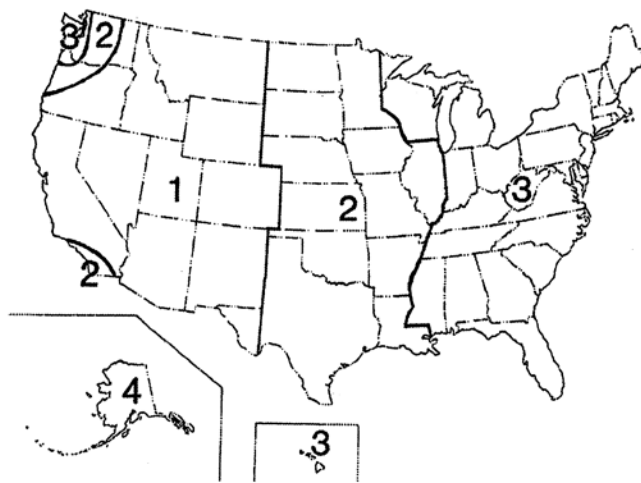
Figure 5.46 Solar radiation zones for the United States

Table 5.6 Basic parameters for temperature gradients in Figure 5.45

Zone	T_1 (°F)	T_2 (°F)
1	54	14
2	46	12
3	41	11
4	38	9

According to the AASHTO LRFD code, not only positive temperature values in the gradient model but also negative values for T_1 and T_2 should be considered. The negative values shall be obtained by multiplying -0.30 to the value specified in Table 5.6 for plain concrete decks and -0.20 for decks with an asphalt overlay. This negative temperature case can cause positive bending moment effect in the midspan area of the bridge span and therefore should be taken into account.

5.3.3 Analysis results for moment

In this section, the effect of temperature on the moment in the typical Michigan bridges is discussed. Thermal loads due to uniform temperature change and gradient temperature described in the previous sections are applied to the typical Michigan bridge models developed in this chapter. Table 5.7 shows the coefficients of thermal expansion of steel and concrete materials used in the FEA.

Table 5.7 Coefficients of thermal expansion of steel and concrete

Material	Coefficient of thermal expansion (/°F)
Steel	6.5×10^{-6}
Concrete	5.5×10^{-6}

The difference between concrete and steel shown in Table 5.7 results in a bending effect in a composite bridge cross section when thermal load is applied. In addition to this, the

difference in temperature between top and bottom of the bridge which causes moment effect is considered when gradient thermal load is applied.

Figures 5.47 to 5.55 show the contour plots of principal stress for the typical Michigan bridge span of 120 ft span length and 10 ft beam spacing subjected to the HL93 truck load, gradient temperature load, and uniform temperature load. The principal stress is mainly caused by bending moment. As seen in the figures, the location of the maximum moment by thermal effect is close to that by truck load. Therefore, the location where the maximum moment is observed under truck loads is focused on hereafter.
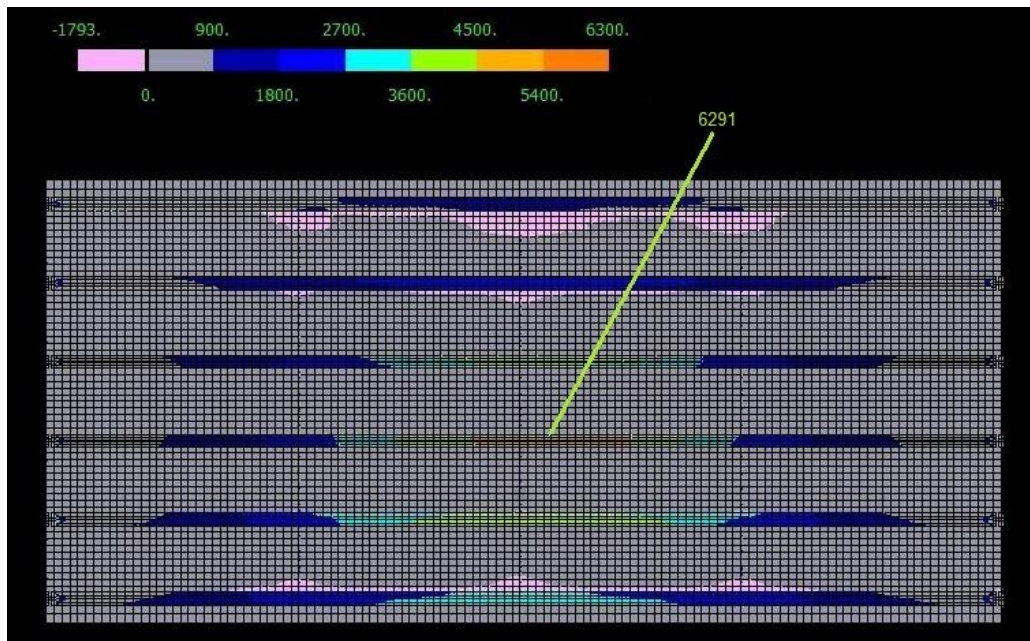
Figure 5.47 Contour plots for maximum principal stress subjected to HL93 truck load

(span length = 120 ft, steel beam spacing = 10 ft, skew angle = 0°)
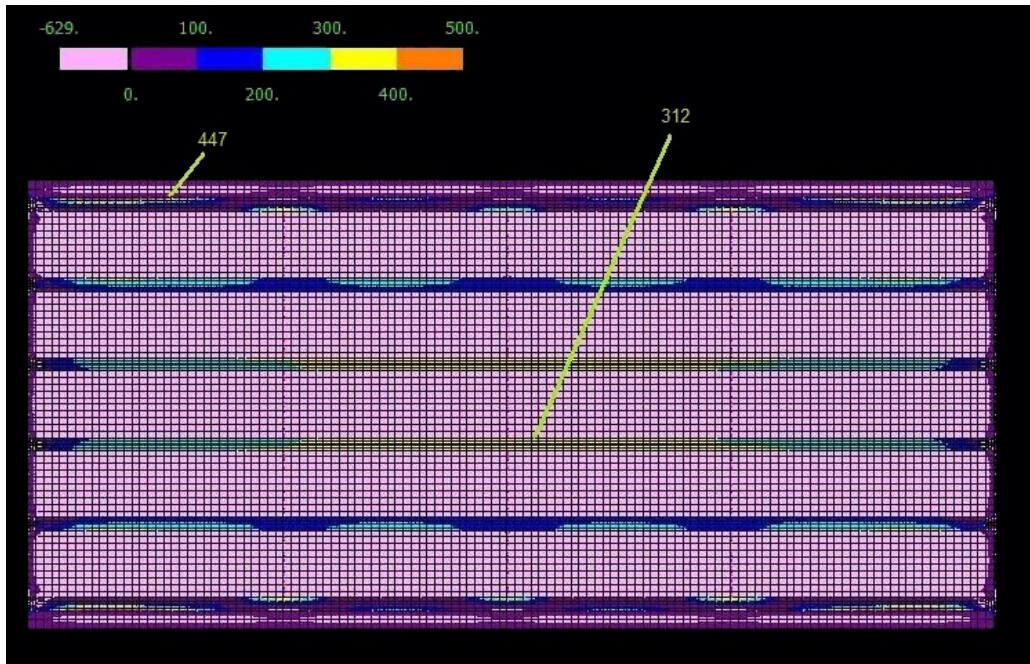
Figure 5.48 Contour plots for maximum principal stress subjected to gradient temperature load

(span length = 120 ft, steel beam spacing = 10 ft, skew angle = 0°)
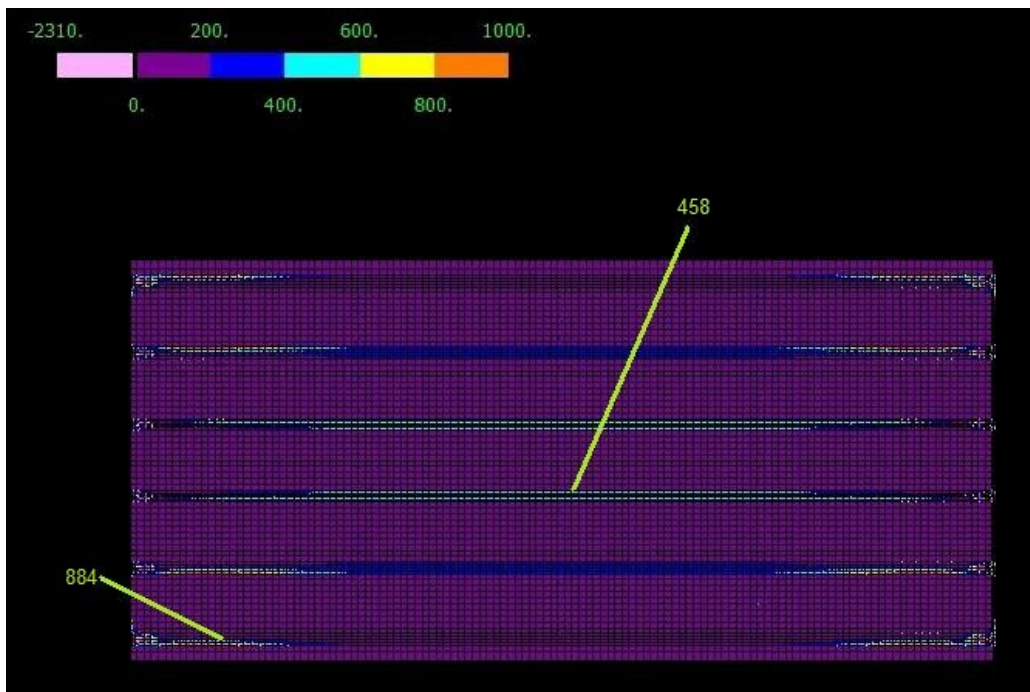
Figure 5.49 Contour plots for maximum principal stress subjected to uniform temperature load

(span length = 120 ft, steel beam spacing = 10 ft, skew angle = 0°)
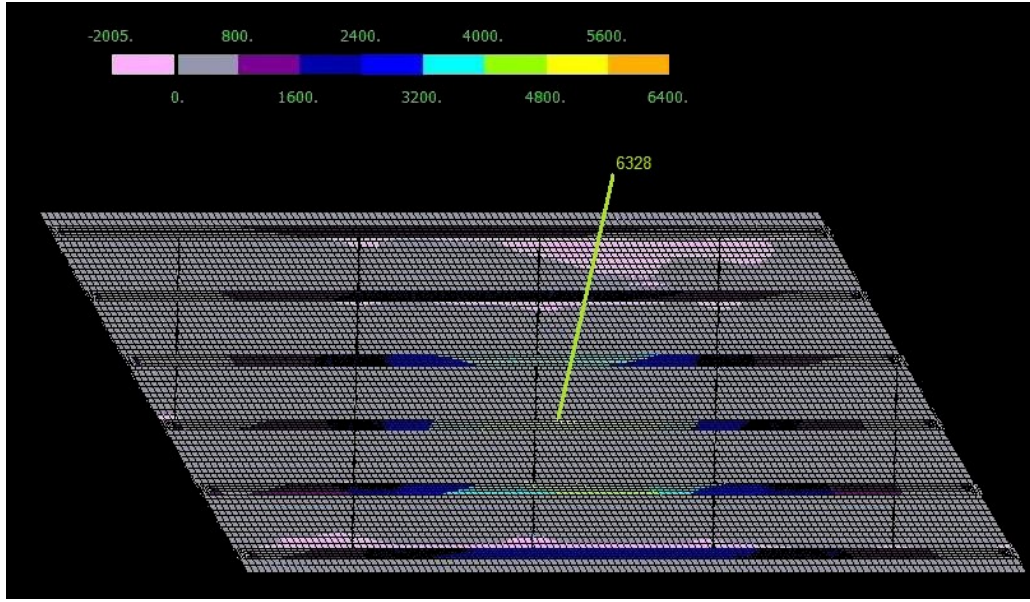
Figure 5.50 Contour plots for maximum principal stress subjected to HL93 truck load

(span length = 120 ft, steel beam spacing = 10 ft, skew angle = 30°)
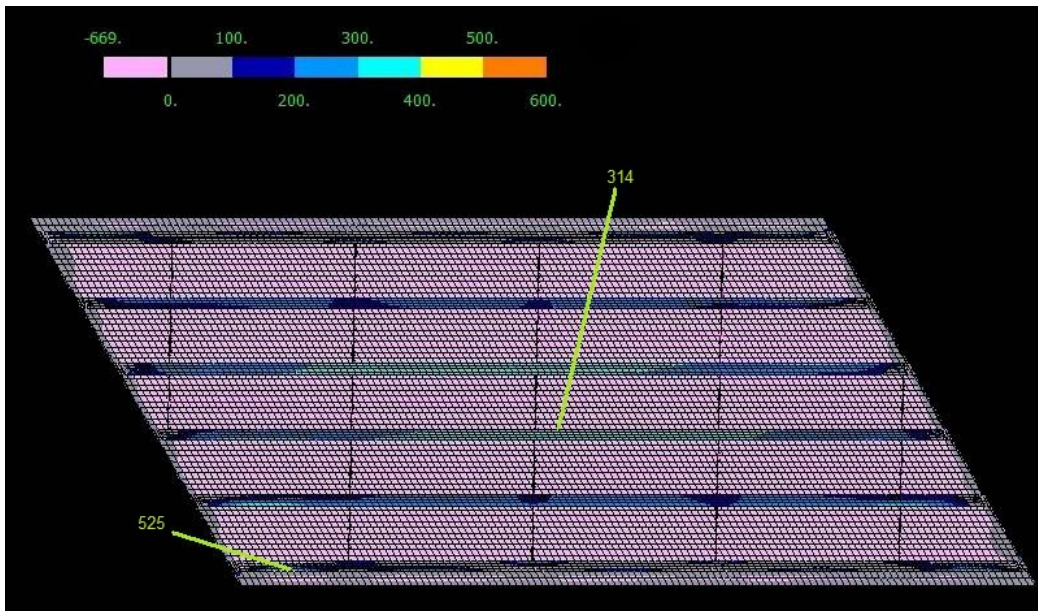
Figure 5.51 Contour plots for maximum principal stress subjected to gradient temperature load

(span length = 120 ft, steel beam spacing = 10 ft, skew angle = 30°)
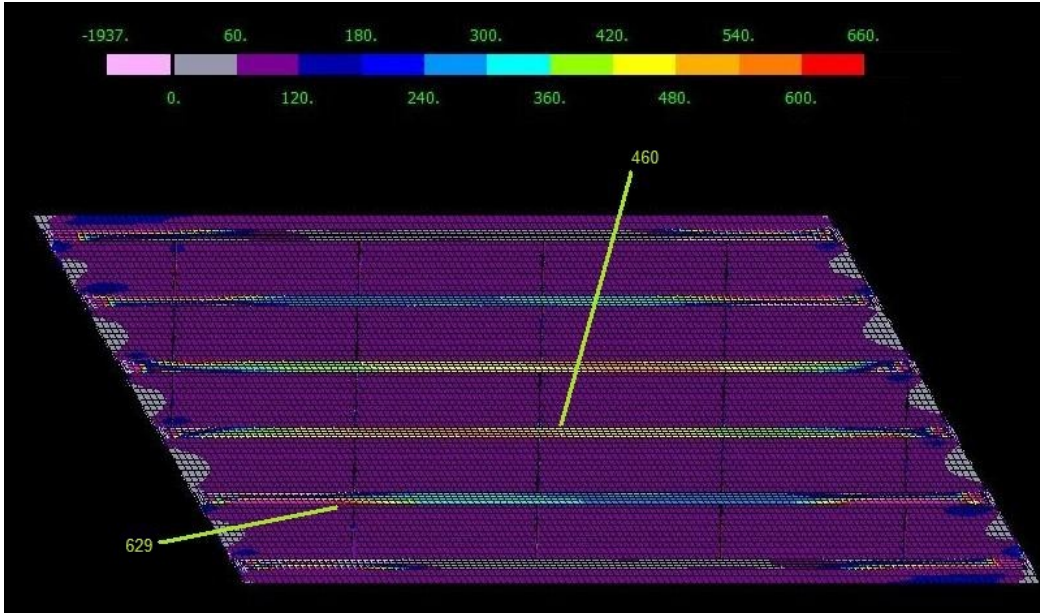
Figure 5.52 Contour plots for maximum principal stress subjected to uniform temperature load

(span length = 120 ft, steel beam spacing = 10 ft, skew angle = 30°)
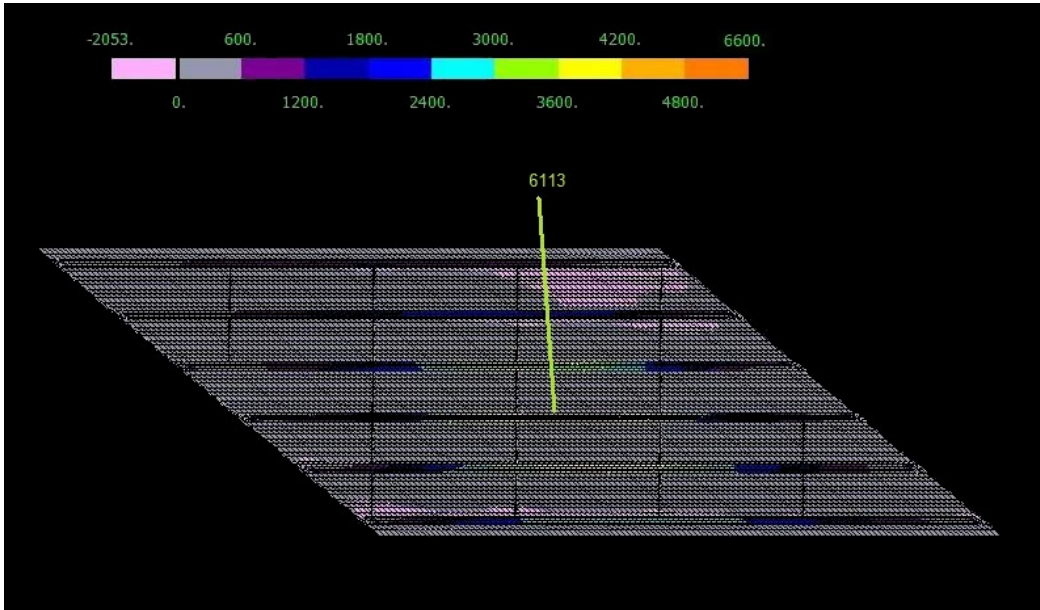
Figure 5.53 Contour plots for maximum principal stress subjected to HL93 truck load

(span length = 120 ft, steel beam spacing = 10 ft, skew angle = 50°)
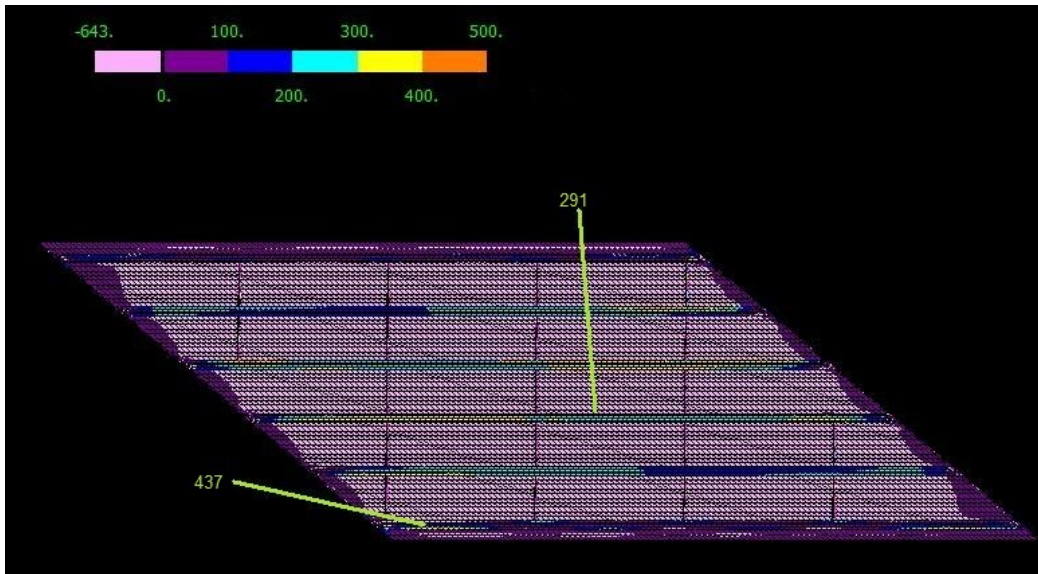
Figure 5.54 Contour plots for maximum principal stress subjected to gradient temperature load

(span length = 120 ft, steel beam spacing = 10 ft, skew angle = 50°)
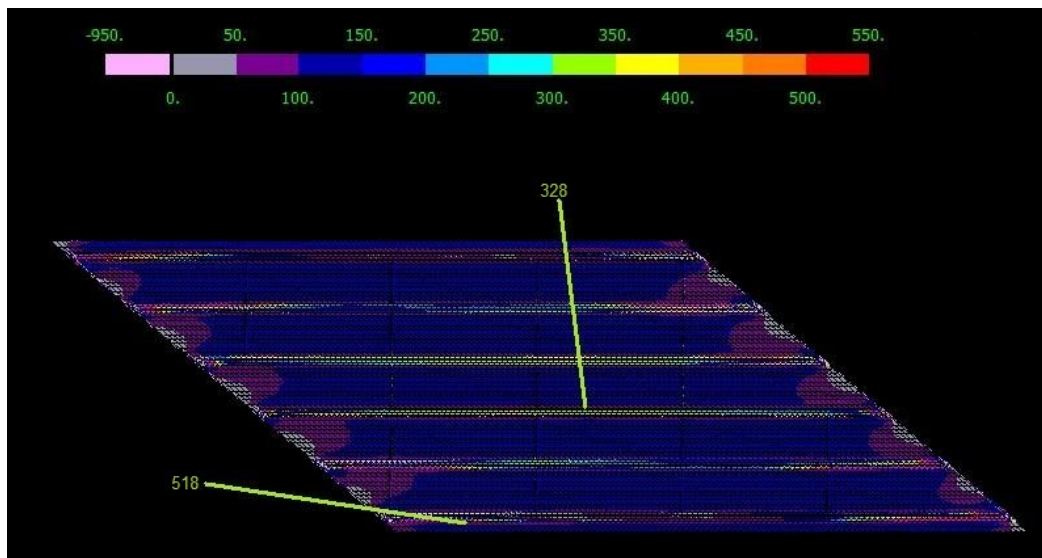
Figure 5.55 Contour plots for maximum principal stress subjected to uniform temperature load

(span length = 120 ft, steel beam spacing = 10 ft, skew angle = 50°)

Table 5.8 Principal stress of typical Michigan steel girder bridges (psi)

	Skew angle	Truck	Lane	Gradient	Uniform
120'-6'	0°	4926	1896	197	200
	30°	4775	1804	183	120
	50°	4852	1467	186	80
120'-10'	0°	4783	1508	312	458
	30°	4795	1533	314	460
	50°	4655	1458	291	328
180'-6'	0°	3747	1578	123	104
	30°	3690	1577	123	104
	50°	3642	1571	116	31
180'-10'	0°	3852	1847	214	184
	30°	3741	1895	208	192
	50°	3686	1868	181	184

Tables 5.8 and 5.9 show the maximum principal stresses of the typical Michigan steel girder bridges and prestressed concrete girder bridges, respectively. The ratio of thermal effect to the AASHTO design live load obtained from this result is shown in Figure 5.56 for gradient temperature change and Figure 5.57 for uniform temperature change. As shown in the figures, the thermal effect of prestressed concrete girder bridges is more significant than that of steel girder bridges. The difference in the temperature gradient distribution in Figure 5.45 is the reason for this. In addition, it is observed that the bridge with wider beam spacings have more significant thermal effect. The cause for this trend is possibly that the wider beam spacing makes

the distance between neutral axis of the composite section and bottom flange longer, and then the longer distance makes the stress at the bottom flange higher. According to the analysis, the effect of thermal loads on moment is at most 12% and therefore it should not be neglected.

Table 5.9 Principal stress of typical Michigan prestressed concrete girder bridges (psi)

	Skew angle	Truck	Lane	Gradient	Uniform
60'-6'	0°	381	144	44	36
	30°	380	145	46	32
	50°	385	142	52	29
120'-6'	0°	397	183	55	42
	30°	415	181	59	40
	50°	417	177	66	39
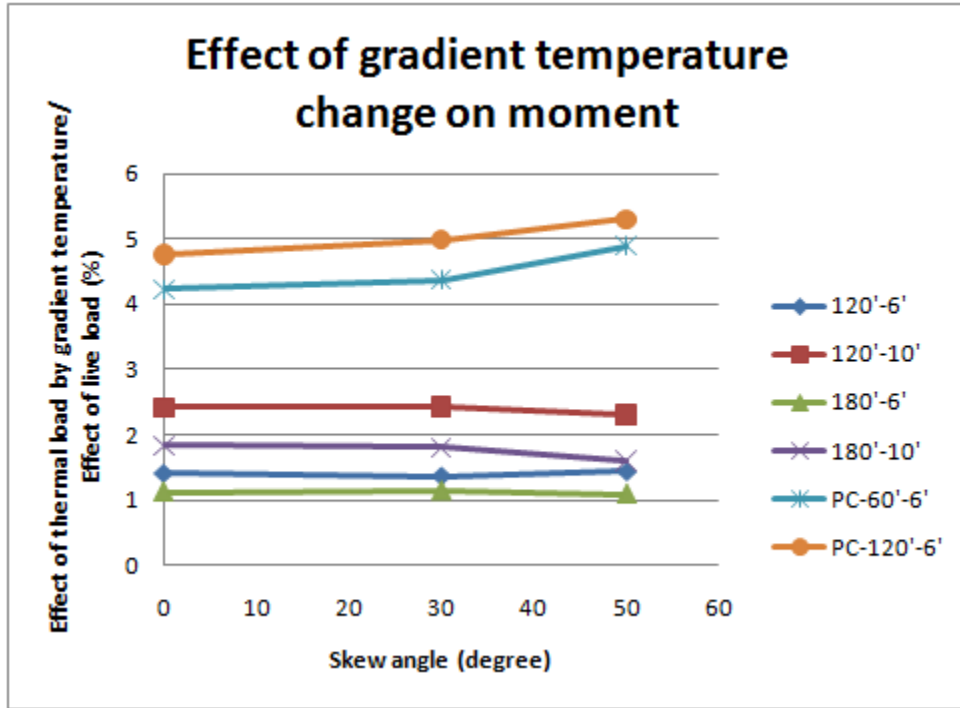
Figure 5.56 Effect of gradient thermal load on moment
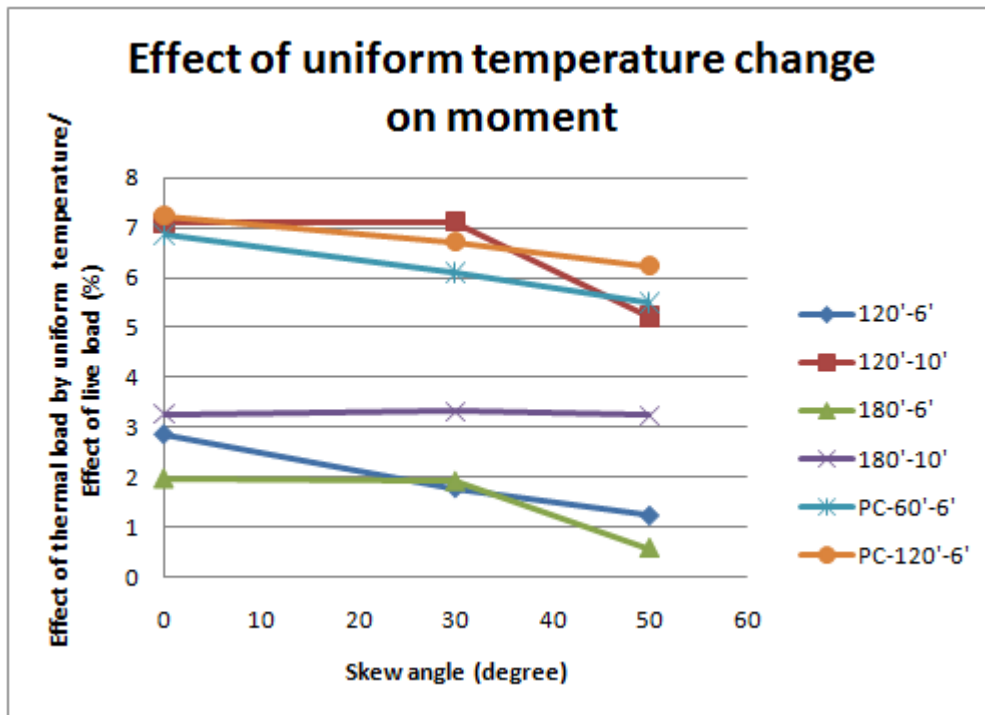
Figure 5.57 Effect of uniform thermal load on moment

5.3.4 Analysis results for shear

In this section, the effect of temperature on shear is discussed. The main focus is on the shear force at the obtuse corner as one of the main focus points of skewed bridge design. As done in the previous section, thermal loads by gradient temperature and uniform temperature are applied to the typical Michigan skewed bridges. The comparison results for the reaction force at the obtuse corner between traffic loads and thermal loads are shown in Tables 5.10 and 5.11.

Table 5.10 Reaction force of typical Michigan steel girder bridges at obtuse corner (lb)

	Skew angle	Truck	Lane	Gradient	Uniform
120'-6'	0°	44009	21722	2574	889
	30°	44621	22245	3211	811
	50°	44400	23892	4289	900
120'-10'	0°	52770	27202	5821	2054
	30°	52721	27149	6721	1389
	50°	53301	29521	7032	1121
180'-6'	0°	44362	26546	4601	1165
	30°	44321	28139	5312	1188
	50°	46211	29874	5489	1365
180'-10'	0°	54875	36798	9041	2649
	30°	53587	36124	10143	2401
	50°	57211	39158	10682	1604

Table 5.11 Reaction force of typical Michigan prestressed concrete bridges at obtuse corner (lb)

	Skew angle	Truck	Lane	Gradient	Uniform
60'-6'	0°	37782	10487	2784	120
	30°	35393	10245	2611	420
	50°	33810	11028	3214	1220
120'-6'	0°	42231	16987	4021	65
	30°	42121	17513	3862	115
	50°	41974	18768	4921	1643
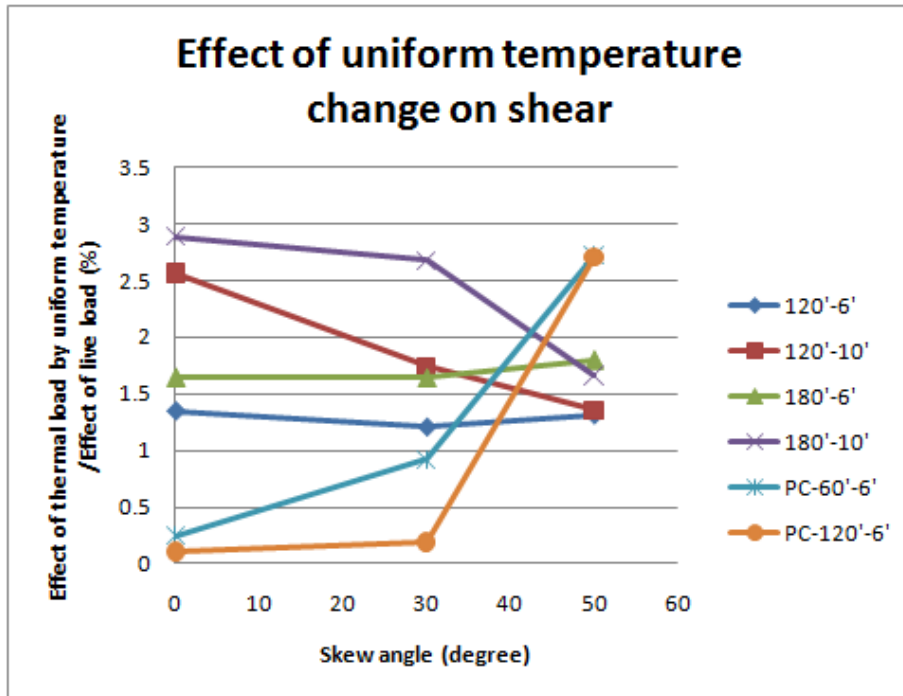
Figure 5.58 Effect of gradient thermal load on shear at obtuse corner
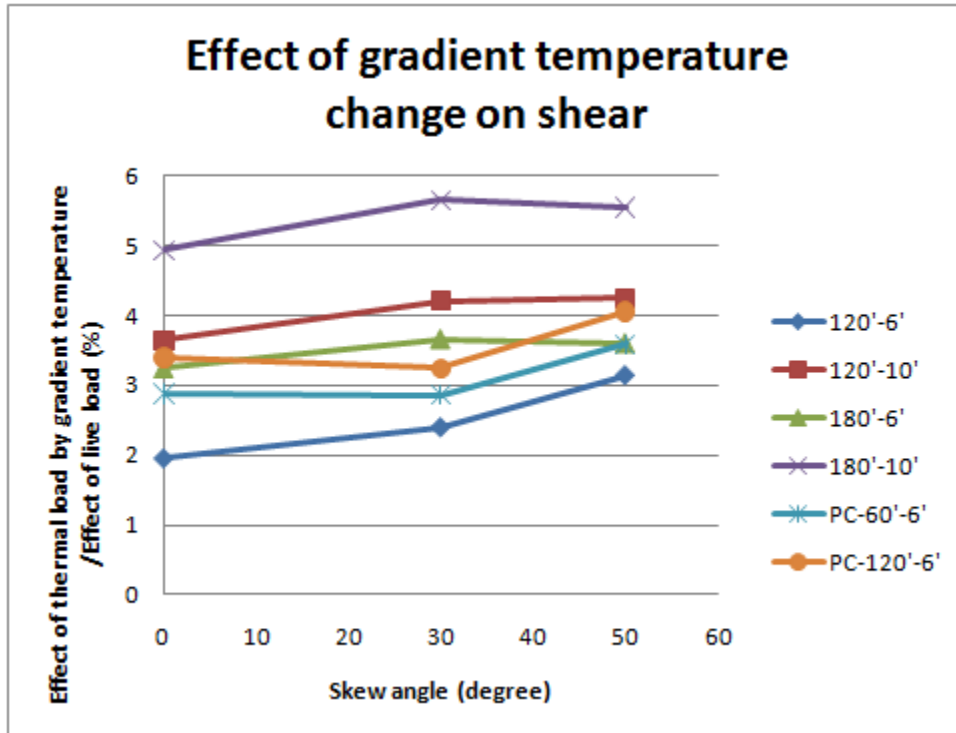
Figure 5.59   Effect of uniform thermal load on shear at obtuse corner

The ratio of thermal effect to the AASHTO HL93 live load effect obtained from this result is shown in Figure 5.58 for gradient temperature change and Figure 5.59 for uniform temperature change. Like the moment described in the previous chapter, wider beam spacing has more thermal effect on shear. According to these analysis results, the effect of thermal loads on shear and reaction is at most 12% and therefore it should not be neglected.

5.4 Summary

This chapter has presented the FEA calculation program for typical Michigan skewed highway bridges in this research project. In the analysis shown in Section 5.2, the moment and

shear distribution factors were derived and compared with AASHTO LRFD Bridge Design Specifications. FEA results for the "SS" end model shows that moment effect decreases and shear effect increases as the skewed angle increases, as seen in the moment distribution factor of the AASHTO LRFD specifications. However, the AASHTO LRFD specifications do not cover the "Fixed" and "Bearing" end conditions. The moment distribution factor for the "Fixed" end model is less than half of what the specifications give, and the shear distribution factor for the "Bearing" end model does not increase as the skew angle increases. It can happen that the structural members are overdesigned or underdesigned if it is designed as per the specifications.

In Section 5.3, the thermal effects caused by uniform temperature change and gradient temperature change on moment and shear are investigated. Results have shown that thermal effect can be as high as 12% of the effect of AASHTO live load effect for both moment and shear and therefore it should receive adequate attention in the design process.

Chapter 6

Analytical Solution Program

In this chapter, an analytical solution for skewed thick plates is pursued and successfully developed. Skewed plates are important structural elements used in a wide range of applications including skewed bridges where the reinforced concrete deck can be viewed as a typical thick plate. Skewed plate analytical solutions presented in this chapter can be used to develop their counterpart for skewed bridges by assembling several plates supported by beams at their edges to form the bridge system.

The advantage of such analytical solutions is that the end user will not need to deal with complex model building and computational issues like element type, element size, mesh convergence, etc, since there is no mesh nor iteration needed to solve the problem. The computer will be used as a powerful calculator to performed the required calculations. When such a computer program is written to implement the analytical solution for routine application, the required input data from the user will be identical to those used in routine design, such as span length, beam spacing, deck thickness, concrete material properties, steel material properties, etc.

In this chapter, two plate theories are discussed first to provide the background. These theories have led to corresponding governing equations of three-dimensional elastic medium based on respective basic assumptions, but not yet for thick plates in an oblique coordinate system. Next, the concept of oblique coordinate system is introduced for dealing with skewed thin and thick plates and its relationship to the rectangular coordinate system. Then, the

governing differential equation of skewed thick plates subjected to truck wheel loads is developed based on the Reissner-Mindlin theory in the oblique coordinate system. The equation is then solved using a sum of polynomial and trigonometric function series. Analytical solution results for several application examples are also compared in this chapter to corresponding solutions reported in the literature derived from numerical methods. Their agreement indicates that the proposed analytical solution approach is equally effective, with an advantage of being more user friendly for routine application.

6.1 Introduction

6.1.1 Plate theories for various plate thicknesses

A number of theories exist for analyzing plates and are discussed in this section. A plate is also a three-dimensional structure whose general governing equations are as follows.

(1) Equilibrium equations:

$$\frac{\partial \sigma_x}{\partial x} + \frac{\partial \tau_{xy}}{\partial y} + \frac{\partial \tau_{xz}}{\partial z} + \overline{X} = 0$$

$$\frac{\partial \tau_{xy}}{\partial x} + \frac{\partial \sigma_y}{\partial y} + \frac{\partial \tau_{yz}}{\partial z} + \overline{Y} = 0$$

$$\frac{\partial \tau_{xz}}{\partial x} + \frac{\partial \tau_{yz}}{\partial y} + \frac{\partial \sigma_z}{\partial z} + \overline{Z} = 0$$

$$\ldots\ldots\ldots\ldots\ldots\ldots\ldots\ldots(6.1)$$

(2) Constitutive equations:

$$\sigma_x = 2G\left(\varepsilon_x + \frac{v}{1-2v}(\varepsilon_x + \varepsilon_y + \varepsilon_z)\right)$$

$$\sigma_y = 2G\left(\varepsilon_y + \frac{v}{1-2v}(\varepsilon_x + \varepsilon_y + \varepsilon_z)\right)$$

$$\sigma_z = 2G\left(\varepsilon_z + \frac{v}{1-2v}(\varepsilon_x + \varepsilon_y + \varepsilon_z)\right)$$

$$\tau_{xy} = G\gamma_{xy}$$

$$\tau_{xz} = G\gamma_{xz}$$

$$\tau_{yz} = G\gamma_{yz}$$

…………………………..(6.2)

(3) Compatibility equations:

$$\varepsilon_x = \frac{\partial u}{\partial x}, \varepsilon_y = \frac{\partial v}{\partial y}, \varepsilon_z = \frac{\partial w}{\partial z}$$

$$\gamma_{xy} = \frac{\partial v}{\partial x} + \frac{\partial u}{\partial y}, \gamma_{xz} = \frac{\partial w}{\partial x} + \frac{\partial u}{\partial z}, \gamma_{yz} = \frac{\partial w}{\partial y} + \frac{\partial v}{\partial z}$$

…………………….(6.3)

Because there are 15 unknowns (6 stresses σ_x, σ_y, σ_z, τ_{xy}, τ_{xz}, and τ_{yz}, 6 strains ε_x, ε_y, ε_z, γ_{xy}, γ_{xz}, and γ_{yz}, and 3 displacements u, v, and w) in 15 equations, the solution exists, theoretically. However, it is extremely difficult if not impossible to solve the above equations analytically because of their complexity and interaction. Thus, assumptions are used for specific problems to simplify the process of solution, such as plates and shells with respect to the shape of the structure, or plane stress or plane strain problems with respect to resulting stress or strain distribution.

Plates can be roughly categorized into four groups defined in Table 6.1 (Hangai 1995) according to the ratio of their thickness to typical edge length. Typical decks of composite

highway bridges can be categorized into the group of thick plates. Namely their ratio of thickness to edge length is in the range of 10^{-1} to 10^{0}. Therefore, analytical solution for bridge deck on skewed structures is to be developed here based on the Reissner-Mindlin theory.

Table 6.1. Plate categories

Thickness of plates (thickness/edge length)	Applicable theory
Extremely thick plates (10^{0})	Higher order theory
Thick plates (10^{-1}~10^{0})	Reissner-Mindlin theory
Thin plates (10^{-1})	Kirchhoff theory
Extremely thin plates (10^{-2})	Membrane theory

6.1.2 Kirchhoff theory and Reissner-Mindlin theory

The most fundamental and classical plate theory is the Kirchhoff theory for thin plates. This theory consists of the so called Kirchhoff assumptions as follows (Reddy 2007):

(1) The transverse deformation w is infinitesimal.

(2) The straight lines perpendicular to the mid-surface (*i.e.,* the transverse normals) before deformation remain straight after deformation.

(3) The transverse normals do not experience elongation (*i.e.,* are inextensible).

(4) The transverse normals rotate such that they remain perpendicular to the middle surface after deformation.

The above four assumptions are mathematically formulated as follows:

(1) Infinitesimal deformation

$$w \ll h, \left(\frac{\partial w}{\partial x}\right)^2 \ll 1, \left(\frac{\partial w}{\partial y}\right)^2 \ll 1 \quad \text{................................(6.4)}$$

(2) No mid-surface deformation along the x and y directions

$$\varepsilon_x\big|_{z=0} = 0, \varepsilon_y\big|_{z=0} = 0, \gamma_{xy}\big|_{z=0} = 0 \quad \text{....................................(6.5)}$$

(3) The transverse normals maintain their length and the stress along z-direction is zero

$$\varepsilon_z = 0, \sigma_z = 0 \quad \text{...(6.6)}$$

(4) The transverse normals and mid-surface remain perpendicular

$$\gamma_{xz} = 0, \gamma_{yz} = 0 \quad \dots\dots\dots\dots\dots\dots\dots\dots\dots\dots\dots\dots\dots\dots\dots(6.7)$$

By applying these assumptions in Equations 6.4 to 6.7 in 6.1 to 6.3, the following Equation 6.8 is obtained.

$$D\left(\frac{\partial^4 w}{\partial x^4} + 2\frac{\partial^4 w}{\partial x^2 \partial y^2} + \frac{\partial^4 w}{\partial y^4}\right) = p \quad \dots\dots\dots\dots\dots\dots\dots\dots\dots(6.8)$$

where D is the flexural rigidity of the plate, w is the transverse deformation, and p is the transverse load.

The Kirchhoff theory is widely used in plate analysis, but suffers from under-predicting deflections when the thickness-to-edge-length ratio exceeds 1/20 because it neglects the effect of the transverse shear deformation (*e.g.,* Reddy 2007).

To address this issue, the Reissner-Mindlin theory was developed by Reissner (1945) and Mindlin (1951). This theory relaxes the perpendicular restriction for the transverse normals and allows them to have arbitrary but constant rotation to account for the effect of transverse shear deformation. Namely, the assumption in Equation 6.7 is not dropped in the Reissner-Mindlin theory. Note that the relationship between the Kichhoff and Reissner-Mindlin theories for plates is analogical to that between the Bernoulli-Euler and Timoshenko theories for beams. In the next section, skewed thick plates are analyzed based on the Reissner-Mindlin theory.

6.2   Governing equation in an oblique coordinate system

When a plate's boundary profile is a parallelogram, the oblique Cartesian coordinate system can be advantageous. Next, we first present the concept of oblique coordinate system and

then derive the governing differential equation of skewed thick plates based on the Reissner-Mindlin theory in the oblique coordinate system.

6.2.1 Oblique coordinate system

Figure 6.1 shows an oblique coordinate system spanned by the X and Y axes, along with the reference rectangular system by x and y, with angle YOy denoted as skew angle α. Parallelogram $ABCD$ in Figure 6.1 represents the skewed plate of interest, and the edge lengths CD and AD are $2a$ and $2b$, respectively. Hereafter, quantities with subscript of upper-case letters (*i.e.*, M_X and M_Y) are those in the oblique coordinate system and quantities with subscript of lower-case letters (*i.e.*, M_x, and M_y) are those in the rectangular coordinate system.
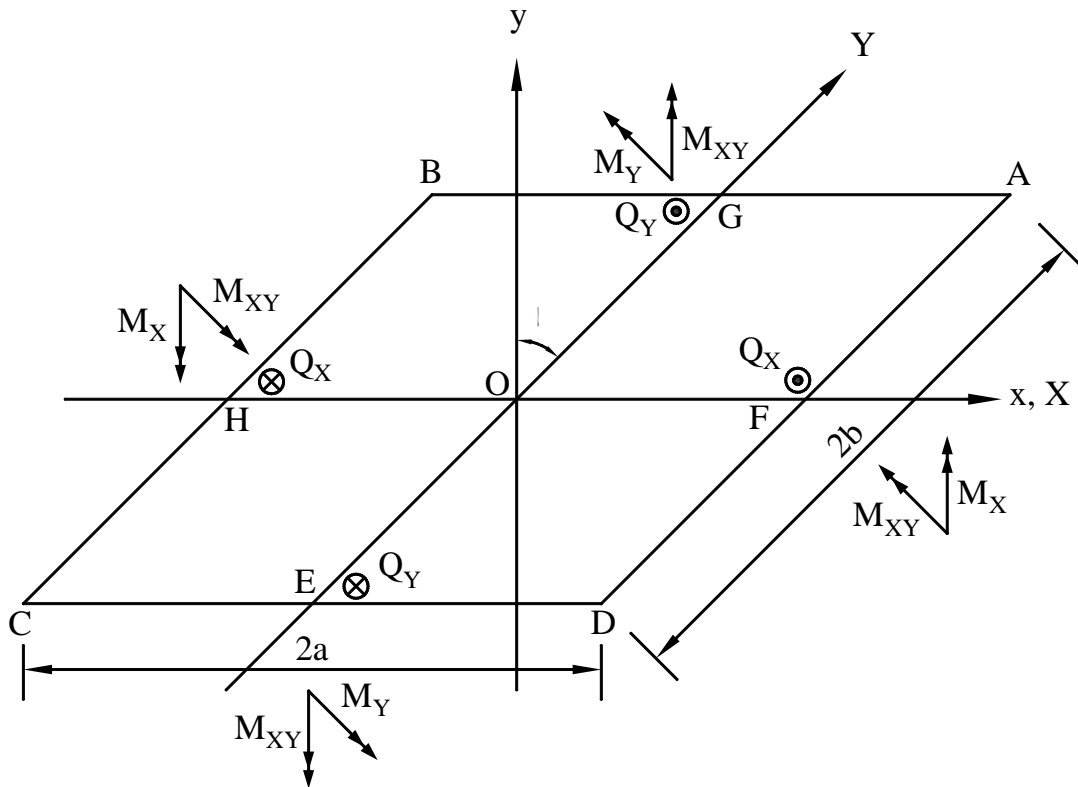
Figure 6.1   A skewed plate defined in an oblique coordinate system

First, the relation between the rectangular and oblique coordinate system is provided as follows in Equations 6.9 to 6.11 (Morley 1963, Liew and Han 1997). Equation 6.9 is the basis for deriving the rest of the equations.

$$\begin{pmatrix} X \\ Y \end{pmatrix} = \begin{pmatrix} 1 & \tan\alpha \\ 0 & \sec\alpha \end{pmatrix} \begin{pmatrix} x \\ y \end{pmatrix} \quad\ldots\ldots\ldots\ldots\ldots\ldots\ldots\ldots\ldots\ldots\ldots\ldots\text{(6.9)}$$

$$\begin{pmatrix} \dfrac{\partial}{\partial X} \\[2ex] \dfrac{\partial}{\partial Y} \end{pmatrix} = \begin{pmatrix} 1 & 0 \\ \sin\alpha & \cos\alpha \end{pmatrix} \begin{pmatrix} \dfrac{\partial}{\partial x} \\[2ex] \dfrac{\partial}{\partial y} \end{pmatrix} \quad\ldots\ldots\ldots\ldots\ldots\ldots\ldots\ldots\ldots\text{(6.10)}$$

$$\begin{pmatrix} \phi_X \\ \phi_Y \end{pmatrix} = \begin{pmatrix} 1 & 0 \\ \sin\alpha & \cos\alpha \end{pmatrix} \begin{pmatrix} \phi_x \\ \phi_y \end{pmatrix} \quad\ldots\ldots\ldots\ldots\ldots\ldots\ldots\ldots\ldots\ldots\text{(6.11)}$$

In the above equations, ϕ_x, ϕ_y, ϕ_X, and ϕ_Y are the rotations normal to the x, y, X, and Y axes respectively. The relationship between the strain, moment, and shear of the two coordinate systems can be derived using Equations 6.9 to 6.11. This derivation leads to Equations 6.12 to 6.14 as follows.

$$\begin{pmatrix} \varepsilon_X \\ \varepsilon_Y \\ \gamma_{XY} \end{pmatrix} = \begin{pmatrix} 1 & 0 & 0 \\ \sin^2\alpha & \cos^2\alpha & \sin\alpha\cos\alpha \\ 2\sin\alpha & 0 & \cos\alpha \end{pmatrix} \begin{pmatrix} \varepsilon_x \\ \varepsilon_y \\ \gamma_{xy} \end{pmatrix} \quad\ldots\ldots\ldots\ldots\ldots\ldots\text{(6.12)}$$

$$\begin{pmatrix} M_X \\ M_Y \\ M_{XY} \end{pmatrix} = \begin{pmatrix} \cos\alpha & \sin\alpha\tan\alpha & -2\sin\alpha \\ 0 & \sec\alpha & 0 \\ 0 & -\tan\alpha & 1 \end{pmatrix} \begin{pmatrix} M_x \\ M_y \\ M_{xy} \end{pmatrix} \quad\text{................(6.13)}$$

$$\begin{pmatrix} Q_X \\ Q_Y \end{pmatrix} = \begin{pmatrix} \cos\alpha & -\sin\alpha \\ 0 & 1 \end{pmatrix} \begin{pmatrix} Q_x \\ Q_y \end{pmatrix} \quad\text{................(6.14)}$$

where ε and γ are the normal and shear strains. M and Q indicate the moment and shear force in the respective directions noted by the subscript and they are also presented in Figure 6.1. The stress-strain relationship of the oblique and rectangular coordinate systems are described in the following Equations 6.15 and 6.16) respectively.

$$\begin{pmatrix} M_x \\ M_y \\ M_{xy} \end{pmatrix} = [D_r] \begin{pmatrix} \varepsilon_x \\ \varepsilon_y \\ \gamma_{xy} \end{pmatrix} \quad\text{................(6.15)}$$

$$\begin{pmatrix} M_X \\ M_Y \\ M_{XY} \end{pmatrix} = [D_o] \begin{pmatrix} \varepsilon_X \\ \varepsilon_Y \\ \gamma_{XY} \end{pmatrix} \quad\text{................(6.16)}$$

where $[D_r]$ and $[D_o]$ are the flexural stiffness matrices respectively under the rectangular and oblique coordinate systems. The flexural stiffness matrices relate the moments to the curvatures in the respective coordinate systems. For example, $[D_r]$ in the rectangular coordinate system for isotropic material is (Timoshenko 1959):

$$[D_r] = \frac{Et^3}{12} \begin{pmatrix} \dfrac{1}{1-v^2} & \dfrac{v}{1-v^2} & 0 \\[2mm] \dfrac{v}{1-v^2} & \dfrac{1}{1-v^2} & 0 \\[2mm] 0 & 0 & \dfrac{1}{2(1+v)} \end{pmatrix}$$ ………….....…………….(6.17)

where E is the Young's modulus, v is the Poisson's ratio, t is the thickness of the plate. Since Reissner-Mindlin theory assumes that the transverse normals do not experience elongation, Equations 6.15 and 6.16 are changed into the following Equations 6.18 and 6.19.

$$\begin{Bmatrix} M_x \\ M_y \\ M_{xy} \end{Bmatrix} = [D_r] \begin{Bmatrix} \dfrac{\partial \phi_x}{\partial x} \\[2mm] \dfrac{\partial \phi_y}{\partial y} \\[2mm] \dfrac{\partial \phi_x}{\partial y} + \dfrac{\partial \phi_y}{\partial x} \end{Bmatrix}$$ …………..........………………..(6.18)

$$\begin{Bmatrix} M_X \\ M_Y \\ M_{XY} \end{Bmatrix} = [D_o] \begin{Bmatrix} \dfrac{\partial \phi_X}{\partial X} \\[2mm] \dfrac{\partial \phi_Y}{\partial Y} \\[2mm] \dfrac{\partial \phi_X}{\partial Y} + \dfrac{\partial \phi_Y}{\partial X} \end{Bmatrix}$$ …………..........…….…………….(6.19)

The relationship between $[D_r]$ and $[D_o]$ can be calculated readily using the following equation 6.20:

$$\begin{pmatrix} M_X \\ M_Y \\ M_{XY} \end{pmatrix} = \begin{pmatrix} \cos\alpha & \sin\alpha\tan\alpha & -2\sin\alpha \\ 0 & \sec\alpha & 0 \\ 0 & -\tan\alpha & 1 \end{pmatrix} \begin{pmatrix} M_x \\ M_y \\ M_{xy} \end{pmatrix}$$

$$= \begin{pmatrix} \cos\alpha & \sin\alpha\tan\alpha & -2\sin\alpha \\ 0 & \sec\alpha & 0 \\ 0 & -\tan\alpha & 1 \end{pmatrix} [D_r] \begin{pmatrix} \varepsilon_x \\ \varepsilon_y \\ \gamma_{xy} \end{pmatrix}$$

$$= \begin{pmatrix} \cos\alpha & \sin\alpha\tan\alpha & -2\sin\alpha \\ 0 & \sec\alpha & 0 \\ 0 & -\tan\alpha & 1 \end{pmatrix} [D_r] \begin{pmatrix} 1 & 0 & 0 \\ \sin^2\alpha & \cos^2\alpha & \sin\alpha\cos\alpha \\ 2\sin\alpha & 0 & \cos\alpha \end{pmatrix}^{-1} \begin{pmatrix} \varepsilon_X \\ \varepsilon_Y \\ \gamma_{XY} \end{pmatrix}$$

$$= [D_o] \begin{pmatrix} \varepsilon_X \\ \varepsilon_Y \\ \gamma_{XY} \end{pmatrix}$$

....(6.20)

Namely,

$$[D_o] = \begin{pmatrix} \cos\alpha & \sin\alpha\tan\alpha & -2\sin\alpha \\ 0 & \sec\alpha & 0 \\ 0 & -\tan\alpha & 1 \end{pmatrix} [D_r] \begin{pmatrix} 1 & 0 & 0 \\ \sin^2\alpha & \cos^2\alpha & \sin\alpha\cos\alpha \\ 2\sin\alpha & 0 & \cos\alpha \end{pmatrix}^{-1}$$

..........(6.21)

Note that Equation 6.21 is applicable not only for isotropic material, but also for more complex materials, such as orthotropic or anisotropic materials.

If the relationship between the shear force and deflection is described as in Equations 6.22 and 6.23, the relationship between the extensional stiffness matrices $[A_r]$ and $[A_o]$ in the equations are derived from Equation 6.24:

$$\begin{pmatrix} Q_x \\ Q_y \end{pmatrix} = K_s[A_r] \begin{pmatrix} \dfrac{\partial w}{\partial x} + \phi_x \\ \dfrac{\partial w}{\partial y} + \phi_y \end{pmatrix}$$ ………….......…………….(6.22)

$$\begin{pmatrix} Q_X \\ Q_Y \end{pmatrix} = K_s[A_O] \begin{pmatrix} \dfrac{\partial w}{\partial X} + \phi_X \\ \dfrac{\partial w}{\partial Y} + \phi_Y \end{pmatrix}$$ ………….......…………….(6.23)

$$\begin{pmatrix} Q_X \\ Q_Y \end{pmatrix} = \begin{pmatrix} \cos\alpha & -\sin\alpha \\ 0 & 1 \end{pmatrix} \begin{pmatrix} Q_x \\ Q_y \end{pmatrix}$$

$$= K_s \begin{pmatrix} \cos\alpha & -\sin\alpha \\ 0 & 1 \end{pmatrix} [A_r] \begin{pmatrix} \dfrac{\partial w}{\partial x} + \phi_x \\ \dfrac{\partial w}{\partial y} + \phi_y \end{pmatrix}$$

$$= K_s \begin{pmatrix} \cos\alpha & -\sin\alpha \\ 0 & 1 \end{pmatrix} [A_r] \begin{pmatrix} 1 & 0 \\ \sin\alpha & \cos\alpha \end{pmatrix}^{-1} \begin{pmatrix} \dfrac{\partial w}{\partial X} + \phi_X \\ \dfrac{\partial w}{\partial Y} + \phi_Y \end{pmatrix}$$

$$= K_s[A_O] \begin{pmatrix} \dfrac{\partial w}{\partial X} + \phi_X \\ \dfrac{\partial w}{\partial Y} + \phi_Y \end{pmatrix}$$ ……(6.24)

Namely,

$$[A_O] = \begin{pmatrix} \cos\alpha & -\sin\alpha \\ 0 & 1 \end{pmatrix} [A_r] \begin{pmatrix} 1 & 0 \\ \sin\alpha & \cos\alpha \end{pmatrix}^{-1}$$ ………(6.25)

where w is the transverse deformation perpendicular to the plane of the plate and K_s is the shear correction factor to account for non-uniform transverse shear distribution.

The extensional stiffness matrix relates the shear forces to the shear strains. For example, $[A_r]$ for isotropic material is

$$[A_r] = \frac{Et}{2(1+v)}\begin{pmatrix} 1 & 0 \\ 0 & 1 \end{pmatrix} \qquad\text{.........(6.26)}$$

Based on the relationships (6.21) and (6.25), the governing equation of skewed thick plate bending is developed in the next section.

6.2.2 Governing equation for bending of skewed thick plates in oblique system

Hereafter, matrices $[D_o]$ and $[A_o]$ are referred to using their respective elements D_{11} to D_{33} and A_{44} to A_{55} as follows:

$$[D_O] = \begin{bmatrix} D_{11} & D_{12} & D_{13} \\ D_{12} & D_{22} & D_{23} \\ D_{13} & D_{23} & D_{33} \end{bmatrix}, [A_o] = \begin{bmatrix} A_{55} & A_{45} \\ A_{45} & A_{44} \end{bmatrix} \qquad\text{...............................(6.27)}$$

where the diagonal elements of $[D_o]$ relate the moments to the curvatures in the same directions. The off-diagonal terms relate the same moments to the curvatures in other directions due to the Poisson's effect and coordinate system obliquity. Similarly, the diagonal components of $[A_o]$ relate the shear forces to the shear strains in the same direction, and off-diagonal terms to the shear strains in other directions due to obliquity.

The following Equations 6.28 to 6.30 are the equilibrium conditions of the skewed plate shown in Figure 6.1 (Morley 1962).

(1) Equilibrium of forces along the z direction :

$$\frac{\partial Q_X}{\partial X} + \frac{\partial Q_Y}{\partial Y} = -Q$$

....(6.28)

(2) Equilibrium of moments along the x axis :

$$\frac{\partial M_X}{\partial X} + \frac{\partial M_{XY}}{\partial Y} = Q_X$$

....(6.29)

(3) Equilibrium of moments along the y axis :

$$\frac{\partial M_Y}{\partial Y} + \frac{\partial M_{XY}}{\partial X} = Q_Y$$

....(6.30)

where Q in Equation 6.28 is the load applied over the upper surface of the plate.

By substituting the moments and shear forces in the oblique coordinate system in Equations 6.21, 6.25, and 6.27 into the equilibrium conditions in Equations 6.28 to 6.30, the following Equations 6.31 to 6.33 are obtained in the oblique system.

$$K_s A_{45}\left(\frac{\partial^2 w}{\partial X \partial Y} + \frac{\partial \phi_X}{\partial Y}\right) + K_s A_{45}\left(\frac{\partial^2 w}{\partial X \partial Y} + \frac{\partial \phi_Y}{\partial X}\right) + K_s A_{55}\left(\frac{\partial^2 w}{\partial X^2} + \frac{\partial \phi_X}{\partial X}\right) + K_s A_{44}\left(\frac{\partial^2 w}{\partial Y^2} + \frac{\partial \phi_Y}{\partial Y}\right) = -Q$$

........(6.31)

$$D_{11}\frac{\partial^2 \phi_X}{\partial X^2} + D_{12}\frac{\partial^2 \phi_Y}{\partial X \partial Y} + D_{13}\left(2\frac{\partial^2 \phi_X}{\partial X \partial Y} + \frac{\partial^2 \phi_Y}{\partial X^2}\right) + D_{23}\frac{\partial^2 \phi_Y}{\partial Y^2} + D_{33}\left(\frac{\partial^2 \phi_X}{\partial Y^2} + \frac{\partial^2 \phi_Y}{\partial X \partial Y}\right)$$

$$= K_s A_{45}\left(\frac{\partial w}{\partial Y} + \phi_Y\right) + K_s A_{55}\left(\frac{\partial w}{\partial X} + \phi_X\right)$$

........(6.32)

$$D_{12}\frac{\partial^2 \phi_X}{\partial X \partial Y} + D_{13}\frac{\partial^2 \phi_X}{\partial X^2} + D_{22}\frac{\partial^2 \phi_Y}{\partial Y^2} + D_{23}\left(\frac{\partial^2 \phi_X}{\partial Y^2} + 2\frac{\partial^2 \phi_Y}{\partial X \partial Y}\right) + D_{33}\left(\frac{\partial^2 \phi_X}{\partial X \partial Y} + \frac{\partial^2 \phi_Y}{\partial X^2}\right)$$

$$= K_s A_{44}\left(\frac{\partial w}{\partial Y} + \phi_Y\right) + K_s A_{45}\left(\frac{\partial w}{\partial X} + \phi_X\right)$$

........(6.33)

137

Note that Reddy (2004, 2007) also presented similar governing equations but for solving the problem of simply supported straight thick plates.

To make the solution process simpler, a new potential function ψ is introduced below in this research project for skewed thick plates. We assume that w consists of terms up to the 4th derivative and ϕ_X and ϕ_Y up to the 3rd derivative of ψ, with respect to the spatial variables X and Y. The following relations in Equations 6.34 to 6.36 are obtained to satisfy Equations 6.32 and 6.33.

$$
\begin{aligned}
w = & \left(D_{13}^2 - D_{11}D_{33}\right)\frac{\partial^4\psi}{\partial X^4} + 2\left(D_{12}D_{13} - D_{11}D_{23}\right)\frac{\partial^4\psi}{\partial X^3\partial Y} + \left(D_{12}^2 - D_{11}D_{22} - 2D_{13}D_{23} + 2D_{12}D_{33}\right)\frac{\partial^4\psi}{\partial X^2\partial Y^2} + \\
& 2\left(-D_{13}D_{22} + D_{12}D_{23}\right)\frac{\partial^4\psi}{\partial X\partial Y^3} + \left(D_{23}^2 - D_{22}D_{33}\right)\frac{\partial^4\psi}{\partial Y^4} + \left\{A_{44}D_{11} - 2A_{45}D_{13} + A_{55}D_{33}\right\}K_s\frac{\partial^2\psi}{\partial X^2} + \\
& 2\left\{A_{44}D_{13} + A_{55}D_{23} - A_{45}(D_{12} + D_{33})\right\}K_s\frac{\partial^2\psi}{\partial X\partial Y} + \left\{A_{55}D_{22} - 2A_{45}D_{23} + A_{44}D_{33}\right\}K_s\frac{\partial^2\psi}{\partial Y^2} + (A_{45}^2 - A_{44}A_{55})K_s^2\psi
\end{aligned}
$$

....(6.34)

$$
\begin{aligned}
\phi_X = & \left(A_{45}D_{13} - A_{55}D_{33}\right)K_s\frac{\partial^3\psi}{\partial X^3} + \left\{A_{44}D_{13} - 2A_{55}D_{23} + A_{45}D_{12}\right\}K_s\frac{\partial^3\psi}{\partial X^2\partial Y} + \\
& \left\{-A_{55}D_{22} - A_{45}D_{23} + A_{44}(D_{12} + D_{33})\right\}K_s\frac{\partial^3\psi}{\partial X\partial Y^2} + \left(-A_{45}D_{22} + A_{44}D_{23}\right)K_s\frac{\partial^3\psi}{\partial Y^3} + \left(-A_{45}^2 + A_{44}A_{55}\right)K_s^2\frac{\partial\psi}{\partial X}
\end{aligned}
$$

....(6.35)

$$
\begin{aligned}
\phi_Y = & \left(-A_{45}D_{11} + A_{55}D_{13}\right)K_s\frac{\partial^3\psi}{\partial X^3} + \left\{-A_{44}D_{11} - A_{45}D_{13} + A_{55}(D_{12} + D_{33})\right\}K_s\frac{\partial^3\psi}{\partial X^2\partial Y} + \\
& \left\{-2A_{44}D_{13} + A_{55}D_{23} + A_{45}D_{12}\right\}K_s\frac{\partial^3\psi}{\partial X\partial Y^2} + \left(A_{45}D_{23} - A_{44}D_{33}\right)K_s\frac{\partial^3\psi}{\partial Y^3} + \left(-A_{45}^2 + A_{44}A_{55}\right)K_s^2\frac{\partial\psi}{\partial Y}
\end{aligned}
$$

…..(6.36)

By substituting these relations into Equation 6.31, the governing equation based on the the Reissner-Mindlin theory for skewed thick plates is then formulated as a 6th order partial differential equation as follows

$$
L(\psi) = -Q
$$

....(6.37)

where L is a linear differential operator in the oblique coordinate system:

$$L = A_{55}(D_{13}{}^2 - D_{11}D_{33})K_s \frac{\partial^6}{\partial X^6} + 2\left\{A_{55}\left(D_{12}D_{13} - D_{11}D_{23}\right) + A_{45}\left(D_{13}{}^2 - D_{11}D_{33}\right)\right\}K_s \frac{\partial^6}{\partial X^5 \partial Y} +$$

$$\{A_{44}\left(D_{13}{}^2 - D_{11}D_{33}\right) + 4A_{45}\left(D_{12}D_{13} - D_{11}D_{23}\right) + A_{55}\left(D_{12}{}^2 - D_{11}D_{22} - 2D_{13}D_{23} + 2D_{12}D_{33}\right)\}K_s \frac{\partial^6}{\partial X^4 \partial Y^2} +$$

$$\{2A_{44}\left(D_{12}D_{13} - D_{11}D_{23}\right) + 2A_{55}\left(-D_{13}D_{22} + D_{12}D_{23}\right) +$$

$$2A_{45}\left(D_{12}{}^2 - 2D_{13}D_{23} + 2D_{12}D_{33} - D_{11}D_{22}\right)\}K_s \frac{\partial^6}{\partial X^3 \partial Y^3} + \{A_{44}\left(D_{12}{}^2 - D_{11}D_{22} - 2D_{13}D_{23} + 2D_{12}D_{33}\right) +$$

$$A_{55}\left(D_{23}{}^2 - D_{22}D_{33}\right) + 4A_{45}\left(D_{12}D_{23} - D_{13}D_{22}\right)\}K_s \frac{\partial^6}{\partial X^2 \partial Y^4} + 2\{A_{45}\left(D_{23}{}^2 - D_{22}D_{33}\right) +$$

$$A_{44}\left(D_{12}D_{23} - D_{13}D_{22}\right)\}K_s \frac{\partial^6}{\partial X \partial Y^5} + A_{44}(D_{23}{}^2 - D_{22}D_{33})K_s \frac{\partial^6}{\partial Y^6} + D_{11}(A_{44}A_{55} - A_{45}{}^2)K_s{}^2 \frac{\partial^4}{\partial X^4} +$$

$$4D_{13}(A_{44}A_{55} - A_{45}{}^2)K_s{}^2 \frac{\partial^4}{\partial X^3 \partial Y} + 2(D_{12} + 2D_{33})\left(A_{44}A_{55} - A_{45}{}^2\right)K_s{}^2 \frac{\partial^4}{\partial X^2 \partial Y^2} +$$

$$4D_{23}\left(A_{44}A_{55} - A_{45}{}^2\right)K_s{}^2 \frac{\partial^4}{\partial X \partial Y^3} + D_{22}(A_{44}A_{55} - A_{45}{}^2)K_s{}^2 \frac{\partial^4}{\partial Y^4}$$

$$\text{...(6.38)}$$

6.3 Analytical solution in the series form

In the next two sections, a general solution to the governing differential Equation 6.37 is developed as the sum of a fundamental (homogeneous) and a particular (non-homogeneous) solution.

6.3.1 Homogeneous solution

The homogeneous solution ψ_h is the solution to Equation 6.37 for $Q=0$, obtained as a sum of polynomials ψ_{hp} in Equation 6.39 and trigonometric series ψ_{ht} in Equation 6.40 below. This structure of solution is inspired by Gupta (1974) for skewed thin plates.

$$\psi_{hp} = Z_1 + Z_2 X + Z_3 Y + Z_4 X^2 + Z_5 Y^2 + Z_6 XY + Z_7 X^3 + Z_8 X^2 Y + Z_9 XY^2 +$$

$$Z_{10}Y^3 + Z_{11}\left(D_{22}(-A_{45}^2 + A_{44}A_{55})X^4 - D_{11}(-A_{45}^2 + A_{44}A_{55})Y^4\right) +$$

$$Z_{12}\left(D_{23}(-A_{45}^2 + A_{44}A_{55})X^3 Y - D_{13}(-A_{45}^2 + A_{44}A_{55})XY^3\right)$$

$$\dots\dots(6.39)$$

$$\psi_{ht} = \sum_{h=1}^{\infty}(A_h C_{1X1} + iB_h C_{1X2} + C_h C_{2X1} + iD_h C_{2X2} + E_h C_{3X1} + iF_h C_{3X2} +$$

$$G_h S_{1X1} + iH_h S_{1X2} + I_h S_{2X1} + iJ_h S_{2X2} + K_h S_{3X1} + iL_h S_{3X2} +$$

$$M_h C_{1Y1} + iN_h C_{1Y2} + O_h C_{2Y1} + iP_h C_{2Y2} + Q_h C_{3Y1} + iR_h C_{3Y2} +$$

$$S_h S_{1Y1} + iT_h S_{1Y2} + U_h S_{2Y1} + iV_h S_{2Y2} + W_h S_{3Y1} + iX_h S_{3Y2})$$

$$\dots\dots(6.40)$$

where $i = \sqrt{-1}$ is the imaginary unit, and C_{eXf}, C_{eYf}, S_{eXf}, and S_{eYf} are trigonometric functions as

follows

$$C_{eXf} = \cos\frac{\pi h(X + \lambda_{eY}Y)}{2a} + (-1)^{f+1}\cos\frac{\pi h(X + \overline{\lambda_{eY}}Y)}{2a}$$

$$S_{eXf} = \sin\frac{\pi h(X + \lambda_{eY}Y)}{2a} + (-1)^{f+1}\sin\frac{\pi h(X + \overline{\lambda_{eY}}Y)}{2a}$$

$$C_{eYf} = \cos\frac{\pi h(\lambda_{eX}X + Y)}{2b} + (-1)^{f+1}\cos\frac{\pi h(\overline{\lambda_{eX}}X + Y)}{2b}$$

$$S_{eYf} = \sin\frac{\pi h(\lambda_{eX}X + Y)}{2b} + (-1)^{f+1}\sin\frac{\pi h(\overline{\lambda_{eX}}X + Y)}{2b}$$

$$(e = 1, 2, 3, \ f = 1, 2)$$

$$\dots\dots(6.41)$$

where the bar above λ denotes the conjugate of λ. λ_{1X}, λ_{2X}, λ_{3X}, λ_{1Y}, λ_{2Y}, and λ_{3Y} are the

eigenvalues to be obtained by satisfying $L(\psi_{ht})=0$. For example, λ_{eX} is derived by solving the

following equation.

$$L\left(\cos\frac{\pi h(\lambda_{eX}X + Y)}{2a} + \sin\frac{\pi h(\lambda_{eX}X + Y)}{2a}\right) = 0$$

$$\dots\dots(6.42)$$

The polynomial function ψ_{hp} in Equation 6.39 has 12 unknowns Z_1 to Z_{12}, and the trigonometric function ψ_{ht} in Equation 6.40 has $24l$ unknowns A_h, B_h, C_h, ..., and X_h ($h=1,2,3,...,l$) with l being the number of the trigonometric terms needed for convergence. Therefore, the homogeneous solution ψ_h has $24l+12$ unknowns and they will be determined according to the boundary conditions as discussed later.

6.3.2 Particular solution

For a particular solution in the series form, the transverse load $Q(X,Y)$ in Equation 6.37 is expanded to a trigonometric series as follows

$$Q(X,Y) = \sum_{j=1,2...}^{\infty} \sum_{k=1,2...}^{\infty} \frac{\cos\alpha}{ab} \int_{-b}^{b}\int_{-a}^{a} Q(\xi,\eta)\sin\frac{j\pi(\xi+a)}{2a}\sin\frac{k\pi(\eta+b)}{2b}d\xi d\eta \sin\frac{j\pi(X+a)}{2a}\sin\frac{k\pi(Y+b)}{2b}$$

....(6.43)

Equation 6.43 is able to describe a uniformly distributed load, a concentrated load, a line load, or a patch load. The HL93 lane load is a uniformly distributed load. The axle loads of HL93 design truck are concentrated loads. They are expressed in the following Equations 6.44 and 6.45, respectively.

$$Q = \sum_{j=1,3,...}^{\infty} \sum_{k=1,3,...}^{\infty} \frac{16q_0(-1)^{(j+k+2)/2}}{jk\pi^2}\cos\frac{j\pi X}{2a}\cos\frac{k\pi Y}{2b}\sin\alpha \;....................(6.44)$$

$$Q = \frac{Q_0}{ab}\sum_{j=1,2...}^{\infty}\sum_{k=1,2...}^{\infty}\sin\frac{j\pi(X_0+a)}{2a}\sin\frac{j\pi(X+a)}{2a}\sin\frac{k\pi(Y_0+b)}{2b}\sin\frac{k\pi(Y+b)}{2b}$$

......(6.45)

where q_0 is the uniformly distributed load and Q_0 is the concentrated load at a point (X_0, Y_0).

Accordingly, the particular solution ψ_p for Equation 6.45 can be written in a series form as

$$\psi_p = \sum_{j=1,2,\ldots}^{m} \sum_{k=1,2,\ldots}^{m} K_{jk} \cos\frac{j\pi(X+a)}{2a}\cos\frac{k\pi(Y+b)}{2b} + L_{jk}\sin\frac{j\pi(X+a)}{2a}\sin\frac{k\pi(Y+b)}{2b} \quad \ldots(6.46)$$

where K_{jk} and L_{jk} are to be determined to satisfy Equations 6.37 and 6.43, m is the number of the trigonometric terms needed for convergence. The general solution for ψ is derived as the sum of the homogeneous solution and the particular solution as:

$$\psi = (\psi_{hp} + \psi_{ht}) + \psi_p \quad \ldots(6.47)$$

Since no unknowns exist in the particular solution, the total number of unknowns in the general solution is still $24l+12$, as in the homogeneous solution.

6.4 Determination of unknown constants for series solution

The unknown constants in Equations 6.39 and 6.40 are to be determined using appropriate boundary conditions. These conditions are presented in this section. For bridge deck plates, the boundaries are the edges of the plate, which may be free, supported by a beam, etc. In The following derivations, the normal and tangential directions to the edge are denoted here using subscripts n and s respectively. The moments on the edges are accordingly noted using these subscripts consistent with the directions of the stresses thereby induced. For example, M_n is for the moment causing normal stresses and M_s is the torsional moment inducing shear stresses.

The following four boundary conditions are common for highway bridge decks.

(1)   Clamped: $w = 0, \phi_n = 0, \phi_s = 0$ (6.48)

(2)   Soft Simply Supported (SS1) : $w = 0, M_n = 0, \phi_s = 0$ (6.49)

(3)   Hard Simply Supported (SS2): $w = 0, M_n = 0, M_s = 0$ (6.50)

(4)   Free: $M_n = 0, M_s = 0, Q_n = 0$ (6.51)

An example of clamped condition is one created by the end diaphragm / back wall of the Woodruff Bridge, discussed earlier in Chapter 3 and shown in Figure 4.8.   The difference between the soft and hard simple supports in Equations 6.50 and 6.51 is graphically described in Figure 6.2.   The boundary condition of SS1 restricts the tangential rotation by supporting two points in the cross section, thereby generating a non-zero torsional moment. In contrast, the boundary condition of SS2 supports the plate only at one point in the cross section, allowing a tangential rotation and generating no twisting moment. Note that the Kirchhoff theory treats SS1 and SS2 in Equations 6.49 and 6.50 as the same boundary condition.   The free boundary condition can be used to describe, for example, a deck overhang cantilever.
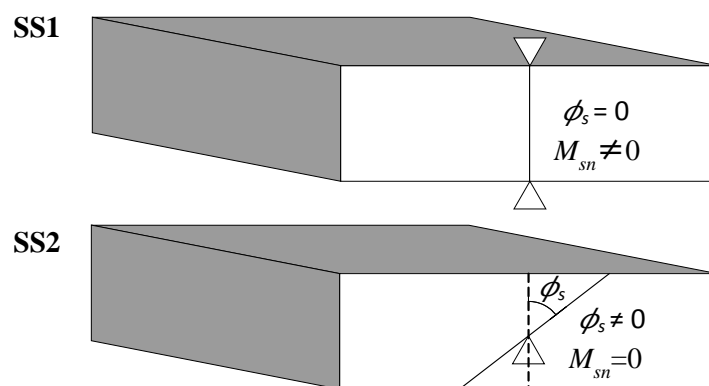

Figure 6.2 Comparison between SS1 and SS2

The boundary conditions in Equations 6.48 to 6.51 can be unified as follows:

$$\Gamma_d(X,Y) = 0 \quad \begin{cases} d = 1,2,3 & \text{(edge CD in Figure 6.1)} \\ d = 4,5,6 & \text{(edge AB in Figure 6.1)} \\ d = 7,8,9 & \text{(edge BC in Figure 6.1)} \\ d = 10,11,12 & \text{(edge AD in Figure 6.1)} \end{cases}$$

...................(6.52)

where $\Gamma_1(X,Y)$ to $\Gamma_{12}(X,Y)$ represent the left hand side of Equations 6.48 to 6.51.

$\Gamma_1(X,Y)$ to $\Gamma_{12}(X,Y)$ are expanded as Fourier series as follows for the solution method pursued in this project:

$$\Gamma_d(X,Y) = \frac{a_{0d}}{2} + \sum_{c=1}^{\infty} \left(a_{cd} \cos\left(\frac{c\pi X}{a}\right) + b_{cd} \sin\left(\frac{c\pi X}{a}\right) \right) \quad (d=1,2,...6) \text{ (for the edge of } Y = b, -b)$$

$$\Gamma_d(X,Y) = \frac{a_{0d}}{2} + \sum_{c=1}^{\infty} \left(a_{cd} \cos\left(\frac{c\pi Y}{b}\right) + b_{cd} \sin\left(\frac{c\pi Y}{b}\right) \right) \quad (d=7,8,...12) \text{ (for the edge of } X = a, -a)$$

.

....(6.53)

where coefficients a_{0d}, a_{cd}, and b_{cd} are Fourier coefficients for boundary condition $\Gamma_d(X, Y)$. Note that the number of equations can be equated to that of unknowns $24l+12$ by arranging the number of truncated terms in Equation 6.53 and this is how the analytical solution is derived in this research effort.

6.5   Application examples

In this section, two application examples are presented using the developed analytical solution for skewed thick plates. They are also compared with solutions published in the literatures and FEA result obtained using a commercial package ANSYS. In the analysis by ANSYS, 2D 4-node quadrilateral plate elements (SHELL181) applicable to thick plate analysis

144

are used for the skewed plates with various skew angles. In addition, the effect on convergence of number of terms l and m in the fundamental and particular solutions is studied. In the following examples, the shear correction factor K_s is taken as 5/6 commonly used in plate analyses (Vlachoutsis 1992, Pai 1995).

6.5.1 Isotropic skewed thick plates

For the concerned skewed thick plates, the following material and geometrical properties are used: E = 580,200 ksi (4000 kN/mm^2), v=0.3, $a = b$ = 3.94 in. (100mm), and t = 1.57 in. (40mm). The external force Q is a uniformly distributed load 1,450 ksi (10kN/mm^2) applied to the plates with skew angle α=0°, 30°, and 60°. The SS2 boundary condition in Equation 6.50 is used for all four edges.

As a first step, the numbers of terms in the series solution m and l in Equation 6.40 and 6.46 are determined. The expansion of the transverse load Q and the boundary conditions Γ_d accordingly use m and l terms respectively. To see the trend of convergence as a function of l, Figure 6.3 shows the results of the out-of-plane deflection w at the center of the plate with increasing number of terms m, for four different l values. The vertical axis shows the deflection normalized by that of l=7 and m=55, denoted as (l,m)=(7,55). As seen, the deflection w for (l,m)=(5,55) and (7,35) differ less than 0.1% from that of (l,m)=(7,55). Thus it can be concluded that the solution is already convergent while truncated at (l,m)=(7,55) and therefore l=7 and m=55 are employed in this example. Note that for different skew angles α=30° and 0°, similar results are observed.

For comparison of present analytical solution and other numerical solutions, Table 6.2 exhibits results of the proposed solution, Liew and Han's method (1997), and FEA results using ANSYS for the deflection w, maximum principal moment M_x at the center of the plate $(X,Y) =$ (0 in., 0 in.) or (0mm, 0mm). The deflection and moment are expressed in a dimensionless form as $100w_c D/Qa^4$ and $10M_c/Qa^2$ (Liew and Han 1997), where w_c and M_c are the deflection and moment at the center of the plate, D is the bending stiffness and expressed as $D = Et^3/12(1-v^2)$.
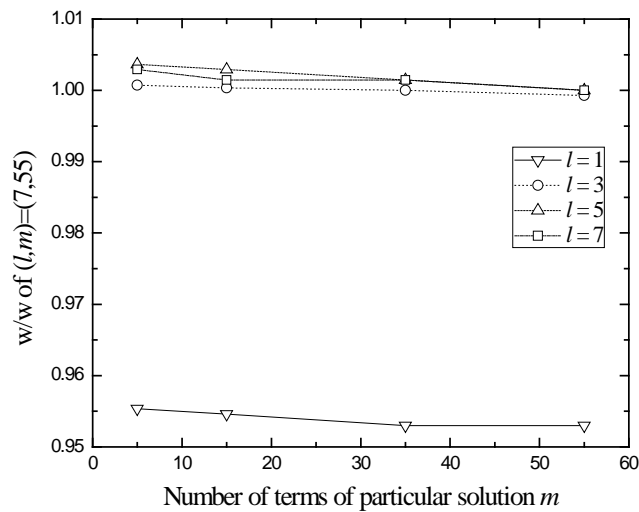

Figure 6.3 Effect of truncation in the proposed analytical solution for deflection at the center of simply supported (SS2) isotropic 30° skewed thick plates under uniform loading

Table 6.2 Comparison of proposed analytical solution and other methods

for simply supported (SS2) skewed thick plates results under uniform loading

α		$100w_cD/q_0a^4$	$10(M_c)_{max}/q_0a^2$	$10(M_c)_{min}/q_0a^2$
0°	Present	8.8686	2.1453	2.1453
	ANSYS	8.8684	2.1454	2.1454
	Liew and Han (1997)	8.8721	2.1450	2.1450
30°	Present	5.8358	1.9132	1.5130
	ANSYS	5.8327	1.9121	1.5122
	Liew and Han (1997)	5.8319	1.9110	1.5108
60°	Present	1.1717	0.8615	0.4891
	ANSYS	1.1711	0.8601	0.4888
	Liew and Han (1997)	1.1692	0.8567	0.4885

Figures 6.4 to 6.7 display comparisons between the present method and finite element method (FEM) analysis using ANSYS for the deflection w and strains ε_x, ε_y, and ε_{xy} defined in Equation (6.54), along line EF in Figure 6.1 and on the top of the plate.

$$\begin{Bmatrix} \varepsilon_x \\ \varepsilon_y \\ \varepsilon_{xy} \end{Bmatrix} = \frac{t}{2} \begin{Bmatrix} \dfrac{\partial \phi_x}{\partial x} \\[2mm] \dfrac{\partial \phi_y}{\partial y} \\[2mm] \dfrac{\partial \phi_x}{\partial y} + \dfrac{\partial \phi_y}{\partial x} \end{Bmatrix} \quad\text{...(6.54)}$$
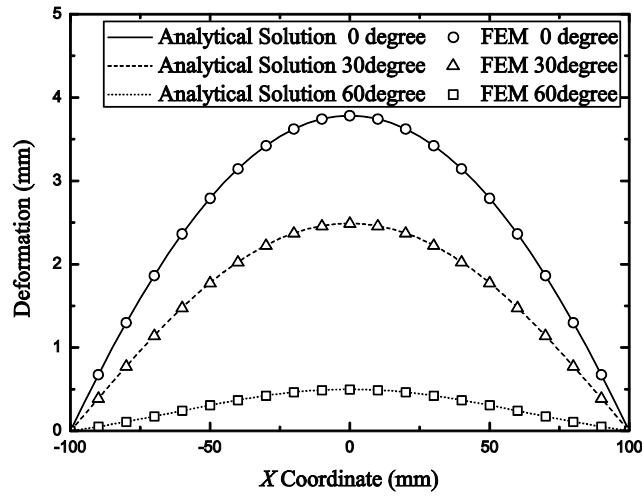
Figure 6.4 Analytical and FEM results for deflection of simply supported (SS2) isotropic skewed
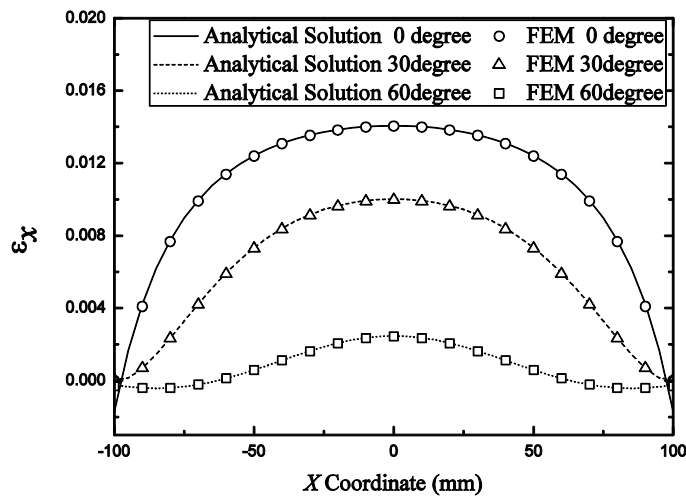
thick plate bending under uniform loading

Figure 6.5 Analytical and FEM results of x-direction strain of simply supported (SS2) isotropic

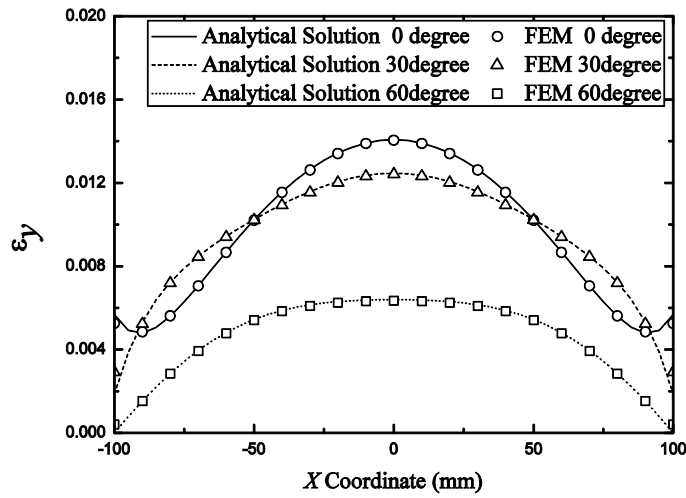skewed thick plate bending under uniform loading

148

Figure 6.6 Analytical and FEM results of *y*-direction strain of simply supported (SS2) isotropic

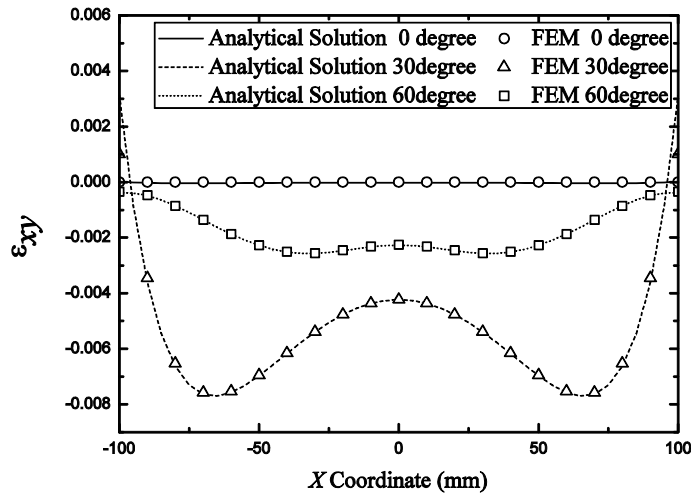skewed thick plate bending under uniform loading

Figure 6.7 Analytical and FEM results of *xy*-direction shear strain of simply supported (SS2)

isotropic skewed thick plate bending under uniform loading

The results show that the analytical and the numerical solutions agree with each other well for these isotropic thick skewed plates under the uniformly distributed load. In Figure 6.4, the deflection w is seen to be decreasing as the skew angle increases. This is apparently due to the reduction in the shortest distance from the loading location to the nearest support. Normal strains ε_x and ε_y displayed in Figures 6.5 and 6.6 also behave similarly due to the same reason. However, shear strain ε_{xy} in Figure 6.7 is due to torsion and does not change with skew angle monotonically.

When a plate is skewed, the direction of principal stress and moment is different from the x and y axes. This causes torsion and ε_{xy} in the plate. This relation is not monotonic and depends on the relative relations of the plate's skew angle, width/length ratio, loading position, boundary conditions, etc.

6.5.2 Orthotropic skewed thick plates

Orthotropic thick skewed plates are demonstrated in this example, with the following material and geometrical properties: E_x = 580,200 ksi (4000 kN/mm^2), E_y = 290,100 ksi (2000 kN/mm^2), G_{xy} = 174,060 ksi (1200 kN/mm^2), G_{xz} = 145,050 ksi (1000 kN/mm^2), G_{yz}= 116 ,040 ksi (800 kN/mm^2), v_{xy}=0.2, $a = b$ = 3.94 in. (100 mm), t = 0.79 in. (20 mm), where E_x and E_y are Young's modulus along the x and y directions, and G_{xy}, G_{xz}, and G_{yz} are shear modulus in the xy, xz, and yz planes. These values determine $[D_r]$, $[D_o]$, $[A_r]$, and $[A_o]$ in Equations 6.16 and 6.20. The external transverse force is a concentrated force of 1,450 ksi (10 kN) applied at (X, Y) = (-1.97 in., 1.97 in.) or (-50mm, 50mm). Plates with skew angle α=0°, 30° and 60° are analyzed

here. Edges *AB* and *CD* are simply supported (SS1) and Edges *BC* and *DA* are clamped. The case is therefore referred to as an CCSS boundary condition.

As the previous example, the number of terms include *l* and *m* in Equations 6.40 and 6.46 need to be determined first. Figure 6.8 shows the deflection *w* at the center of the plate $(X,Y) = (0$ in., 0 in.) or (0 mm,0 mm) for skew angle α=60°, as one of the cases considered, for various *l* and *m* values. It is seen that the deflection at $(l,m)=(7,75)$ is well converged. Therefore $(l,m)=(7,75)$ is employed here and also used as the reference for comparison.
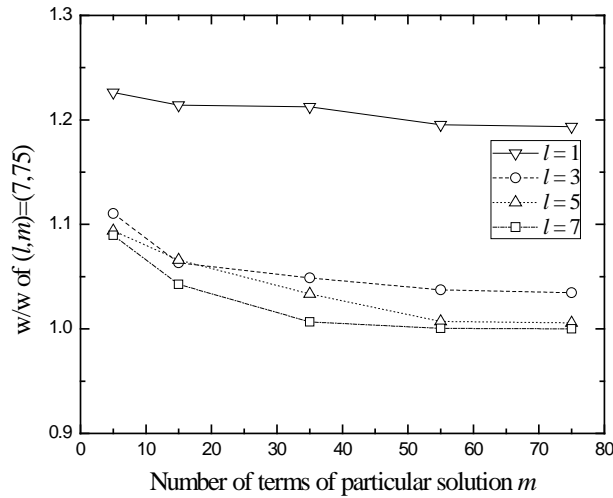

Figure 6.8 Convergence of deflection at the center of CCSS orthotropic skewed thick plates under concentrated loading.

For this example, because no previous work in the literature has been found reporting similar experience, only FEM analysis results are employed for comparison with our analytical solution results. Figures 6.9 to 6.12 show comparisons of the deflection *w* and strains ε_x, ε_y, and

ε_{xy} defined in Equation 6.54 along the line *HF* in Figure 6.1. It is seen that the proposed analytical solutions and the numerical solutions agree with each other very well.
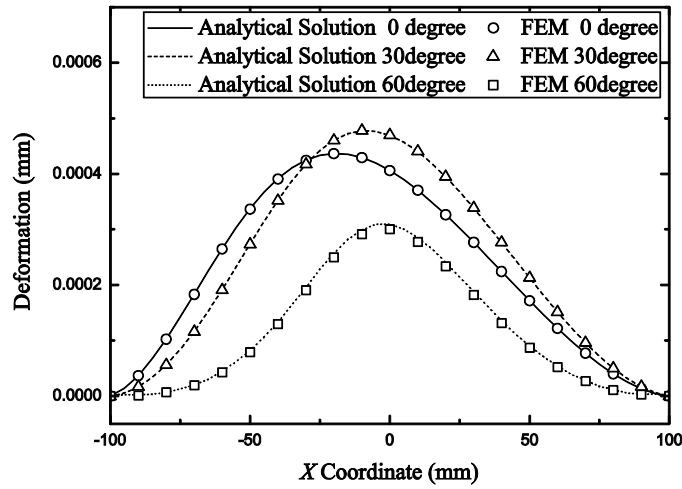
Figure 6.9 Analytical and FEM results of Deflection of CCSS orthotropic skewed thick plate

bending under concentrated loading

Figure 6.10 Analytical and FEM results of *x*-direction strain of CCSS orthotropic skewed thick
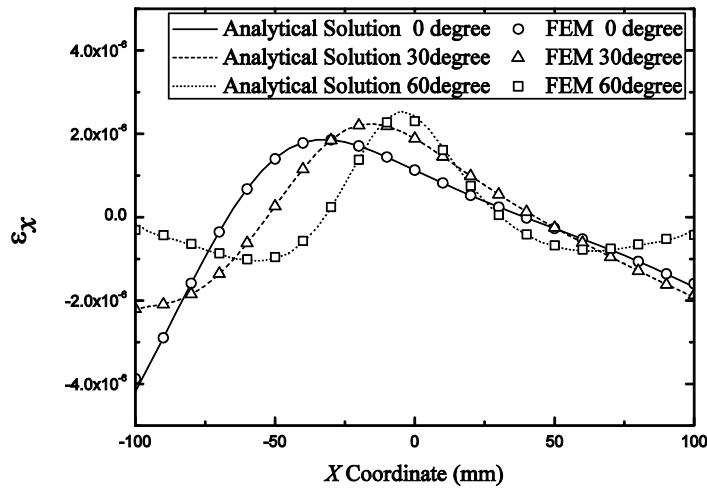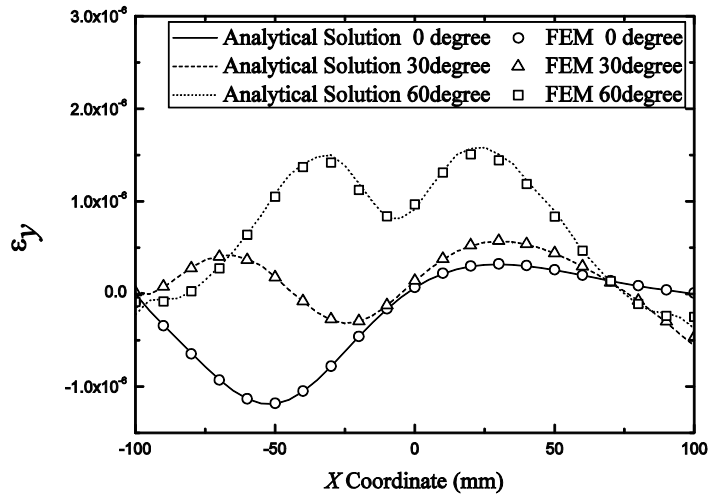
plate bending under concentrated loading

Figure 6.11 Analytical and FEM results of *y*-direction strain of CCSS orthotropic skewed thick

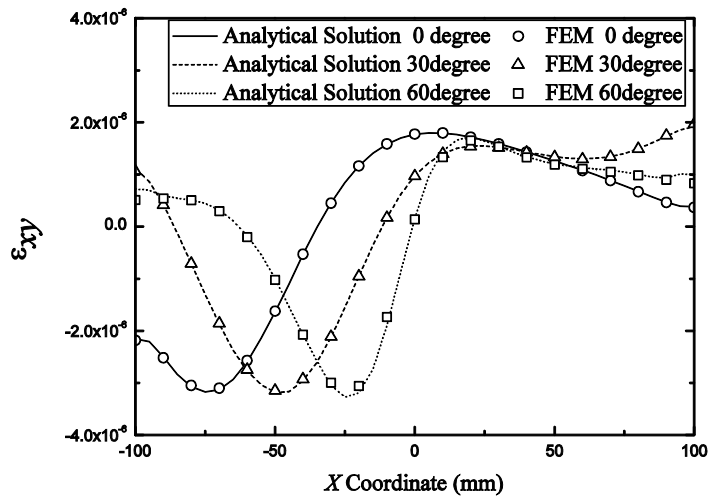plate bending under concentrated loading

Figure 6.12 Analytical and FEM results of *xy*-direction shear strain of CCSS orthotropic skewed

thick plate bending under concentrated loading

The results shown in Figures 6.9 to 6.12 indicate that the response behavior for this case is much more complex than the previous example, due to non-symmetric loading and boundary conditions. These response quantities are read at $Y=0$ in. (0mm). Due to the oblique coordinate system, the load at $(X,Y)=$ (-1.97 in., 1.97 in.) or (-50mm, 50mm) has different relative relations with the interested responses on $Y=0$ in. (0 mm), depending on skew angle. This causes the peak responses in Figures 6.9 to 6.12 to move towards $X=0$ mm with skew angle increasing from 0° to 60°. This behavior is more pronounced in the shear strain ε_{xy} than deflection w and the other two strains ε_x and ε_y.

6.6   Summary

The governing differential equation of skewed thick plates in an oblique coordinate system is formulated for the first time in this research project. It allows derivation of the analytical solution for any boundary conditions and loading conditions. All response quantities including shear forces, moments, stresses, strains, deflections, and rotation angles can be readily derived from the proposed potential function solution ψ. The two illustrative examples show that the analytical solutions are in good agreement with those reported in the literature and numerical solutions by FEA.

This analytical solution method can be readily extended to skewed beam bridges by assembling several skewed plates into the bridge system using appropriate boundary conditions. Such solutions can be readily computerized for routine design application. This approach will be much more user friendly than the FEA approach since there will be no need for mesh related data input, such as element type, element size, element aspect ratio, etc.

155

Chapter 7

Recommended Design Guidelines

The previous chapters have presented the research approaches and findings in this project. The acquired knowledge is important for understanding the behavior of typical Michigan skewed bridges. Accordingly, the following design guidelines are developed and recommended for routine design of typical skewed bridges in Michigan.

(1) The AASHO LRFD Bridge Design Specifications' moment distribution factor overestimates the design moment for interior beams in skewed beam bridges. A modification factor is developed below to account for this effect in routine design.

(2) The AASHTO LRFD Bridge Design Specifications' shear distribution factor may underestimate the design shear for fascia beams in skewed beam bridges. When such a case occurs, the design will be inadequate. A separate modification factor is developed below and recommended to be applied in routine design to account for this effect.

(3) Effects due to the AASHTO LRFD Bridge Design Specifications' temperature loads can be significant in typical Michigan skewed highway bridges, and they should not be neglected especially when thermal stresses superimpose on to maximum live load stresses.

(4) Warping and torsional effects in typical Michigan skewed bridges are small and can be neglected when designing typical short and medium spans. This conclusion is based on the

types and span ranges of bridge structure studied herein, which represent a significant majority of new Michigan highway bridges.

(5) The AASHTO distribution-factor analysis method is recommended to be extended beyond the MDOT current policy of 30° skew angle limit for refined analysis to at least 50° studied herein, provided that the modification factor C be applied, as recommended in (2) above, to unconservative design shear prediction and if the structure type, span length, beam spacing, and skew angle are within the ranges of the analyzed spans covered in this report (and thus within the applicable ranges of the AASHTO LRFD Bridge Design Specifications' distribution factors.)

7.1   Concept of modification factor

As seen in Chapter 5, the AASHTO specified load distribution factors overestimate the design moment for the interior beams and also may underestimate the design shear for the fascia beams in skewed structures analyzed using the calibrated FEA modeling approach. Accordingly, a modification factor C is developed below to account for these observed deviations. It is defined as follows

$$DF_{FEM} = C\,DF_{AASHTO} \qquad (7.1)$$

where DF_{FEM} and DF_{AASHTO} are the distribution factor for moment or shear by FEA and the AASHTO LRFD specifications, respectively. Application of this modification factor on the AASHTO distribution factor can reach the level of prediction of the detailed FEA reported

herein, as shown in Equation 7.1. *C* is above 1 when the AASHTO specifications underestimate the load effect, and *C* is below 1 when the AASHTO specifications overestimate. It is thereby recommended that when *C* is above 1, it be applied to produce a more conservative design.

7.2   Modification factor for moment

In this section, the modification factor *C* for the AASHTO moment distribution factor is discussed and presented. Section 7.2.1 is devoted to the modification factor for steel girder bridges and 7.2.2 for prestressed concrete I-girder bridges. For both types of bridge spans, the following three boundary conditions are considered, (1) simply supported end, (2) fixed end, and (3) bearing supported end.

7.2.1 Steel girder bridges

The modification factor *C* for the AASHTO moment distribution factor of the steel girder bridge are derived using regression of the FEA results into the following equations

$$C = 1.11 - 0.00022L - 0.028S - \frac{0.91\tan\theta}{L^{0.67}S^{0.25}} \tag{7.2}$$

$$C = 0.345 + 0.00027L + 0.00475S + \frac{2.65S^3\tan\theta}{L^{2.5}} \tag{7.3}$$

$$C = 1.05 + 0.00024L - 0.024S + \frac{1.1\tan\theta}{L^{0.26}S^{1.04}} \tag{7.4}$$

158

where S is the beam spacing (ft), L is span length (ft), and θ is the skew angle in degree. The applicable ranges of above equations are $6.0 \leq S \leq 10.0$, $120 \leq L \leq 180$, and $0° \leq \theta \leq 50°$. Equations 7.2, 7.3, and 7.4 are respectively for the boundary conditions of (1) simply supported end, (2) fixed end, and (3) bearing supported end. These functions are developed using a regression analysis of the FEA results. The coefficients of determination R^2 are respectively 0.908, 0.962, and 0.892. As an alternative way of expressing Equations 7.2 to 7.4, Figures 7.1 to 7.9 show contour plots of the modification factors C for L, S, and θ within the given ranges. These figures show the curves on which the C value is constant for the specified skew angle θ. The C values are noted on these curves. For example, Figure 7.1 shows C value contours between C=0.9 and 0.8 for moment in steel beams of a straight bridge with $0°$ skew angle.
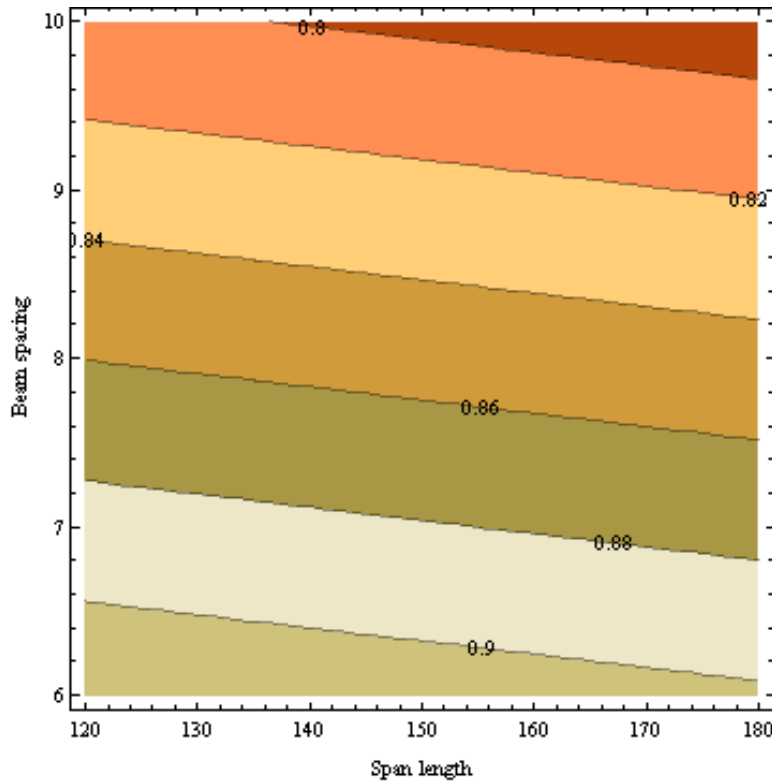

Figure 7.1 Contour of modification factor C for moment in steel girder bridges
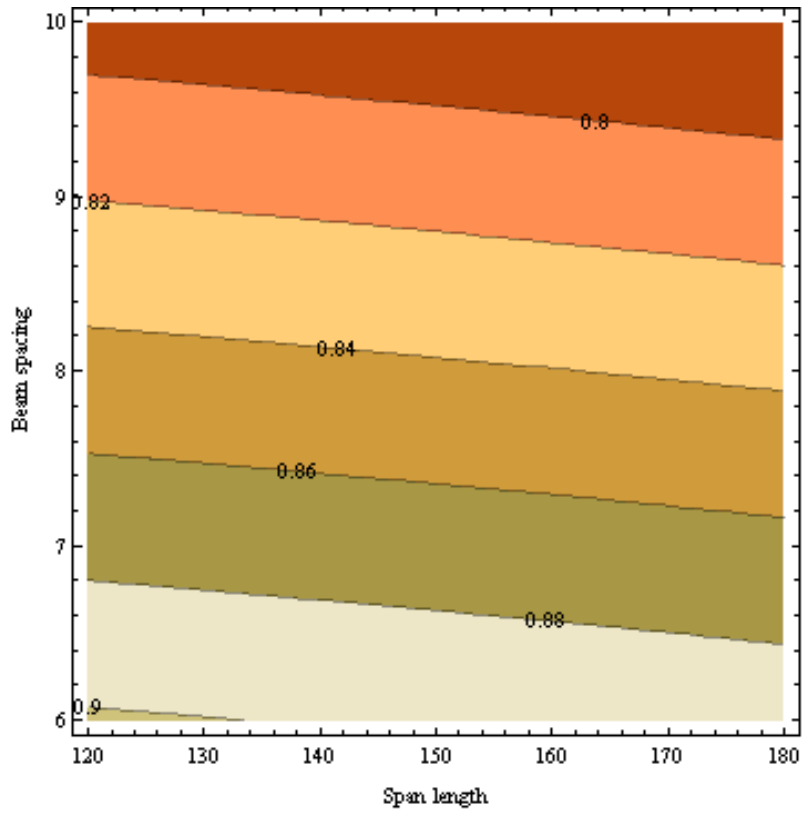
Figure 7.2 Contour of modification factor *C* for moment in steel girder bridges

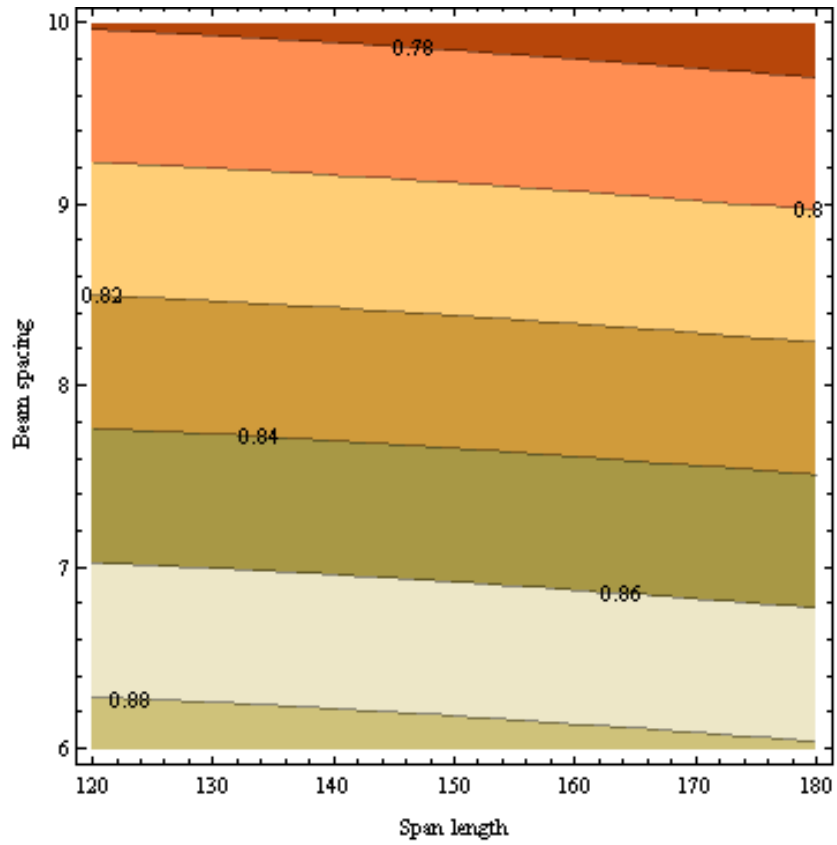(end condition: simple support, skew angle = 30°)

Figure 7.3 Contour of modification factor *C* for moment in steel girder bridges

(end condition: simple support, skew angle = 50°)

Figure 7.4 Contour of modification factor *C* for moment in steel girder bridges

(end condition: fix support, skew angle = 0°)

Figure 7.5 Contour of modification factor *C* for moment in steel girder bridges
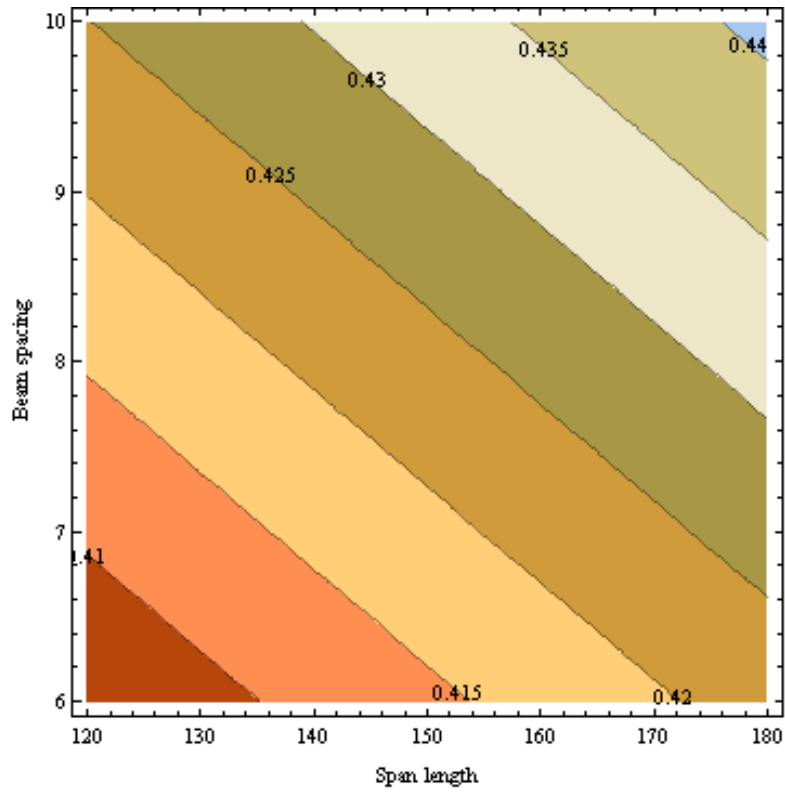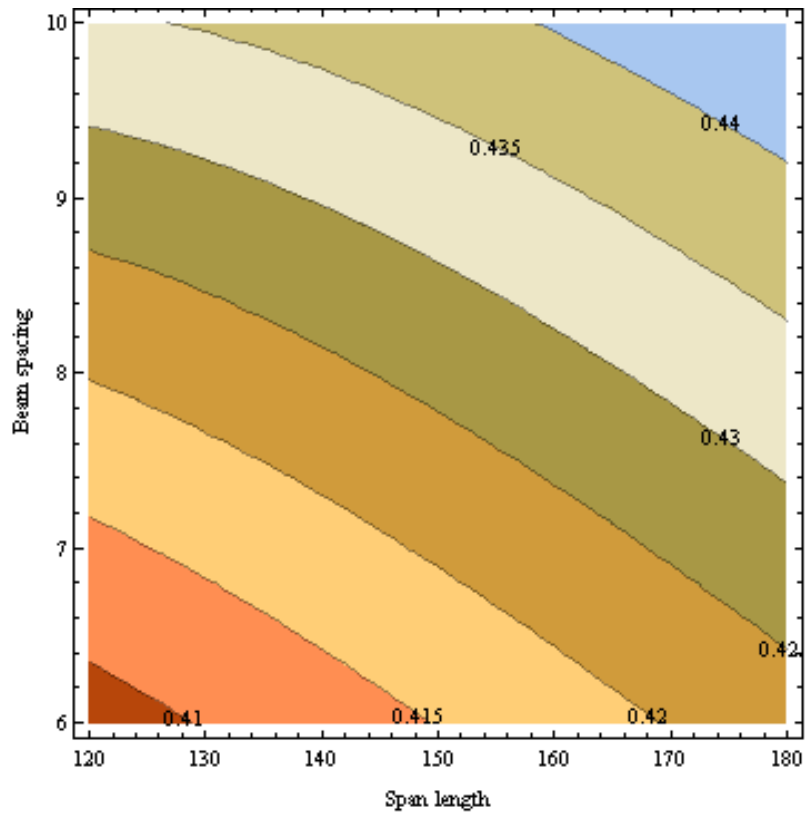
(end condition: fix support, skew angle = 30°)
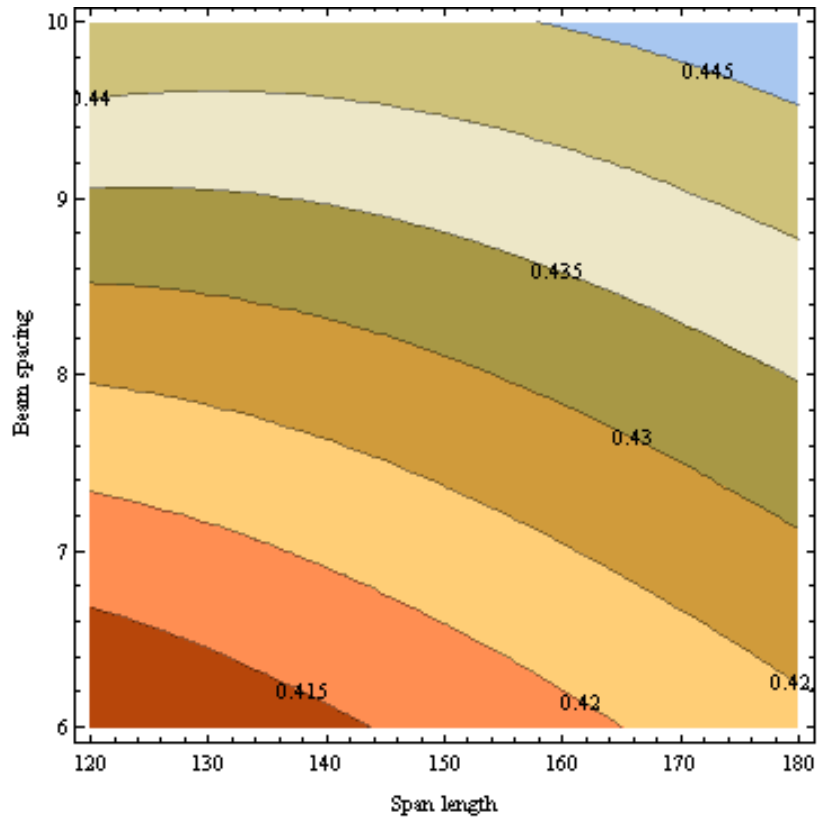
Figure 7.6 Contour of modification factor *C* for moment in steel girder bridges

(end condition: fix support, skew angle = 50°)

Figure 7.7 Contour of modification factor *C* for moment in steel girder bridges

(end condition: bearing support, skew angle = 0°)

Figure 7.8 Contour of modification factor *C* for moment in steel girder bridges

(end condition: bearing support, skew angle = 30°)

Figure 7.9 Contour of modification factor *C* for moment in steel girder bridges

(end condition: bearing support, skew angle = 50°)
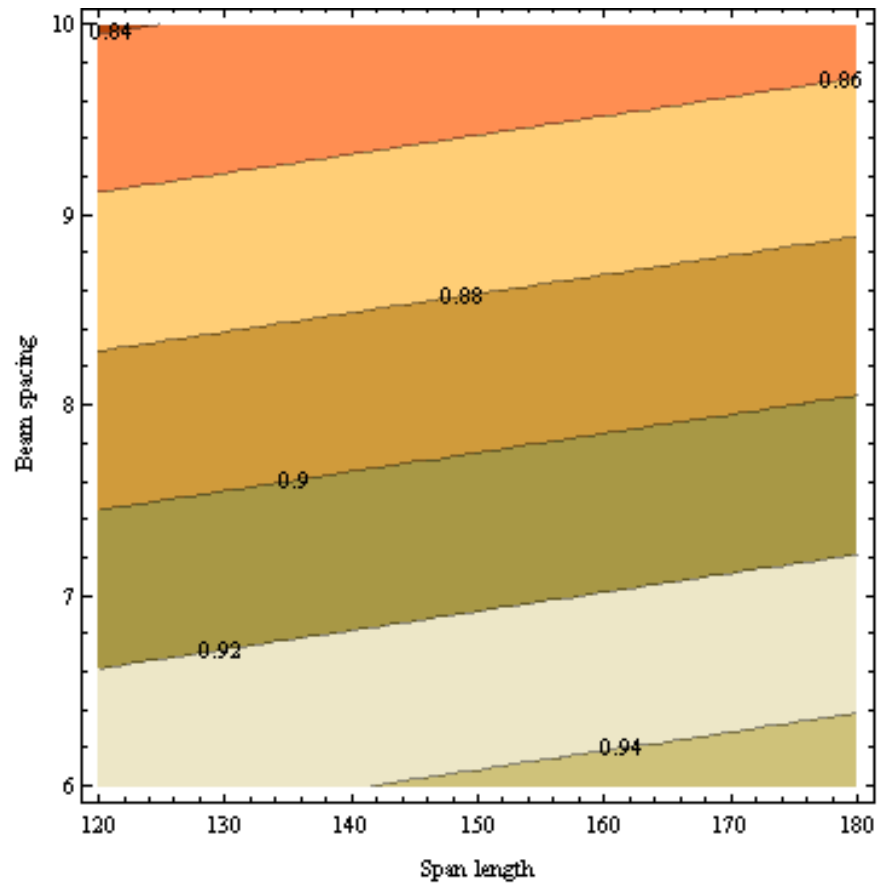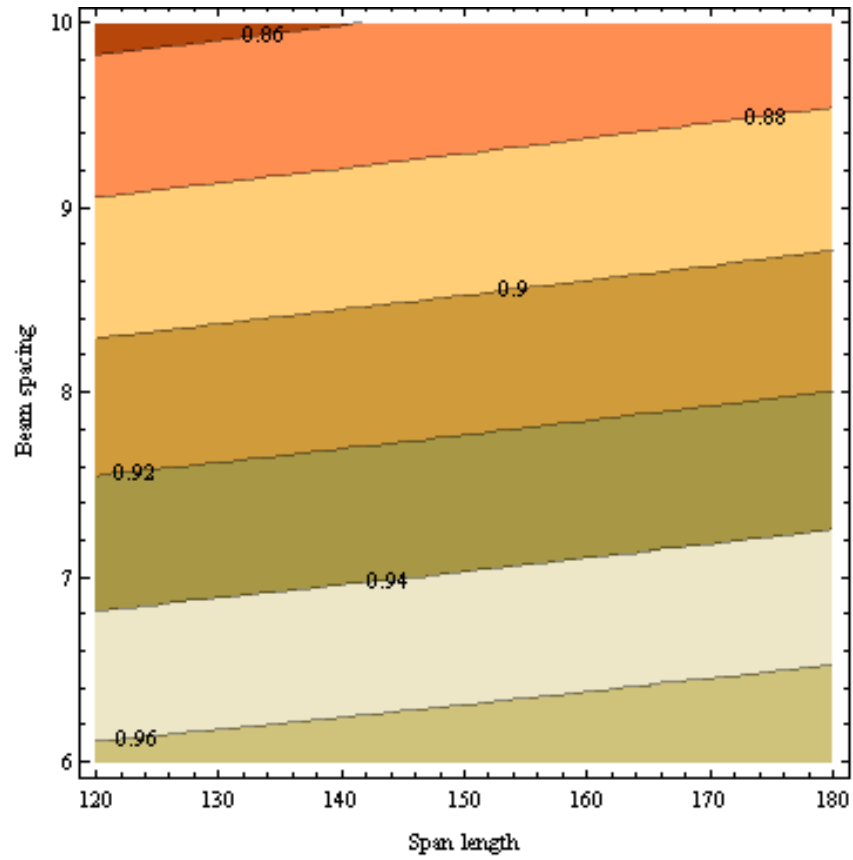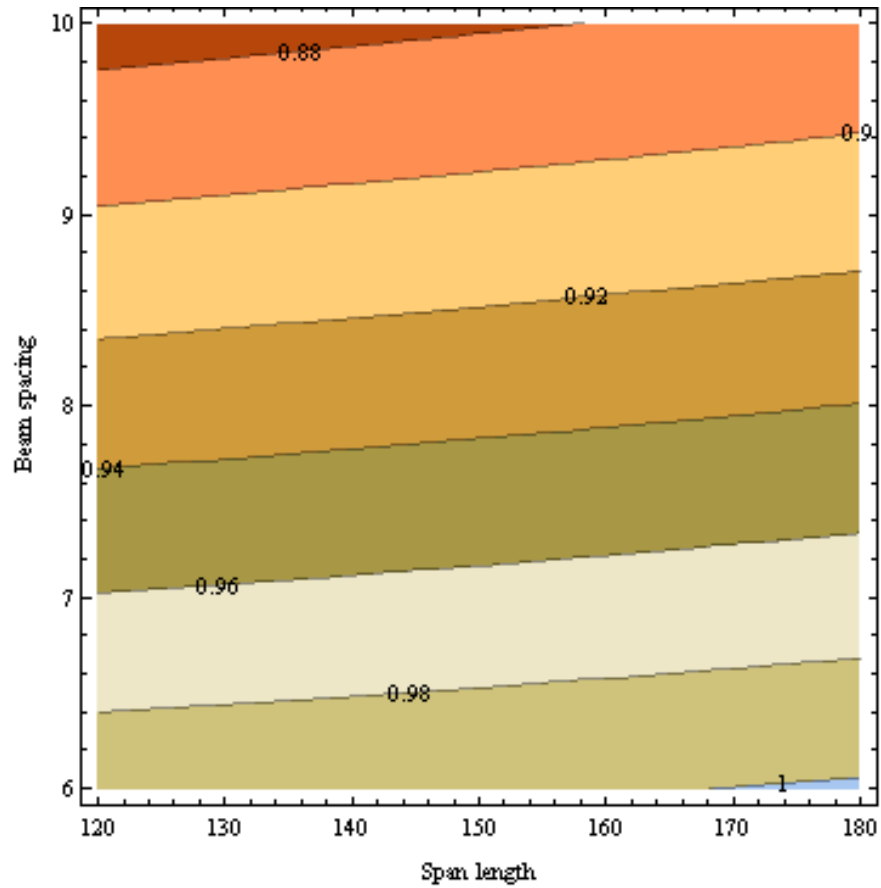
As seen in Equations 7.2 to 7.4 and Figures 7.1 to 7.9, modification factor *C* for moment does not go beyond 1 in the applicable ranges. This indicates that the AASHTO LRFD design code overestimates moment and is conservative.

7.2.2 Prestressed concrete I-girder bridges

The modification factor C for the AASHTO moment distribution factor of the prestressed concrete girder bridge is also derived for the three boundary conditions in the following set of equations

$$C = 0.76 + 0.0009L + 0.003L^{0.5}\tan\theta \qquad (7.4)$$

$$C = 0.35 + 0.0004L + 0.0006L^{0.7}\tan\theta \qquad (7.5)$$

$$C = 0.8 + 0.0011L + \frac{1.05\tan\theta}{L^{0.64}} \qquad (7.6)$$

Figure 7.10 Contour of modification factor C for moment in prestressed concrete girder bridges

(end condition: simple support)

where L is span of beam (ft), θ is the skew angle in degree. The applicable ranges of above equation are $60 \leq L \leq 120$, $0° \leq \theta \leq 50°$. Equations 7.4 to 7.6 are for the boundary conditions of (1) simply supported end, (2) fixed end, and (3) bearing supported end, respectively. Figures 7.10 to 7.12 show the contour plots of modification factor C with L and θ within the applicable ranges.

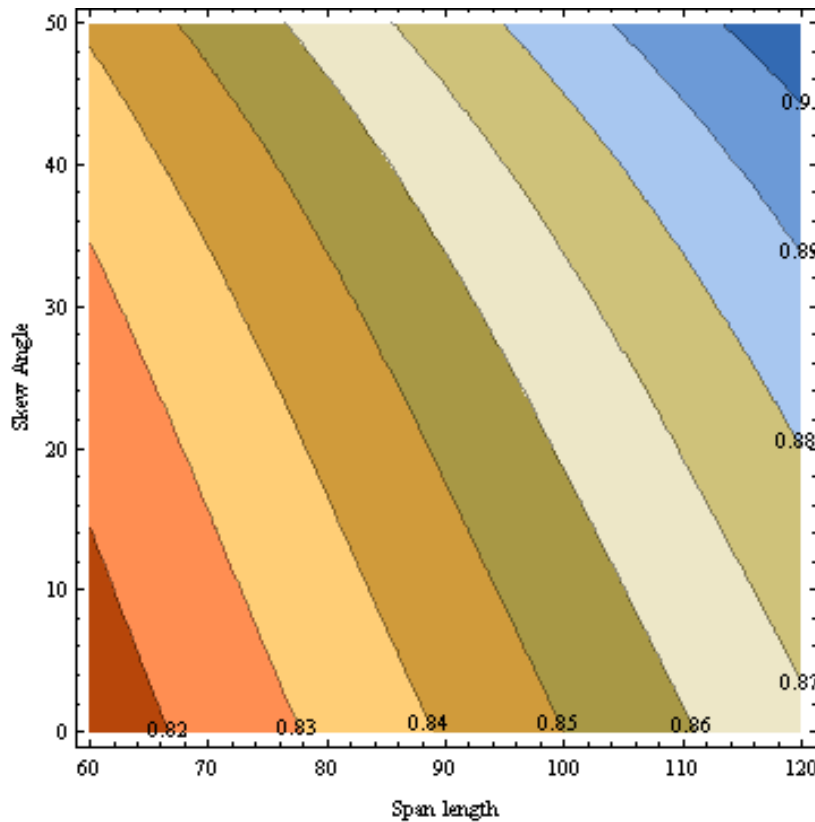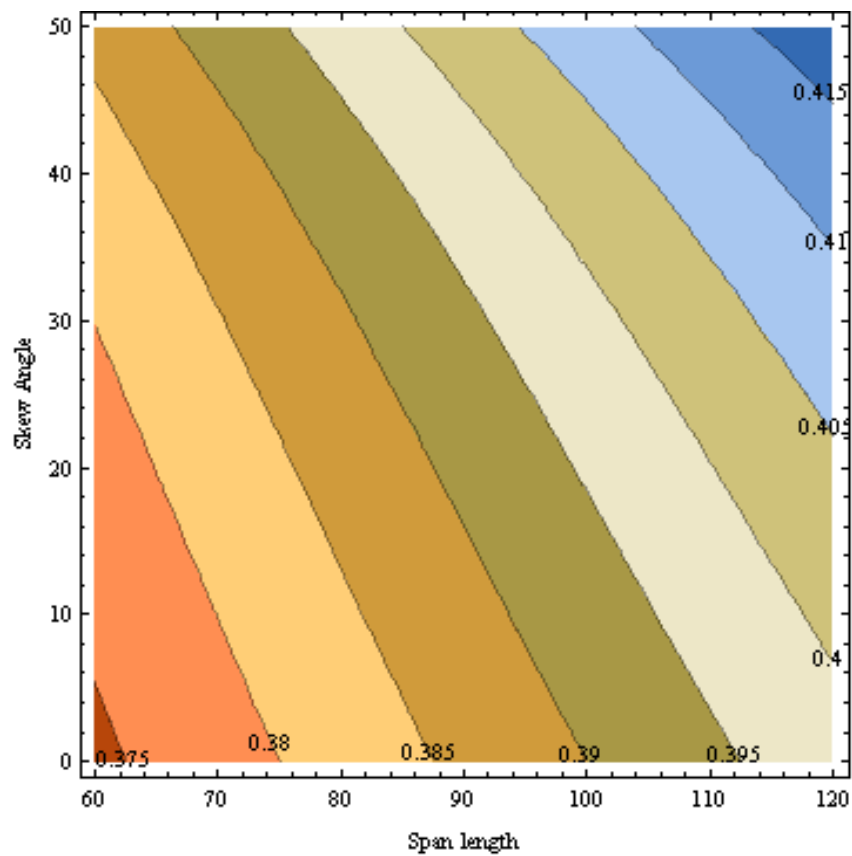
Figure 7.11 Contour of modification factor C for moment in prestressed concrete girder bridges

(end condition: fix support)
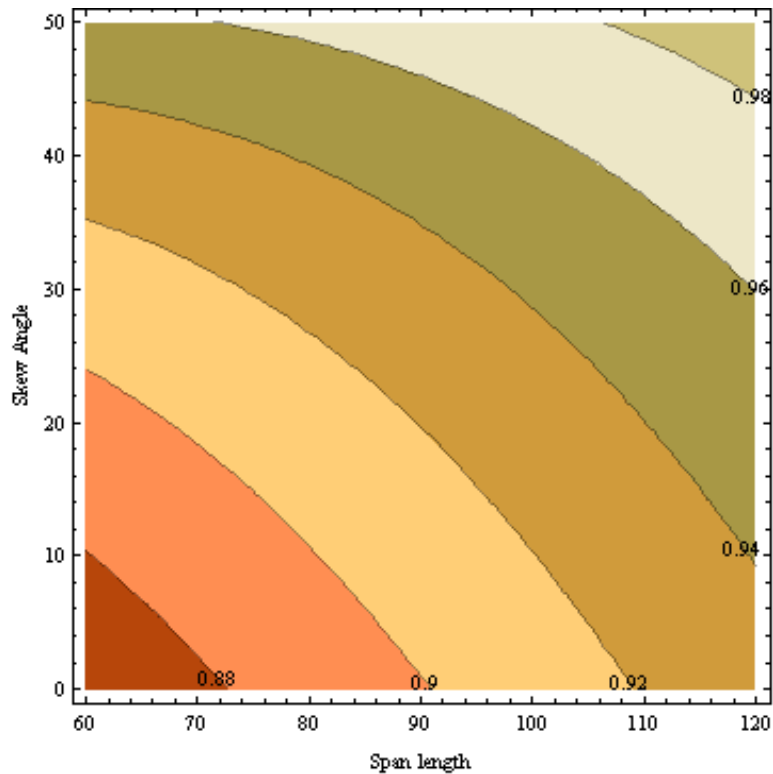
Figure 7.12 Contour of modification factor *C* for moment in prestressed concrete girder bridges

(end condition: bearing support)

Again the modification factor values are all below 1, as is the case for typical Michigan skewed steel girder bridges. This means that the AASHTO LRFD design code is conservative.

7.3 Modification factor for shear

In this section, modification factor *C* for the AASHTO shear distribution factor at the obtuse corner is derived. As done in the previous section, typical skewed Michigan steel and prestressed concrete girder bridges are addressed. Section 7.3.1 below has a focus on the modification factor for the steel girder bridges and 7.3.2. for the prestressed concrete girder

bridges. For both types of bridges, three kinds of boundary conditions are considered as in the previous section.

7.3.1 Steel girder bridges

The modification factors C for the shear distribution factor of the steel girder bridge at the obtuse corner are derived as shown in the following equations

$$C = 1.173 + 0.0001L - 0.031S + \frac{0.000066L^{1.75}\tan\theta}{S^{0.6}} \tag{7.8}$$

$$C = 1.11 + 0.00022L - 0.032S + \frac{0.000065L^{1.6}\tan\theta}{S^{0.175}} \tag{7.9}$$

$$C = 1.28 + 0.00027L - 0.038S - \frac{0.22\tan\theta}{L^{0.05}S^{0.13}} \tag{7.10}$$

where S is the beam spacing (ft), L is the span length (ft), θ is the skew angle in degree. The applicable ranges of the above equation are $6.0 \leq S \leq 10.0$, $120 \leq L \leq 180$, $0° \leq \theta \leq 50°$. Equations 7.8 to 7.10 are for the boundary conditions of (1) simply supported end, (2) fixed end, and (3) bearing supported end, respectively. Figures 7.13 to 3.21 below show the contour plots of modification factor C when L, S, and θ vary within the applicable ranges. These functions are developed based on regression using the corresponding FEA results for the typical Michigan skewed bridge spans, with the coefficient of determination R^2 at 0.897, 0.883, 0.935, respectively.

Figure 7.13 Contour of modification factor *C* for shear in steel girder bridges

(end condition: simple support, skew angle = 0°)

Figure 7.14 Contour of modification factor *C* for shear in steel girder bridges

(end condition: simple support, skew angle = 30°)

Figure 7.15 Contour of modification factor *C* for shear in steel girder bridges

(end condition: simple support, skew angle = 50°)

Figure 7.16 Contour of modification factor *C* for shear in steel girder bridges

(end condition: fix support, skew angle = 0°)
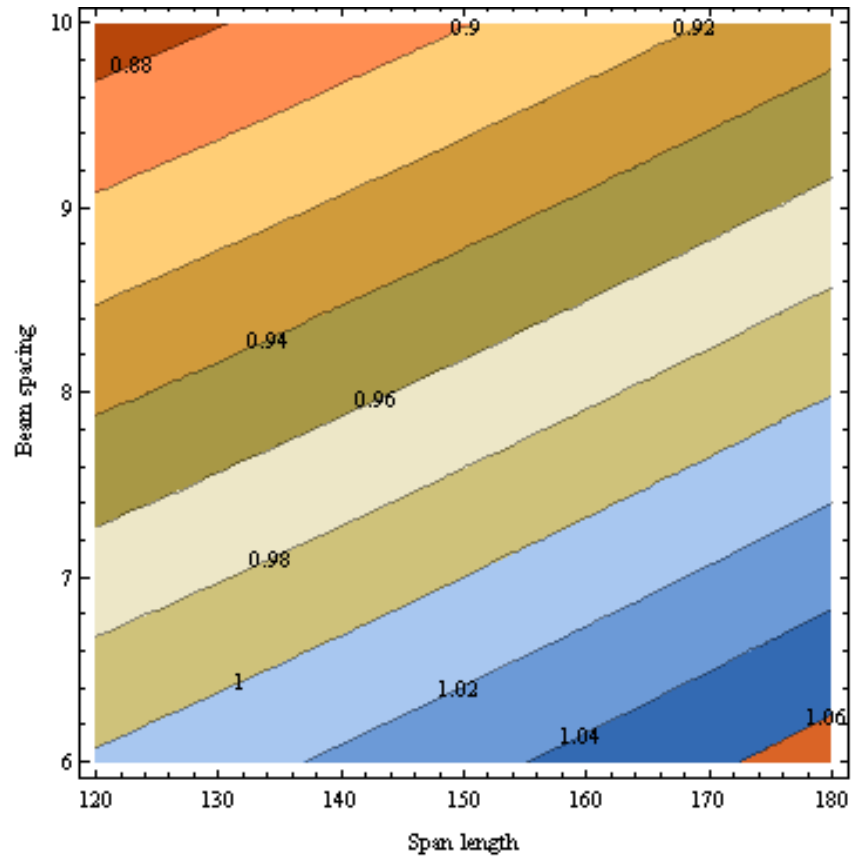
Figure 7.17 Contour of modification factor *C* for maximum shear in steel girder bridges

(end condition: fix support, skew angle = 30°)
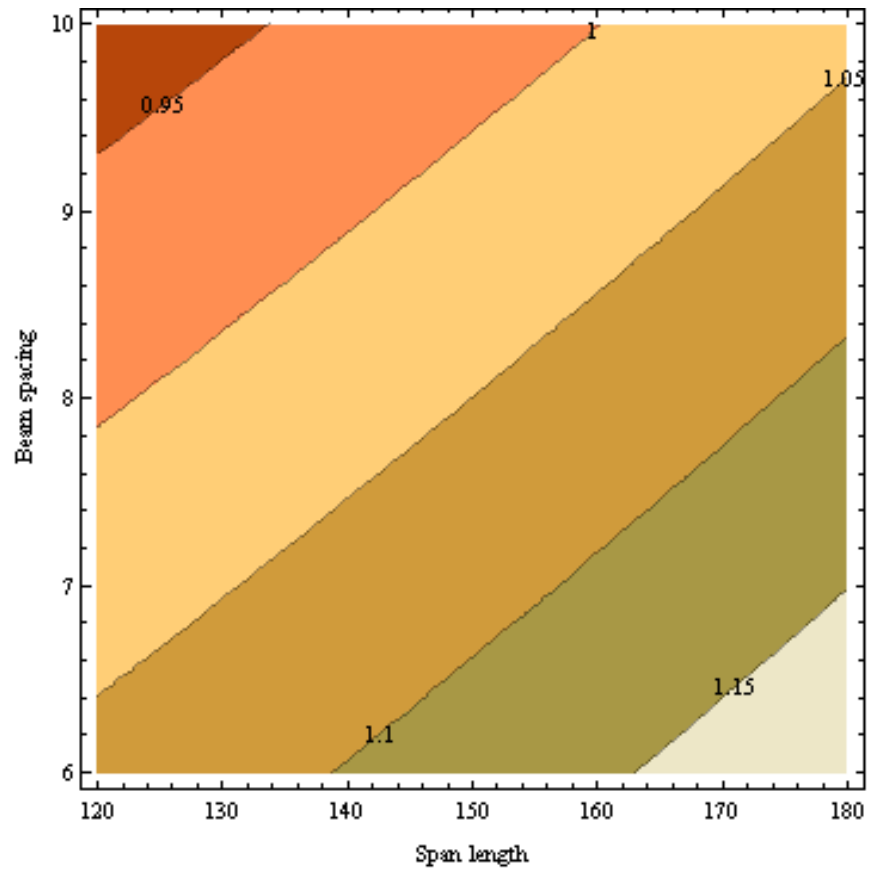
Figure 7.18 Contour of modification factor *C* for maximum shear in steel girder bridges

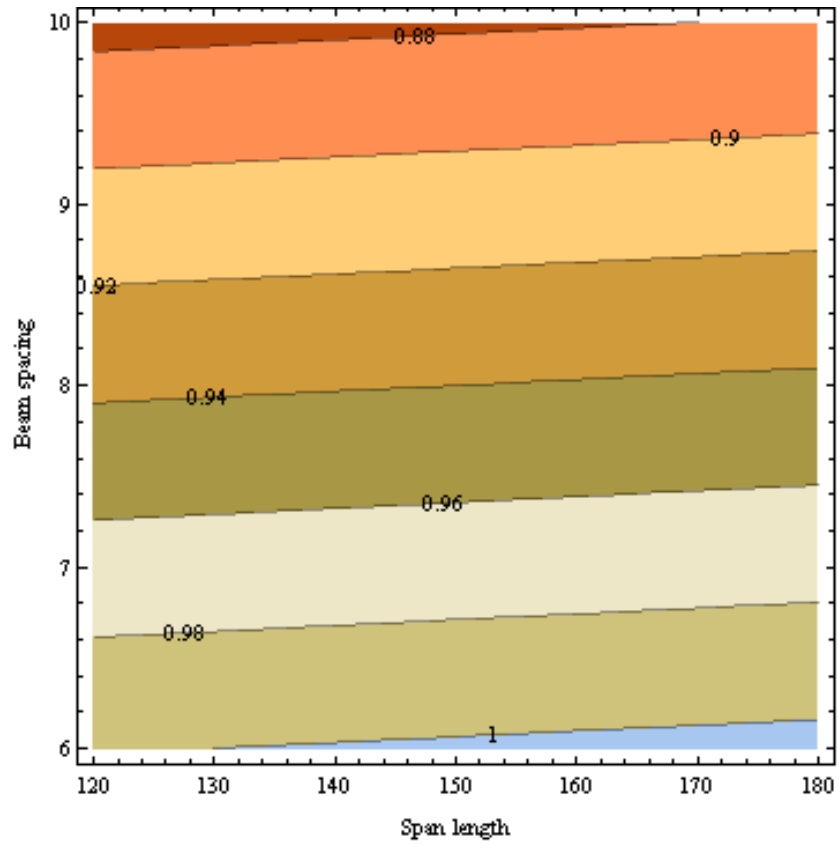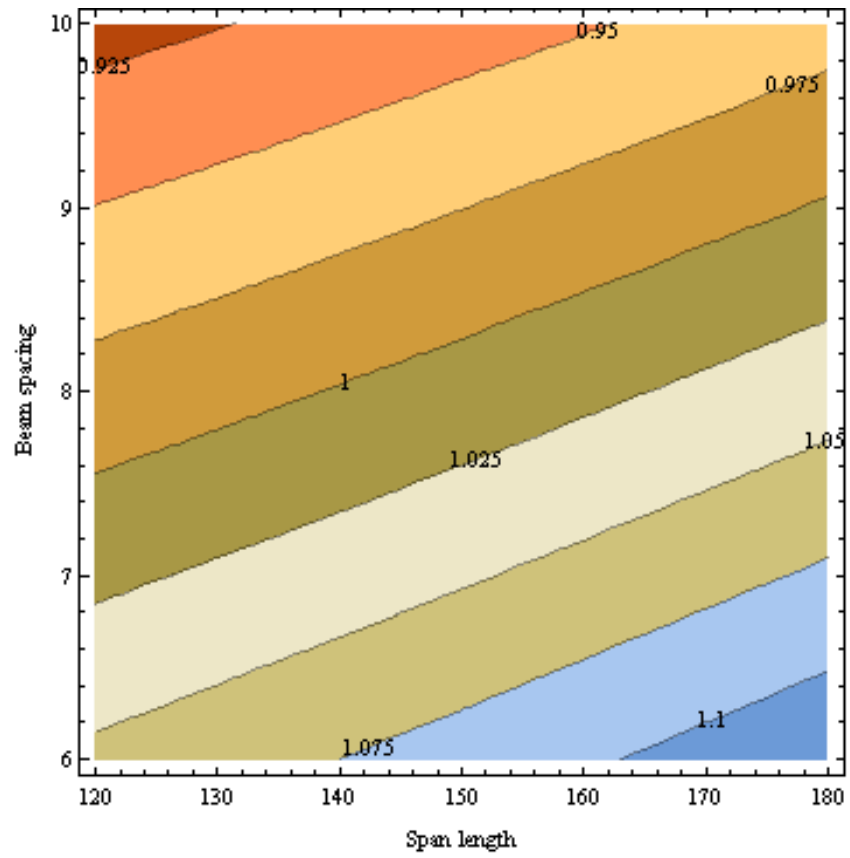(end condition: fix support, skew angle = 50°)
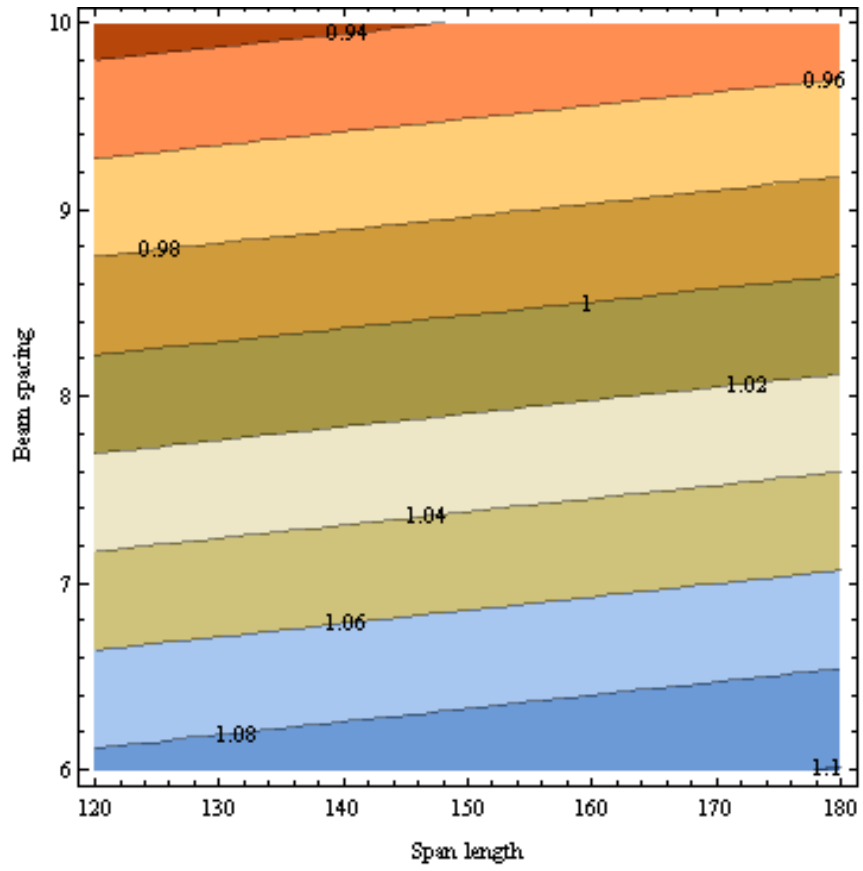
Figure 7.19 Contour of modification factor *C* for shear in steel girder bridges

(end condition: bearing support, skew angle = 0°)
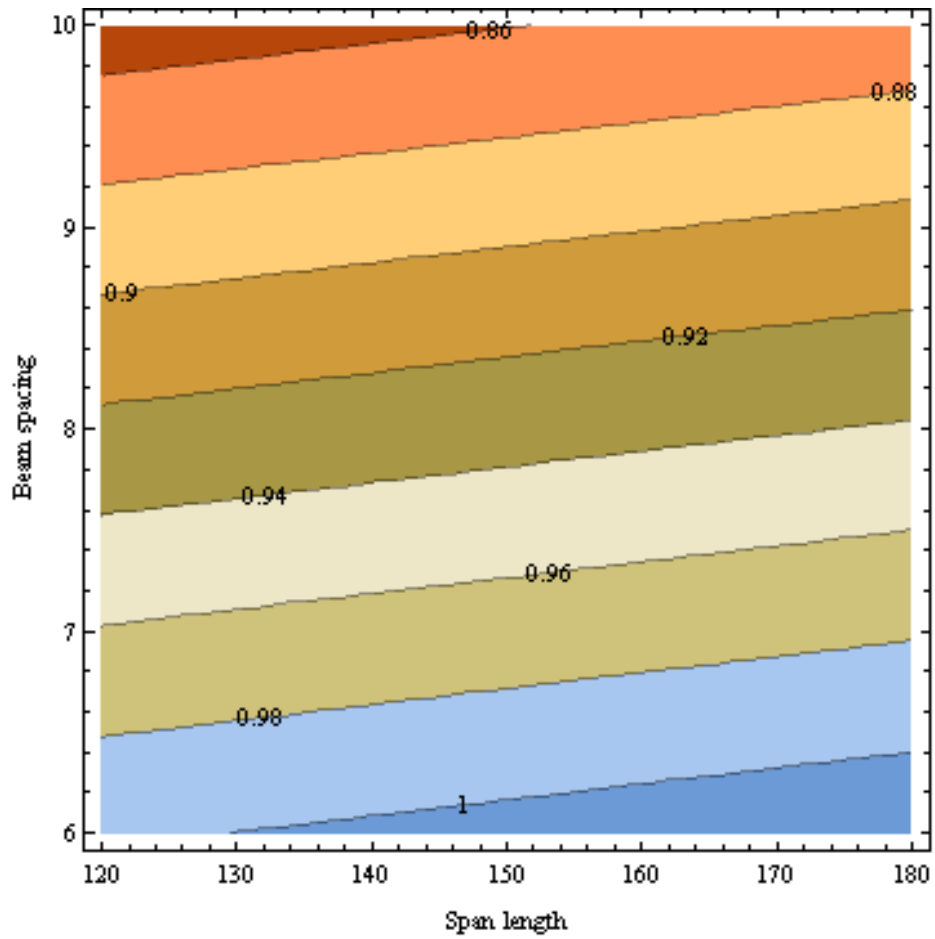
Figure 7.20 Contour of modification factor *C* for shear in steel girder bridges

(end condition: bearing support, skew angle = 30°)
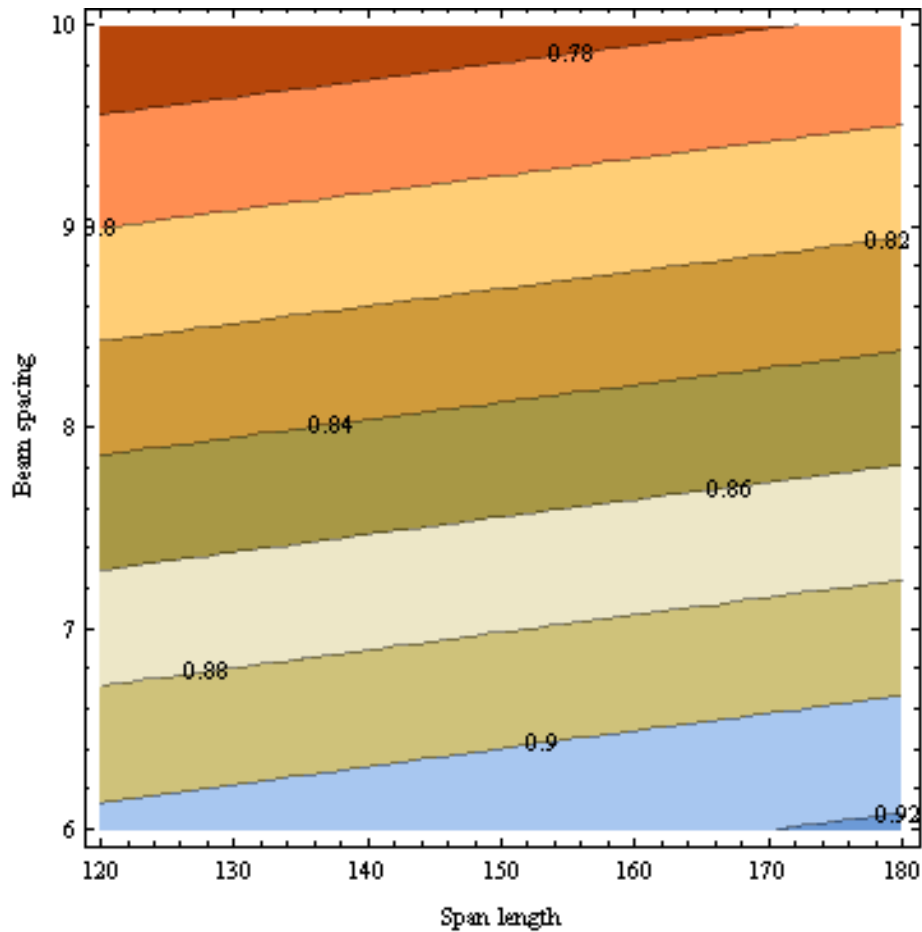
Figure 7.21 Contour of modification factor *C* for shear in steel girder bridges
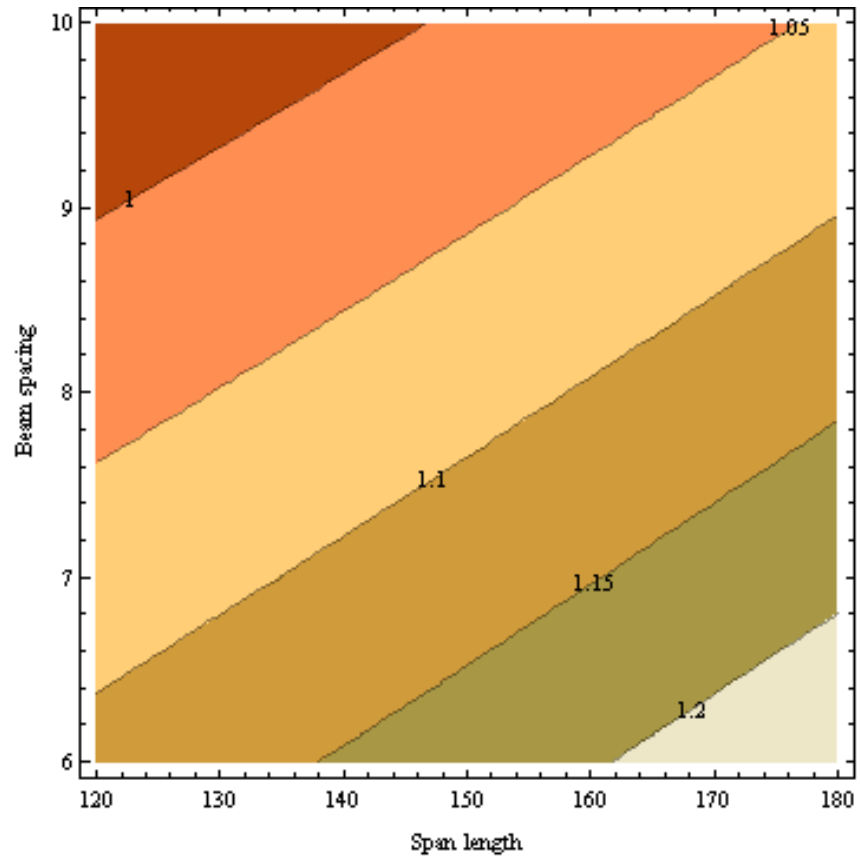
(end condition: bearing support, skew angle = 50°)

As observed in the equations or the figures, the modification factor *C* sometimes exceeds 1, indicating underestimating or unconservative prediction of the AASHTO LRFD Bridge design Specifications. To be on the safe side, it is recommended that the modification factor *C* be included in design computation.

7.3.2 Prestressed concrete I-girder bridges

The modification factor C for the AASHTO shear distribution factor of the prestressed concrete girder bridges is derived into the following equations for the respective support conditions in the order of (1) simply supported end, (2) fixed end, and (3) bearing supported end, respectively:

$$C = 1.164 - 0.0019L + 0.0002L^{1.03}\tan\theta \qquad (7.11)$$

$$C = 1.15 - 0.002L - \frac{8\tan\theta}{L^{1.5}} \qquad (7.12)$$

$$C = 1.16 - 0.0028L - \frac{4.05\tan\theta}{L^{0.68}} \qquad (7.13)$$

where L is the span length in foot and θ is the skew angle in degree. The applicable ranges for L and θ are $60 \le L \le 120$ and $0° \le \theta \le 50°$. Again these equations are regression results using the corresponding FEA results, with the coefficient of determination R^2 of 0.971, 0.938, and 0.912, respectively. The following figures show the contour plots of modification factors when L and θ are changed within the above range.

Figure 7.22 Contour of modification factor *C* for shear in prestressed concrete girder bridges
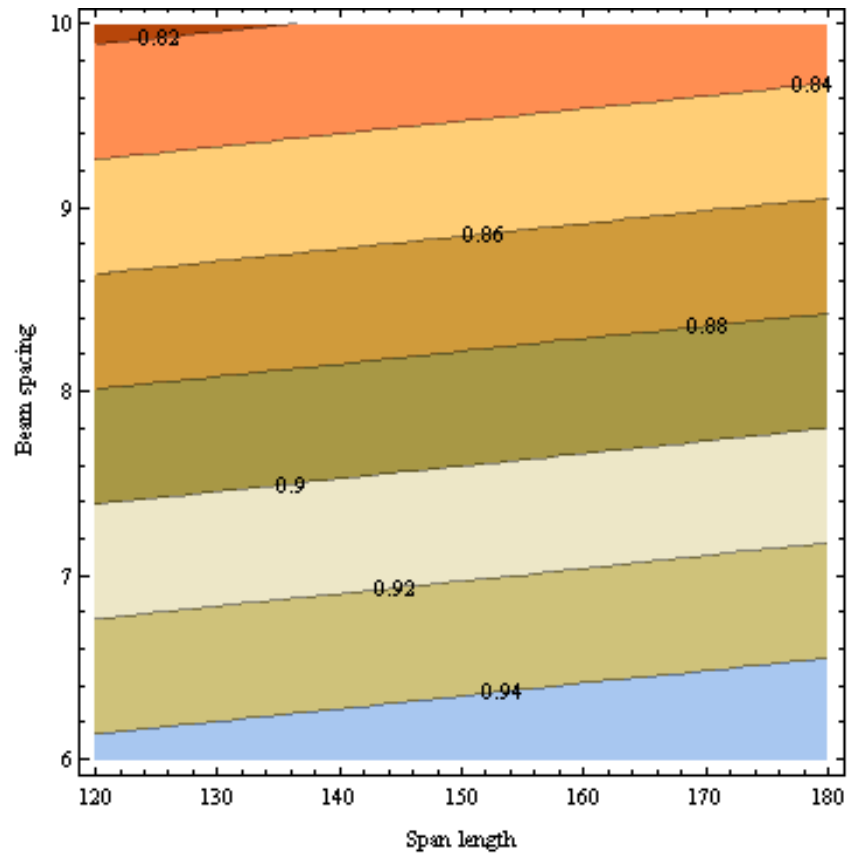
(end condition: simple support)

Figure 7.23 Contour of modification factor *C* for shear in prestressed concrete girder bridges

(end condition: fix support)
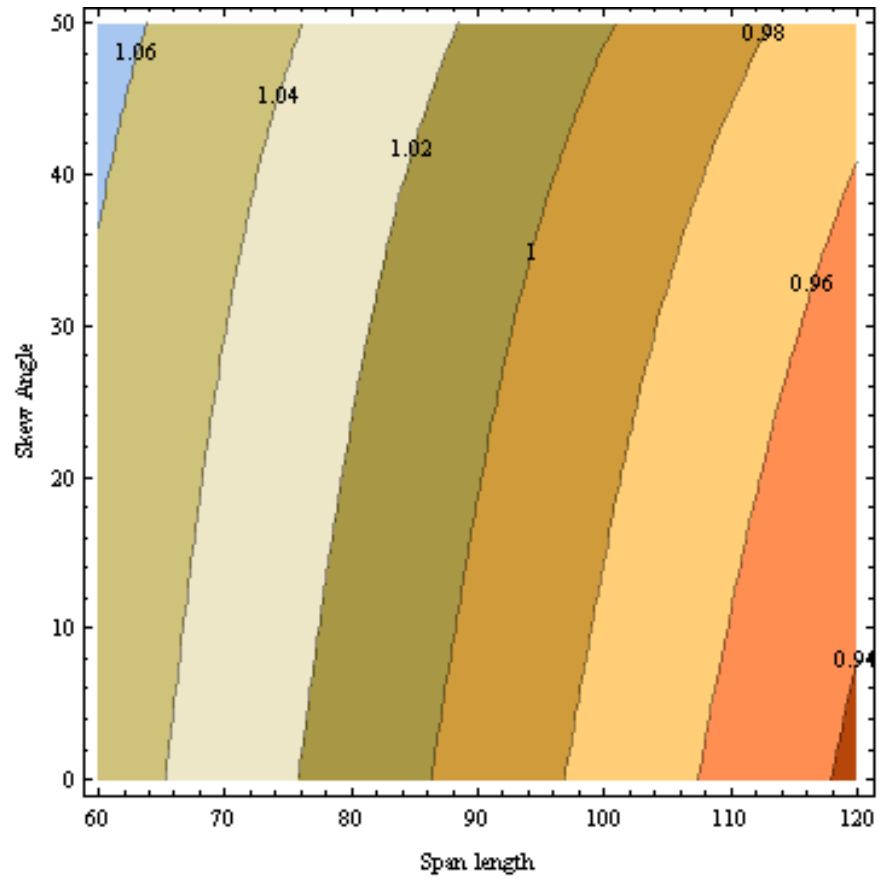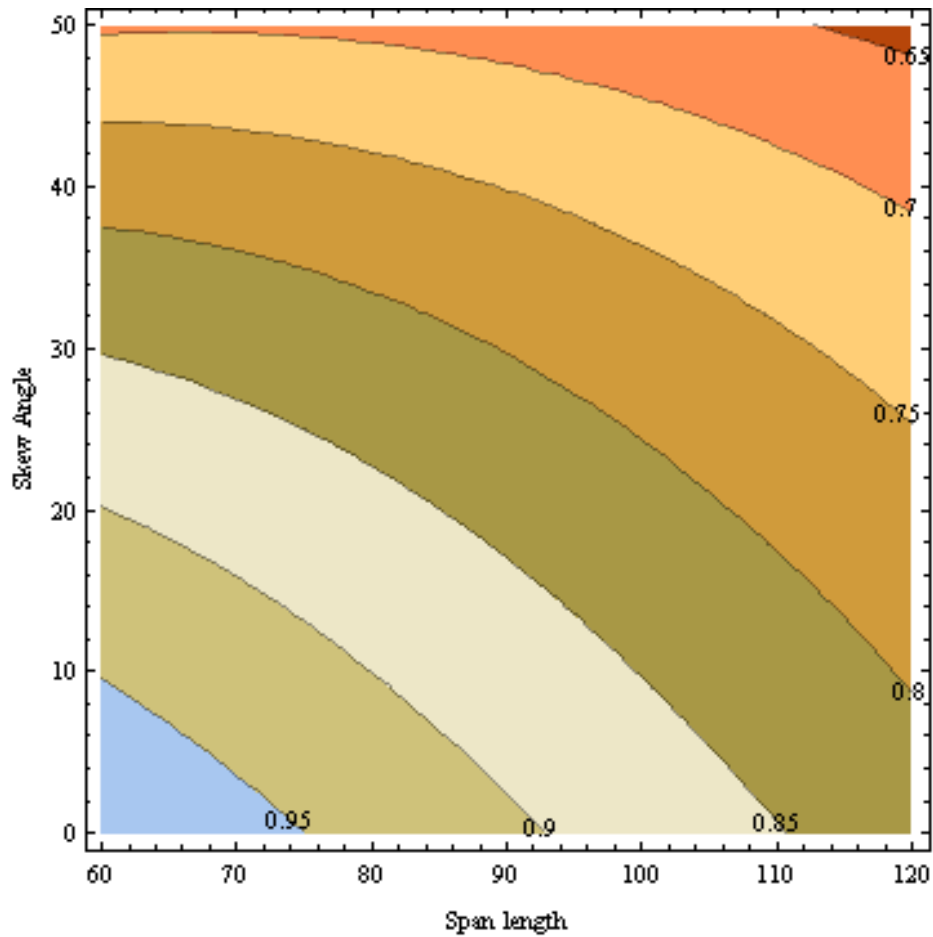
Figure 7.24 Contour of modification factor *C* for shear in prestressed concrete girder bridges

(end condition: bearing support)

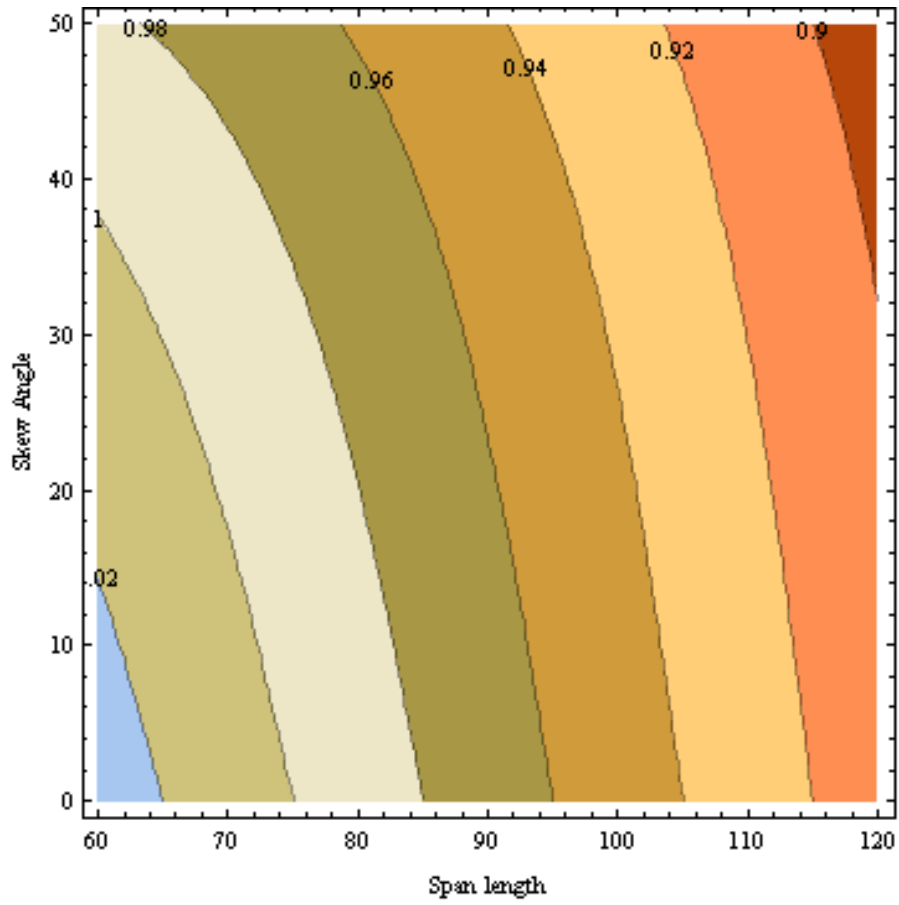As seen in the equations and contour plots, the modification factor *C* occasionally exceeds 1, which identifies the AASHTO LRFD specifications being unconservative. Accordingly, the modification factor *C* is recommended for those cases for routine design.

Chapter 8

Summary, Conclusions, and Recommendations

8.1   Research summary and conclusions

This chapter summarizes the process and conclusions of this research effort on Michigan skewed bridges. Future research topics relevant to this subject are recommended later in this chapter. The major findings and contributions of this research project are summarized as follows.

1) A literature review was completed in this project to summarize state of the art and the practice relevant to skew bridge behavior, analysis, design, and research. The identified and reviewed research efforts have mainly focused on the moment analysis for design, not shear, which increases with severity of skew. The applied research method has been numerical analysis of skewed structures, assisted by limited physical testing for verification.

2) Field measurement was performed in this research project for deck dead load and vehicular live load on a skewed bridge, the Woodruff Bridge, in Monroe County, Michigan. The test program also establishes an appropriate procedure for field measurement of full scale bridges. The measurement results have contributed to understanding of the behavior of a significantly skewed bridge based on maximum strain responses at perceived locations to the intended loads. These measurement data also have played a critical role in the calibration of FEA modeling as an important step to the development of design guidelines in this project.

3) FEA modeling was validated and calibrated using the measurement data from the Woodruff Bridge. Based on this calibration, a sample of 18 typical Michigan bridges were

analyzed using FEA and compared to relevant provisions of the AASHTO LRFD Bridge Design Specifications. In the analysis, skew angle, span length, and beam spacing were selected as controlling parameters. For every of the selected 18 cases of Michigan bridges, effect of boundary condition on the bridge behavior has also been investigated for its effect on the response.

4) The following design guidelines are developed and recommended for the investigated ranges of superstructure type, span length, skew angle, and beam spacing, based on the observations in the load test and the FEA investigation.

a) The AASHO LRFD Bridge Design Specifications' moment distribution factors overestimates the design moment for interior beams in Michigan skewed beam bridges. A modification factor is developed in Chapter 7 to account for this effect in routine design.

b) The AASHTO LRFD Bridge Design Specifications' shear distribution factors may underestimate the design shear for fascia beams in Michigan skewed beam bridges. A different modification factor is developed in Chapter 7 and recommended here to account for this effect in routine design for situations where the AASHTO load distribution factor underestimates.

c) Effects of the AASHTO LRFD Bridge Design Specifications' temperature loads can be significant, to about 10% of the live load effect, in typical Michigan skewed highway bridges. They should not be neglected especially when thermal stresses superimpose to maximum live load stresses.

d) Warping and torsional effects in typical Michigan skewed bridges are small for the considered cases and can be accordingly neglected in design analysis.

5) The AASHTO distribution-factor analysis method is recommended to be extended beyond the MDOT current policy of 30° skew angle limit for refined analysis up to at least 50°,

provided that the modification factor *C* is applied to unconservative shear predictions and if the structure type, span length, beam spacing, and skew angle are within the ranges of the analyzed spans covered in this report (and thus within the applicable ranges of the AASHTO LRFD Bridge Design Specifications provisions.)

6) An analytical solution for skewed thick plates has been developed first time in the literature, where the thick plate is a model for reinforced concrete bridge deck. This solution can be readily furthered to an analytical solution for skewed highway bridges integrated by assembling several thick plates supported on beams. The advantage of this analytical solution approach is a much lower requirement for the end user's data input for routine bridge design analysis, excluding complex information such as element type, shape, size, etc. typically required for FEA. It also will not be restricted by skew angle range as well.

8.2   Recommendations for future research

The following future topics are recommended to further pursue for improved design, construction, and rating of skewed highway bridge spans in Michigan.

1) A field experimental application of sensored bearing at the obtuse corners in a skewed bridge was planned in this project but could not materialize due to several delays in the process. It is recommended to continue to pursue this experimental research. It will allow profound understanding of the magnitude of the obtuse corner shear reaction and its variation during the service life.

2) Further pursue analytical solution for skewed highway bridges under the design dead and live loads, and implement the obtained solution into a computer software program for

routine design application. This program will be much more end-user friendly than FEA programs, without the need for complex input data such as element type, shape, and size that demand months if not years of special and specific training even possibly including graduate school level courses. The recommended research effort should have a task of software development starting with a functionality design so that the end product will be accepted by the targeted users.

3) Investigate and develop possible measures to reduce the potential of skewed deck shrinkage cracking using a deck less constrained to the supporting beams. It has been found (Fu *et al.* 2007) that the full composite action is the cause of such cracking. Thus relaxing this action is expected to reduce cracking potential effectively. Practical designs need to be developed in this research effort that can be effectively and efficiently implemented in routine design and construction. This research effort will also significantly mitigate or eliminate deck early cracking for straight bridges as well.

REFERENCES

[1] AASHTO LRFD Bridge Design Specifications, 3rd Edition, 2004

[2] AASHTO LRFD Bridge Design Specifications, 4th Edition, 2007

[3] AASHTO Standard Specifications for Highway Bridges, 17th Edition, 2002

[4] Aref, A.J., Alampalli, S. and He, Y., "Ritz-Based Static Analysis Method for Fiber Reinforced Plastic Rib Core Skew Bridge Superstructure", Journal of Engineering Mechanics, 127(5), pp.450-458, 2001

[5] Bellman, R., "Methods of nonlinear analysis", Academic Press, New York, 1973

[6] BridgeTech, Tennessee Technological University, Mertz, D. "Simplified Live Load Distribution Factor Equations" TRB NCHRP Report 592, 2007

[7] Bishara, A.G. and Liu, M.C. and El-Ali, N.D., "Wheel Load Distribution on Simply Supported Skew I-Beam Composite Bridges", Journal of Structural Engineering, 119(2), pp.399-419, 1993

[8] Brown, T.G. and Ghali, A., "Finite strip analysis of quadrilateral plates in bending", Proceeding of the American Society of Civil Engineers, 104, pp.480-484, 1978

[9] Chu, K. and Krishnamoorthy, G., "Use of orthotropic plate theory in bridge design", Journal of the structural division, Proceedings of the ASCE, ST3, pp.35-77, 1962

[10] Chun, P. and Fu, G., "Derivation of governing equation of skewed thick plates and its closed-form solution (in Japanese)", JSCE Journal of Applied Mechanics, 12, pp.15-25, 2009

[11] Coull, A., "The analysis of orthotropic skew bridge slabs", Applied Scientific Research, 16(1), pp.178-190, 1966

[12] Dennis M., "Simplified live load distribution factor equations", Transportation Research

Board, NCHRP Report 592, 2007

[13] Dong, C.Y., Lo, S.H., Cheung, Y.K. and Lee, K.Y., "Anisotropic thin plate bending problems by Trefftz boundary collocation method", Engineering Analysis with Boundary Elements, 28(9), pp.1017-1024, 2004

[14] Ebeido, T. and Kennedy, J.B. "Girder moments in continuous skew composite bridges", Journal of Bridge Engineering, 1(1), 37-45, 1996

[15] Ebeido, T. and Kennedy, J.B., "Shear and Reaction Distributions in Continuous Skew Composite Bridges", Journal of Bridge Engineering, 1(4), pp.155-165, 1996

[16] Federal Highway Administration, "Recording and coding guide for the structure inventory and appraisal of the nation's bridges", FHWA-96-001, 1995

[17] G.Fu, J.Feng, J.Dimaria, and Y.Zhuang "Bridge Deck Corner Cracking on Skewed Structures", Final Report to Michigan Department of Transportation, Wayne State University, Detroit, MI, Report RC-1490, September 2007

[18] Gangarao, H.V.S. and Chaudhary, V.K., "Analysis of skew and triangular plates in bending", Computers & Structures, 28(2), pp.223-235, 1988

[19] Gupta, D.S.R. and Kennedy, J.B., "Continuous skew orthotropic plate structures", Journal of the structural division, Proceedings of the ASCE, ST2, pp.313-328, 1978

[20] Hangai, Y., "Theory of plates (in Japanese)", Shoukokusha, Tokyo, 1995

[21] Heins, C.P., "Bending and torsional design in structural members", Lexington Books, Toronto, 1975

[22] Heins, C.P., "Applied plate theory for the engineer", Lexington Books, Toronto, 1976

[23] Heins, C.P. and Looney, C.T.G., "Bridge analysis using orthotropic plate theory", Journal of the structural division, Proceedings of the ASCE, ST2, pp.565-592, 1968

[24] Helba, A. and Kennedy, J.B., "Skew composite bridges - analyses for ultimate load", Canadian Journal of Civil Engineering, 22(6), pp.1092-1103, 1995

[25] Huang, H., Shenton, H.W. and Chajes, M.J., "Load Distribution for a Highly Skewed Bridge: Testing and Analysis", Journal of Bridge Engineering, 9(6), pp.558-562, 2004

[26] Igor, C. and Christian, C., "Variational and potential methods in the theory of bending of plates with transverse shear deformation", Chapman & Hall/CRC, New York, 2000

[27] Jawad, M.H. and Krivoshapko, S.N., "Design of plate and shell structures", Applied Mechanics Reviews, 57, B27, 2004

[28] Kennedy, J.B. and Gupta, S.R., "Bending of skew orthotropic plates structures", Journal of the structural division, Proceedings of the ASCE, ST8, pp.1559-1574, 1976

[29] Kennedy, J.B., "Plastic analysis of orthotropic skew metallic decks", Journal of the structural division, Proceedings of the ASCE, ST3, pp.533-546, 1977

[30] Khaloo, A.R. and Mirzabozorg, H., "Load Distribution Factors in Simply Supported Skew Bridges", Journal of Bridge Engineering, 8, pp.241-244, 2003

[31] Komatsu, S., Nakai, H. and Mukaiyama, T., "Statical Analysis of Skew Box Girder Bridges", Journal ournals of the Japan Society of Civil Engineers, 189, pp.27-38, 1971

[32] Liew, K.M. and Han, J.B., "Bending analysis of simply supported shear deformable skew plates", Journal of Engineering Mechanics, 123(3), pp.214-221, 1997

[33] Malekzadeh, P. and Karami, G., "Differential quadrature nonlinear analysis of skew composite plates based on FSDT", Engineering Structures, 28, pp.1307-1318, 2006

[34] Menassa, C., Mabsout, M., Tarhini, K. and Frederick, G., "Influence of Skew Angle on Reinforced Concrete Slab Bridges", Journal of Bridge Engineering, 12, pp.205-214, 2007

[35] Mindlin, R.D., "Influence of rotatory inertia and shear on flexural motions of isotropic,

elastic plates", Journal of Applied Mechanics, 18(1) , pp.31-38, 1951

[36] Mitsuzawa, T. and Kajita, T., "Analysis of skew plates in bending by using B-spline functions", A bulletin of Daido Technical College, 14, pp.85-91, 1979

[37] Morley, L.S.D., "Bending of a simply supported rhombic plate under uniform normal loading", The Quarterly Journal of Mechanics and Applied Mathematics, 15(4), pp.413-426, 1962

[38] Morley, L.S.D., "Skew Plates and Structures", Pergamon Press, New York, 1963

[39] Pai, P.M., " A new look at shear correction factors and warping functions of anisotropic laminate", International Journal of Solids and Structures, 32(16), pp.2295-2314, 1995

[40] Rajagopalan, N., "Bridge superstructure", Alpha Science International, Oxford, 2006

[41] Ramesh, S.S., Wang, C.M., Reddy, J.N. and Ang, K.K., " Computation of stress resultants in plate bending problems using higher-order triangular elements", Engineering Structures, 30(10), pp.2687-2706, 2008

[42] Reddy, J.N., "Mechanics of laminated composite plates and shells: theory and analysis", CRC Press, Taylor & Francis, 2004

[43] Reddy, J.N., "Theory and analysis of elastic plates and shells", CRC Press, Taylor & Francis, 2007

[44] Reissner, E., "The effect of transverse shear deformation on the bending of elastic plates", Journal of Applied Mechanics, 12, pp.A69-A77, 1945

[45] Robinson, J., "Basic and shape sensitivity tests for membrane and plate bending finite elements", Robinson and Associates, England, 1985

[46] Saadatpour, M.M., Azhari, M., and Bradford, M.A., "Analysis of general quadrilateral orthotropic thick plates with arbitrary conditions by the Rayleigh-Ritz method", International

Journal for Numerical Methods in Engineering, 54, pp.1087-1102, 2002

[47] Sengupta, D., "Stress analysis of flat plates with shear using explicit stiffness matrix", International Journal for Numerical Methods in Engineering, 32, pp.1389-1409, 1991

[48] Sengupta, D., "Performance study of a simple finite element in the analysis of skew rhombic plates", Computers and Structures, 54(6), pp.1173-1182, 1995

[49] Surana, C.S. and Agrawal, R., "Grillage analogy in bridge deck analysis", Narosa Publishing House, London, 1998

[50] Szilard, R., "Theory and analysis of plates - classical and numerical method", Prentice-hall, New Jersey, 1974

[51] Tamaz, S.V., "The theory of anisotropic elastic plates", Kluwer Academic Publishers, London, 1999

[52] Tham, L.G., Li, W.Y., Cheung, Y.K. and Chen, M.J., "Bending of skew plates by spline-finite-strip method", Computers and Structures, 22(1), pp.31-38, 1986

[53] Timoshenko, S.P. and Woinowsky-Krieger, S., "Theory of plates and shells (2nd edition)", Engineering Societies Monographs, New York, McGraw-Hill, 1959

[54] Ugural, A.C., " Stresses in plates and shells", McGraw-Hill, New York, 1999

[55] Vlachoutsis, S., "Shear correction factors for plates and shells", International Journal for Numerical Methods in Engineering, 33(7), pp.1537-1552, 1992

[56] Wang, G. and Hsu, C.T.T., "Static and dynamic analysis of arbitrary quadrilateral flexural plates by B3-spline functions", International journal of solids and structures, 31(5), pp.657-667, 1994